DLR

Report on DLR work in SMART

Version 1.0

	REPORT ON DLR WORK IN SMART	

DISTRIBUTION LIST

NAME	COMPANY	ADDRESS	I/A
SMART email list		Smart@elec.rma.ac.be	I

(I = for information, A = for action)

STATUS INFORMATION

Security classification :		Status :	Approved
Current version number :	1.0	Date of first issue :	30/09/04
Prepared by :	Martin Keller	Date :	30/09/04
	Björn Dietrich		
	Rupert Müller		
	Dr. Peter Reinartz		
	Dr. Mihai Datcu		
Verified by :	Reinhard Schröder	Date :	30/09/04
Approved by :	Dr. Helmut Süß	Date :	30/09/04
	Dr. Manfred Schröder		

Copyright notice

DOCUMENT CHANGE RECORD

Version	Date	Description	Affected sections
1.0	30/09/04	Initial version	All

CONTENTS

1 Measurement Campaign and Data Acquisition

Between 6 and 10 August, 2001, two aircrafts of DLR went to Croatia for recording data in four test sites containing mine suspected areas. The E-SAR sensor was installed on board a Dornier Do 228 aircraft, the multispectral scanner Daedalus and the RMK camera using a colour infrared film were mounted on board a Cessna Caravan. The weather conditions were quite perfect (blue sky, no rain, dry soil, few wind) just as the good collaboration of people from CROMAC and DLR.

The plans for recording airborne data were changed during the meeting on 17 July 2001 at DLR. Additionally to the original plans E-SAR data in C- and P-band were recorded. C-band data were asked for by CROMAC, since the measuring system LISA (JRC) that was planned in the ground truth mission has C band as upper frequency limit. Due to the lack of financial support the measurement with LISA has not been performed.

The partners also agreed that P-band data could be very useful because of the very good penetration abilities due to the long wavelength even though P-band at the E-SAR sensor still is in an experimental state and therefore useful data couldn't be guaranteed. Recording of C- and P-band was possible only by cancelling hh-polarisation in X-band and reducing redundant recordings (normally done for security reasons) in X- and L-band. At the same meeting CROMAC proposed wider regions (4x3km) as test areas than it was planned before (3x3km). The proposed regions were accepted and are used now for all activities. These regions are named Glinska Poljana, Pristeg, Ceretinci and Blinjski Kut (validation area).
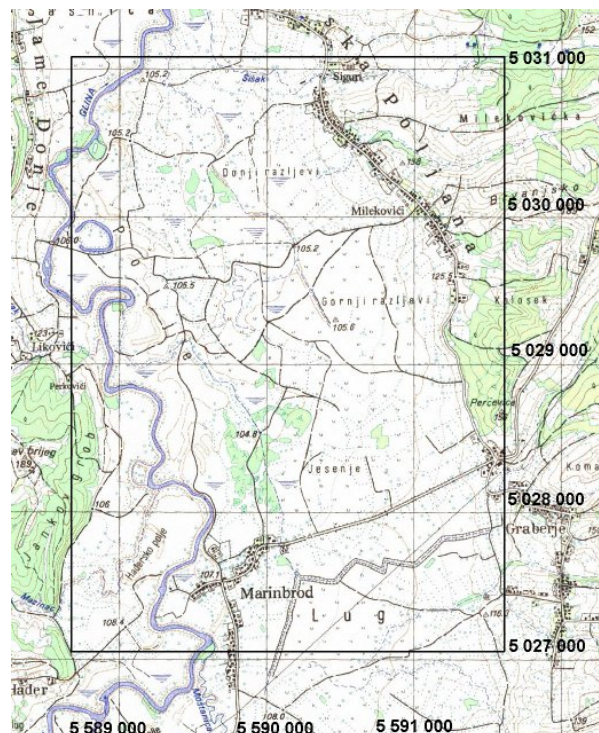
Figure 1: Test area Glinska Poljana
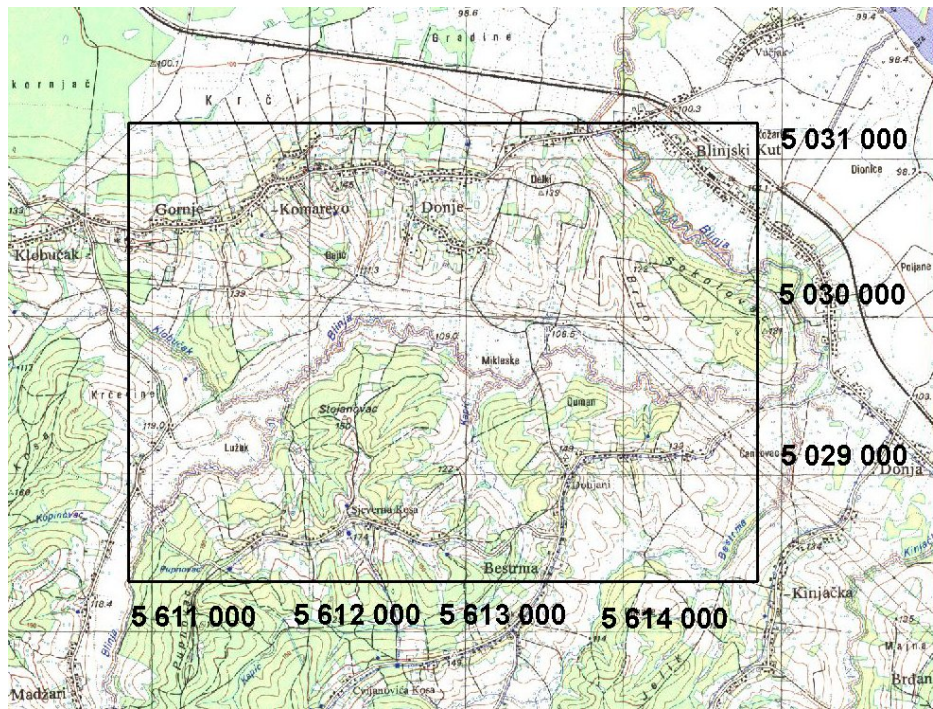
Figure 2: Test area Blinjski Kut
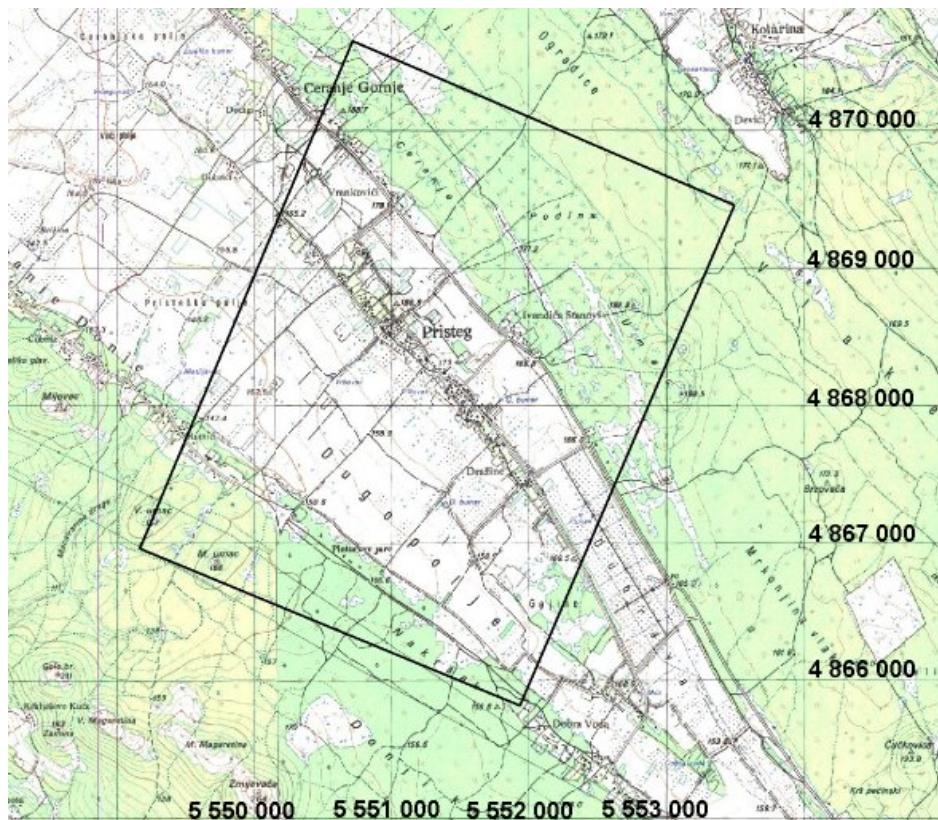
Figure 3: Test area Pristeg

Figure 4: Test area Ceretinci

CROMAC offered digital elevation models (DEM) for the test areas which are necessary for the production of the orthoimages. The proposal was accepted. Therefore the collection of aerial views with the RMK camera from a high flight track (2000m above ground) in stereo mode for DEM creation was cancelled. Very high resolution RMK images as well as Daedalus optical scanner data were taken from low positions (330m above ground) as planned.

Data	SMART Proposal	Recorded
E-SAR, X-band, vv-polarisation	X	X
E-SAR, X-band, hh-polarisation	X	-
E-SAR, C-band, vv-polarisation	-	X
E-SAR, L-band, fully polarimetric	X	X
E-SAR, P-band, fully polarimetric	-	X
Daedalus (330m above ground)	X	X
RMK (330m above ground)	X	X
RMK stereo (2000m above ground)	X	-

Table 1: Overview of the aerial data foreseen in DoW (EC IST, SMART, 2000) and collected

During the flight campaign two ground teams consisting of members of DLR and CROMAC were positioning radar reflectors (corner reflectors and Luneberg lenses) for calibration of the E-SAR data and geodetic GPS systems for high precision determination of the Do 228 flight

tracks. There were always two corner reflectors (provided by DLR) placed inside the test area looking in opposite directions, the Luneberg lens reflectors (provided by CROMAC) were placed in 4 groups of 2 or more reflectors, having opposite directions.

Figure 5: Ground team at the flight campaign in Glinska Poljana. Left image: Corner reflectors, GPS-system. Right image: Luneberg lenses at one position, looking into opposite directions.

The Daedalus data have been left with CROMAC directly after the flight campaign, where they were preliminary pre-processed in strips (only for visualisation) for export permission by the Croatian authorities. The RMK and E-SAR data have been brought to Germany under supervision of Mladen Viher (CROMAC). The RMK aerial film has been developed in Münster, Germany, the E-SAR data were transcribed from Sony tape to Exabyte tapes at DLR. Furthermore a survey processing for all the acquired E-SAR data has been done to get first (low quality) images of the data. After that, everything was brought back to CROMAC. Between 10th and 18th of September 2001 Martin Keller (DLR) went to Zagreb, Croatia for processing some of the E-SAR data for export permission by the Croatian authorities. The export permission finally was granted middle of October 2001 and all data were shipped to DLR for further processing.

During the measurement campaign photos of the ground (overview, vegetation, landmarks) were taken by the ground team. They were scanned at DLR and provided to the partners together with other useful information like
- scanned maps with the position and look direction of the photos,
- scanned maps with the approximate centre coordinates of the RMK aerial views,
- meteorological notes of the measurement campaign

Further information concerning the measurement campaign can be found in the deliverable D1.2.

2 Data Processing and Delivery

2.1 DEM used for Geocoding

In an early stage of the SMART project it was planned to use interferometric SRTM (Shuttle Radar Topography Mission) data for the creation of DEMs (digital elevation models) of the four test areas in the SMART project. Additionally other possibilities for DEM creation were taken into account (collection of RMK stereo image pairs from 2000m above the test areas, E-SAR X-band single pass interferometry, use of existing DEMs provided by CROMAC). During the technical meeting on 17/07/2001 at DLR the decision was taken to use existing DEMs provided by CROMAC. A first DEM of the test area Glinska Poljana was handed out on 29/10/2001 while for the other three test areas the DEMs had to be refined. New DEMs of the other test areas have been provided to DLR and were checked. After removal of artefacts, these DEMs seem to be of reasonable quality, although pixel accuracy can not be achieved.

Further information concerning the used DEMs can be found in the deliverable D1.7.

2.2 E-SAR / Daedalus Data Overview

Airborne data, which was processed and delivered to the partners, is listed in the following table:

	Daedalus		E-SAR			
	Mosaicked Image	**Single Stripes**	**Geocoded**	**Ground Range**	**SLC**	**IF Slave SLC**
Glinska Poljana	delivered	delivered	X,C,L,P	-	X,C,L,P	L,P
Blinjski Kut	delivered	delivered	X,C,L,P	L,P	X,C,L,P	L,P
Pristeg	delivered	delivered	X,C,L,P	L,P	X,C,L,P	L,P
Ceretinci	delivered	delivered	X,C,L,P	L,P	X,C,L,P	L,P

Table 2: Processed data (SLC: single look complex data; IF: interferometric data)

Ground range amplitude E-SAR L- and P-band data of Blinjski Kut, Pristeg, and Ceretinci were only processed because geocoded data could not be produced before March 2002 due to missing digital elevation models for these test areas. The ground range data have the same data format as geocoded data, therefore tests of the developed algorithms were possible with these data sets already. Since geocoded amplitude E-SAR data are available now, the ground range data are not used any more.

The processing of E-SAR geocoded and SLC data has finished, the data has been delivered to the partners.

Some problems occurred while mosaicking of the Daedalus data stripes of Blinjski Kut. Especially in the south-east of the test area the DEM is not very accurate, which results in an offset of several meters between pixels of adjacent data stripes which show the same object. It was possible to correct some of these errors by hand, but the resulting geocoded image still has a geocoding error of several meters. The only possibility to correct this error would be to

start the geocoding process of the data set again with a very accurate DEM but such a DEM is not available in the SMART project.

2.3 E-SAR Data

For each test area data wase collected in X-, C-, L-, and P-band. X- and C-band was recorded in vv-polarisation (vertical received, vertical transmitted), L- and P-band data is fully polarimetric (hh, hv, vv, vh-polarisations). Additionally, L- and P-band were both recorded several times from slightly different tracks, so that repeat pass interferometric processing is possible. The baselines which are available are 13m and 20m for L-band, 40m and 60m for P-band. For redundancy reasons the data have been recorded from both sides of the test area. C- and P-band, as well as interferometry was not foreseen in the contract, but it was possible to record this data without additional costs by using the available flight time efficiently.

Except for one pass out of 78, all data is of excellent quality, recording for the bad pass was stopped during the flight. In the data of X-, C-, and L-band, no visible interferences can be found, the data quality is high. Although in P-band there are sometimes visible interferences, the overall quality of P-band is better than expected. Due to the experimental status of P-band an absolute calibration of the P-band data is not yet possible.

E-SAR raw data (radar holograms) have been copied from HDDT tape, which was used during the recordings, to Exabyte tapes, which can be used at the processing computer. The programme for E-SAR processing has been developed at DLR, and due to its experimental character, it is very often updated, new features are added, and existing routines are optimised. In the SMART project, for the first time ever P-band data had to be both geocoded and interferometrically processed which caused some problems that had to be solved. The first geocoded data sets that were provided to the project partners contained an offset from their real positions of several meters. Meanwhile corrected geocoded data of Glinska Poljana in X-, C-, and L-band have been provided to the partners, P-band data will follow soon.

The processing chain includes (if: only for repeat pass interferometric processing):
- reading raw data, aircraft navigation and motion data, DEM data, and corner reflector positions
- interference filtering (P-band)
- processing to slant range image data
- slant range to ground range conversion
- polarimetric calibration (L- and P-band)
- coregistering (if)
- interferogram generation (if)
- coherence calculation (if)
- geocoding
- writing a backup tape and image tapes of the final data

The spatial resolution in range direction is 2.0m in X-, C-, and L-band and 4.0m in P-band. The azimuth resolution differs for multilook geocoded data and for SLC slant range data. In geocoded data the azimuth resolution is 1.5m for X- and C-band, 2.0m for L-band, and 4.0m for P-band, in SLC data it is: 0.6m for X- and C-band, 0.8m for L-band, 1.6m for P-band.

2.4 Daedalus Data

Data for all four test areas was collected in 12 different channels, ranging from visible blue to thermal infrared in excellent quality. The Daedalus data was collected from very low altitude (330m) to get a high spatial resolution. Therefore several stripes of data were collected in each test area and mosaicked to one geocoded image afterwards. The processing chain for Daedalus data processing consists of:

- system corrections
    - correction for interrupted scanlines
    - correction of perspective dependent sensor sensitivity
radiometric processing
    - calibration of the raw data
    - radiometric normalisation
geometric processing
    - preparation of aircraft position and flight attitude
    - geocoding of the image stripes
    - mosaicking the stripes into one image

There are several conspicuous stripes in the images running from north to south that come from different orientation angles between sensor, sun, and object, while the aircraft recorded image stripes flying from north to south and back. The effect is minimal when the sun is along the axis of the flight track, the reflectance symmetry to both sides of the tracks then leads to a similar reflectance around the border of two adjacent stripes. Anyhow, the reflectance between the same objects in the middle and at the border of a stripe will be different. This depends on object characteristics and can not be compensated during the processing, while the perspective dependent sensor sensitivity only depends on the sensor itself and was eliminated.

Spectral sensitivities

Each Daedalus channel is able to receive electromagnetic waves in a part of the whole spectrum. Since the sensitivity is not equal for all wavelengths inside this window, this is an important fact to know. Here we present tables for each channel, showing the sensitivity in dependence of the wavelength. The maximum sensitivity is scaled to 100.

spectral sensitivity, ch3

spectral sensitivity, ch4

spectral sensitivity, ch5

spectral sensitivity, ch6

spectral sensitivity, ch7

spectral sensitivity, ch8

spectral sensitivity, ch9

spectral sensitivity, ch10
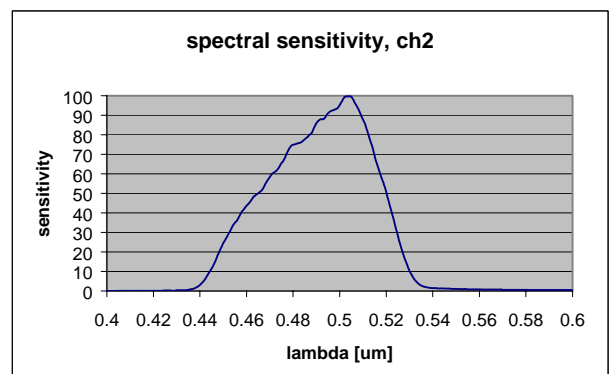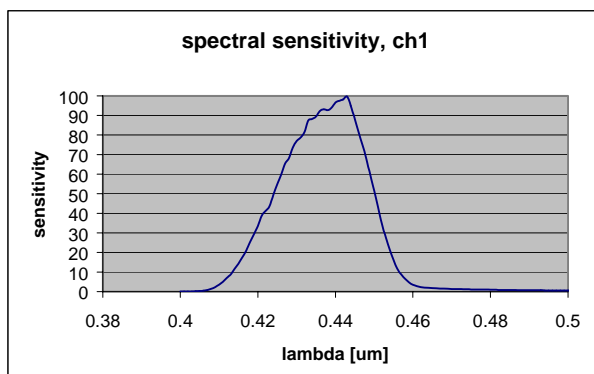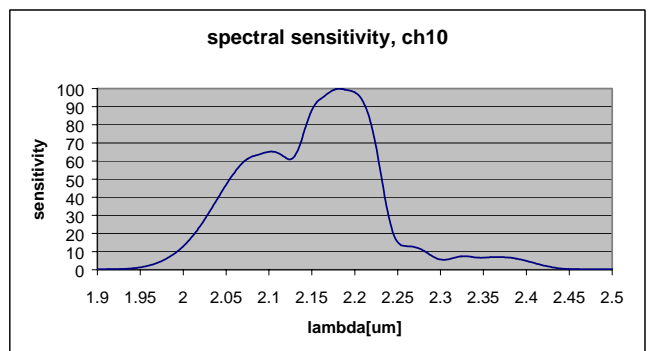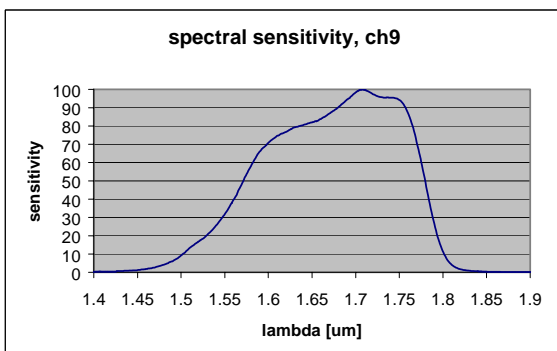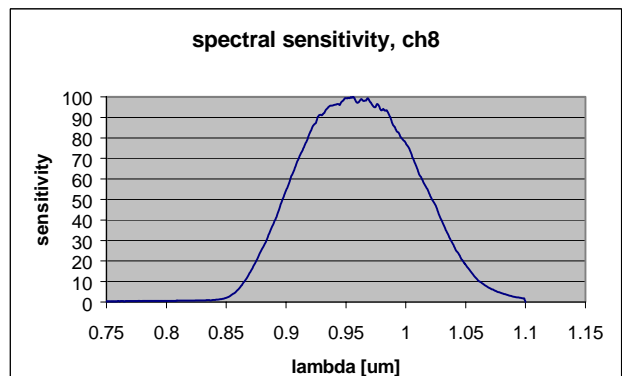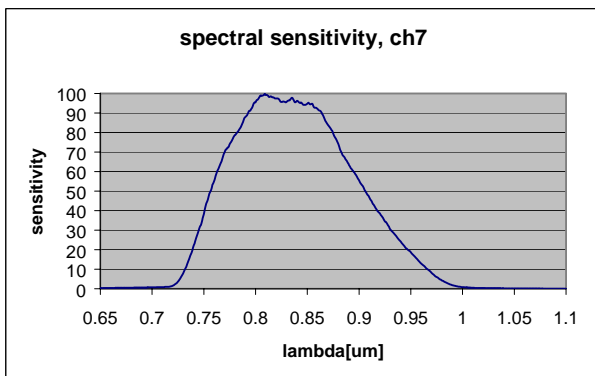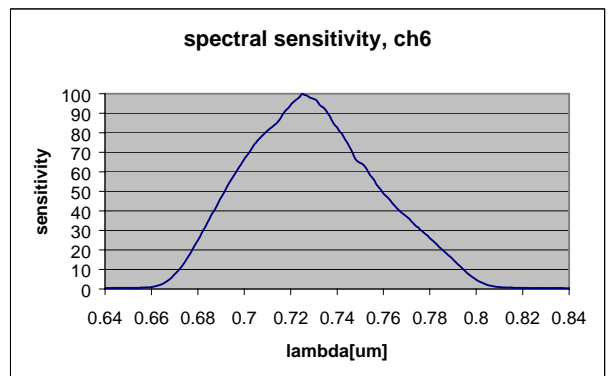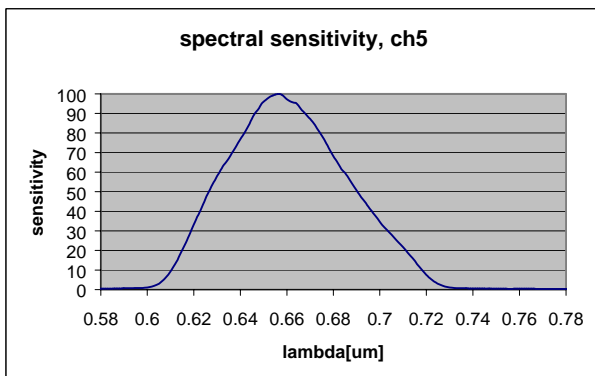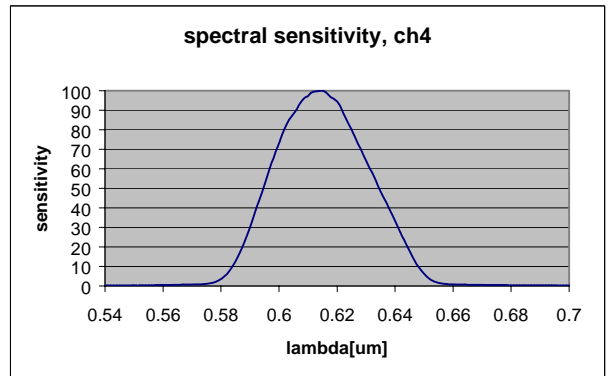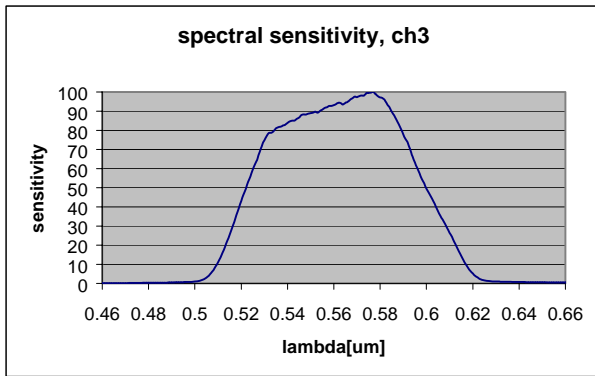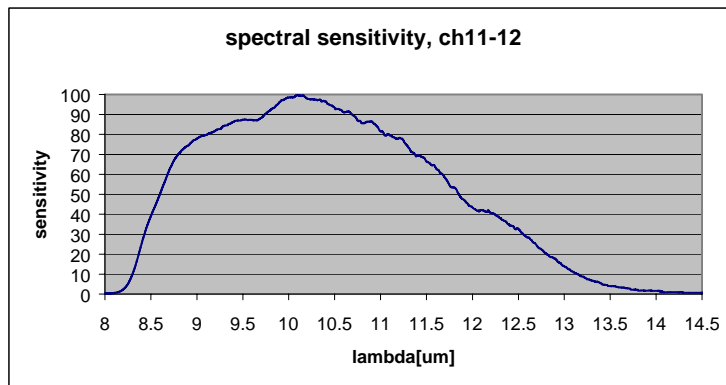
2.5 Data Registration

The 12 channels of Daedalus data are by default already registered, because they are recorded at the same time. For the same reason, the four channels of fully polarimetric L- and P-band E-SAR data are registered too. Work on data registration is therefore necessary between E-SAR data of different wavelengths and between Daedalus and E-SAR data.

First tests at DLR have shown that geocoded multifrequency E-SAR data are already very good registered so that an additional workstep is not necessary. Fig.6 and Fig.7 show rgb-composites of geocoded data of Glinska Poljana that show the corner reflector in different wavelengths. For all bands the response of the corner reflector comes from the same point in the geocoded data.

In Fig.8 and Fig.9 an effect can be seen that can lead to errors in manual registration if it is not taken into account. In volume scatterers like the canopy of trees, radar waves of longer wavelength penetrate deeper into the volume than shorter wavelengths. Therefore the measured distance to volume scatterers is slightly different for different wavelengths and the objects show up at different positions in the image. In Fig.8 and Fig.9 it can be observed, that trees have stronger backscatter in the blue channel (highest frequency) at the right side which is directed to the sensor while the left side is rather red (lowest frequency). This effect is due to larger penetration depth of longer radar wavelengths. As an example, X-band is scattered at the outer leaves and branches of a tree while L-band penetrates into the crown and therefore the centre of backscattering is at a different position, further away from the sensor. Using volume scatterers like trees for registration will lead to registration errors. Only surface scatterers, positioned at the earth's surface, like the corner reflector or crossroads should be used for registration purposes.
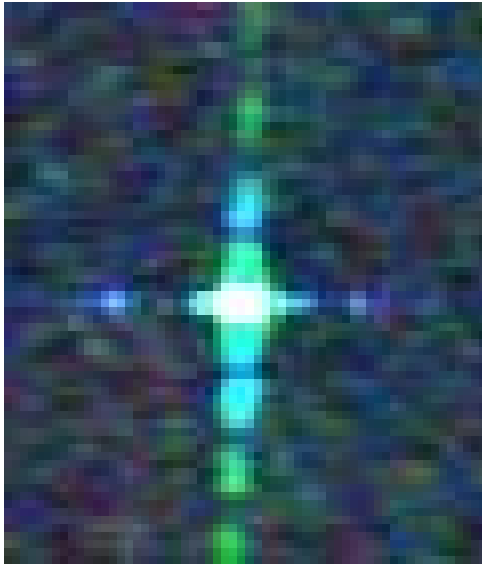
Fig.6: rgb composite of E-SAR geocoded data of the corner reflector at Glinska Poljana.
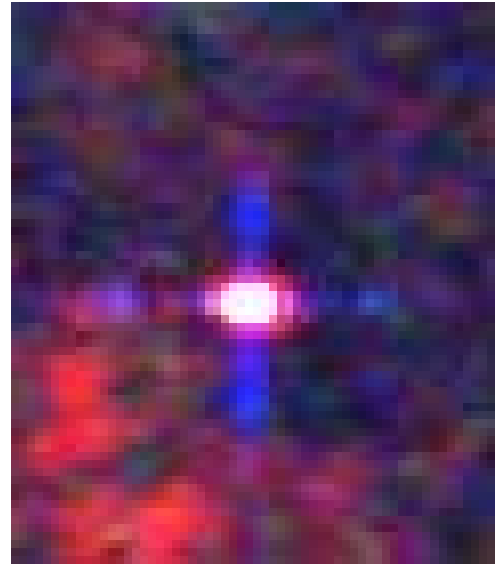
(r,g,b: Lvv,, Cvv, Xvv)

Fig.7: rgb composite of E-SAR geocoded data of the corner reflector at Glinska Poljana.
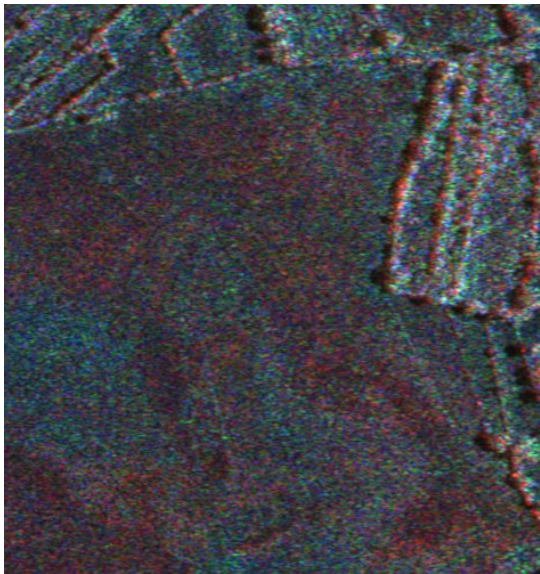
(r,g,b: Pvv, Lvv, Xvv)

Fig.8: rgb composite of E-SAR geocoded data of a mine suspected region at Glinska Poljana.

(r,g,b: Lvv, Cvv, Xvv)
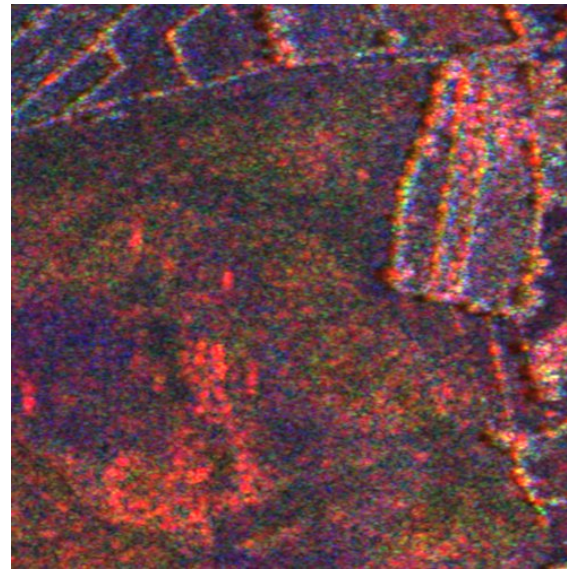
Fig.9: rgb composite of E-SAR geocoded data of a mine suspected region at Glinska Poljana.

(r,g,b: Pvv, Lvv, Xvv)

2.6   RMK Aerial Views

A complete set of 378 paper prints in A3 format of the RMK aerial views was sent to RMA, ULB, and ENST. For creating these prints, all 378 CD-ROMs had to be read. The original very high resolution digital images were saved in lower resolution (approximately 10cm instead of 3cm, 30-50MB instead of 650MB) in order to have the maximum possible

resolution of the A3 prints and at the same time allow a faster printing due to the reduced data size. The smaller digital images were saved on 27 CD-ROMs and were provided to the partners via ftp. Since CROMAC was interested on full resolution RMK data of selected areas, a member of CROMAC came to DLR and copied approx. 100 full resolution images to hard disk (approx. 80GB).

During the production of prints of the 378 RMK aerial views, digital images of lower resolution (10cm instead of 3cm) and of smaller size (50MB instead of 650MB) have been created. These digital images were saved on CD. Since several partners in SMART were interested in these digital images, they were provided to them via ftp.

2.7 New Format for Polarimetric E-SAR SLC Data

During the discussion about integration of the algorithms it was decided to store the polarimetric SLC SAR data in one single 3-channel file in little endian format. Originally every polarisation was saved in a separate file in XDR-format. All polarimetric SLC data sets have been created as decided together with an ASCII header file containing useful information. The data sets have been provided to the partners via ftp.

Further information concerning the data processing can be found in the deliverable D2.1.

3   Available Satellite Data

3.1   Requirements on Spaceborne Data in the Project SMART

Spaceborne data can help the project SMART by adding information that could not be collected during the airborne measurement campaign in August 2001. During the measurement campaign multispectral data between the visible blue and the thermal infrared have been collected with 1m resolution by the Daedalus optical scanner, colour infrared aerial views with 3cm spatial resolution were taken by the RMK camera, and the E-SAR system collected SAR data in X-band (vv-polarisation), C-band (vv-polarisation), L-band (fully polarimetric and interferometric), and P-band (fully polarimetric and interferometric). This diversity of the airborne data together with the high overall data quality cannot be achieved by any existing spaceborne system.

The possible benefit from spaceborne data comes from the ability to use data of the time before the war (until Sept. 1991) or during the war (Sept. 1991 - Dec. 1995) for a change detection together with the airborne data. Such a fused analysis leads to best results if the used data sets have relatively similar properties. A crucial data parameter besides the data acquisition time is therefore the spatial resolution of the spaceborne data set. A high data quality (radiometric resolution and signal to noise level) is important as well. Data of sensors which are known to have a low data quality (e.g. due to technical problems) should be avoided.

3.2   Comparison of Spaceborne Sensor Data

Since the technical possibilities of spaceborne optical and SAR sensors have evolved greatly over the last decades, spaceborne remote sensing data of different satellite generations differ strongly in spatial resolution, coverage, period of data collection and costs. In the following tables different spaceborne sensors are being compared concerning sensor properties and coverage of the test areas in the SMART project. Green highlighted parts show the most promising sensor properties, yellow parts indicate that the sensor property is not exactly what we are looking for but the data can still be used if no better choice is found, and red marked text excludes the sensor from the use for change detection in the SMART project.

Optical Sensors	Spatial Resolution	Wavelength	Nr. channels [bits/ pixel]	Scene size [km^2]	Operation time	Price / scene
LANDSAT 4,5	28.5m	450-12500nm	7[8]	185 x 170	since 1982	$US 550
KVR-1000	2m	panchrom. film	-	40 x 40	1983 - 1993	$US 900-2000
Spot 1-4	10m / 20m	510-730nm / 500-890nm	1[8] / 3[8]	60 x 60	since 1986	EUR 1200 (2000 and older), EUR 1900 (new data)
IRS-1 C/D	5.8m / 24m	500-750nm / 520-1700nm	1[6] / 4[7]	70 x 70	since 1995 / 1997	EUR 900 (1/9 scene)
LANDSAT 7	15m /	520-900nm /	1[8] / 7[8]	185 x 170	since 1999	$US 475-600

	28.5m	450-12500nm				
IKONOS	1m / 4m	450-900nm	1[11] / 4[11]	11 x 11	since 1999	$US 900 and up
EROS A	1m	500-900nm	1[11]	6 x 6	since 2000	$US 1250
QuickBird	0.61m / 2.4m	450-900nm	1[11] / 4[11]	16.5 x 16.5	since 2001	$US/km² 25-70
OrbView-3	1m / 4m	450 - 900nm	1[11] / 4[11]	7 x 5	since 2002	$US 250 and up
Spot 5	2.5m / 10m	480-1750nm	1[8] / 4[8]	60 x 60	since 2002	EUR 1900-5400

Table 3: Sensor properties of the most important spaceborne optical sensors which can be relevant for SMART

SAR Sensors	Spatial Resolution	Radar band, λ, polarisation, inc. angle	Nr. channels [bits / pixel]	Scene size [km²]	Operation time	Price / scene
ERS-1	26m	C-band, 5.7cm, vv, 23°	1[16]	100 x 102	1991 - 2000	$US 1200-1400
ERS-2	26m	C-band, 5.7cm, vv, 23°	1[16]	100 x 102	since 1995	$US 1200-1400
JERS-1	18m	L-band, 23cm, hh, 35°	1[8]	75 x 100	1992-1998	$US 650-1000
Radarsat-1	8m (fine) / 25m (std)	C-band, 5.6cm, hh, 40°	1[16]	50 x 50 / 100 x 100	since 1995	$US 3250 / $US 3000
SRTM, X-SAR	25m	X-band, 3.1cm, vv, 52°	1[16]	50 x 100	11-22 Feb. 2000	EUR 150
SRTM, SIR-C	25m	C-band, 5.8cm, hh, vv, hv, vh, 23°-63°	4[80]	225 x 100	11-22 Feb. 2000	EUR 150

Table 4: Sensor properties of the most important spaceborne SAR sensors which can be relevant for SMART

Optical Sensor	Glinska Poljana	Blinjski Kut	Pristeg	Ceretinci
LANDSAT 4,5	1 scene avail. (1995)	1 scene avail. (1995)	1 scene avail. (1995)	1 scene avail. (1994)
KVR-1000	1 scene avail (1989)	covered (1989)	1 scene avail (1989)	1 scene avail (1988)
Spot 1-4	1 scene avail. (1994)	1 scene avail. (1994)	1 scene avail. (1994)	2 scenes avail. (1994)
IRS-1 C/D	covered (1996-now)	covered (1996-now)	covered (1996-now)	covered (1996-now)
LANDSAT 7	covered (1999-now)	covered (1999-now)	covered (1999-now)	covered (1999-now)
IKONOS	covered (May 2000)	not covered	covered (Feb 2000), partly with clouds	not covered
EROS A	not covered	not covered	not covered	not covered
QuickBird	not covered	not covered	not covered	not covered
OrbView-3	not covered	not covered	not covered	not covered
Spot 5	not known due to Spot archive search engine error	not known due to Spot archive search engine error	not known due to Spot archive search engine error	not known due to Spot archive search engine error

Table 5: Coverage and availability of spaceborne optical data sets which can be relevant for the project SMART.

SAR Sensor	Glinska Poljana	Blinjski Kut	Pristeg	Ceretinci
ERS-1	covered(1991-1999)	covered(1991-1999)	covered(1992-1999)	covered(1992-1999)
ERS-2	covered(1995-now)	covered(1995-now)	covered(1996-now)	covered(1995-now)
JERS-1	covered(1992-1998)	covered(1992-1998)	covered(1992-1998)	covered(1993-1998)
Radarsat-1	covered(1997-now)	covered(1997-now)	covered(1997-now)	covered(1996-now)
SRTM	covered(Feb 2000)	covered(Feb 2000)	covered(Feb 2000)	covered(Feb 2000)
SRTM, X-SAR	covered(Feb 2000)	covered(Feb 2000)	covered(Feb 2000)	covered(Feb 2000)
SRTM, SIR-C	covered(Feb 2000)	covered(Feb 2000)	covered(Feb 2000)	covered(Feb 2000)

Table 6: Coverage and availability of spaceborne SAR data sets which can be relevant for the project SMART.

3.3 Purchase Decision

There is just one sensor that can deliver high resolution data of less than 5m and in the favoured time interval until the end of 1995. Only KVR-1000 data fulfil both requirements. If one allows the sensor to deliver data of up to 10m spatial resolution and includes the years 1996 and 1997 into the possible time interval, SPOT 1-4, IRS-1 C/D, and Radarsat-1 in fine

mode can fulfil the criteria too. Especially the quality of IRS data should be checked before ordering because of its low radiometric resolution. All these sensors have collected data that cover all test areas in the SMART project and can be a possible choice therefore.

Since the KVR-1000 data are the only ones that fulfil the strict requirements of having less than 5m spatial resolution and a coverage of the area earlier than the end of 1995, a decision was taken to purchase these data. On 11 June 2002 three orthorectified KVR-1000 images of the test areas Glinska Poljana, Pristeg and Ceretinci were ordered by TRASYS and were delivered to the partners on 23 August 2002. Each orthorectified image costs $US 1400,- .

Further information concerning the available satellite data can be found in the deliverable D1.1.

4 Zeppelin Feasibility Study

4.1   First Test Measurement Campaign on the Zeppelin Platform on 18/09/2002

Originally, the Zeppelin test measurements were planned for spring 2002 but it was postponed because a key person at DLR got ill. Although at the beginning three to four weeks of illness were expected it took him four months to recover. Since the Zeppelin test measurements were not seen as being time-critical, they were shifted until this key person was at work again.

On 10/06/2002 a meeting between Zeppelin and DLR has taken place at Zeppelin in Friedrichshafen/Germany. The airship has been inspected with regard to the possibilities of installing the Daedalus and RMK sensors. There are two possibilities to install sensors at the Zeppelin, one inside the gondola and one below the bow outside of the gondola. There is no possibility to create a second opening in the floor of the gondola to install a third sensor for simultaneous data recording without an extremely high effort for the modification. Therefore it was decided to use the opening in the floor for the RMK camera and the Daedalus scanner and change the instruments during the flight. It was not expected that the small time delay in between the recorded data causes problems. Since it was not known at that time if CCMAT contributes to the measurements with their CASI hyperspectral scanner, the possibility was kept of installing the CASI scanner below the bow.

At that meeting it was decided to test the equipment in several steps in order not to get problems with the data exchange between the platform and the sensors during the planned measurement campaign in Croatia:

- the sensors should be placed in the Zeppelin on the ground to test the power and data connections.
- test measurements should be carried out in Germany to analyse the behaviour of the airship as sensor platform and to make sure that all needed data is recorded and of good quality.
- finally a measurement campaign in Croatia should be carried out to collect data over the same test areas as at the measurement campaign of August 2001. A direct comparison of the results of the developed tools should show the improvements (and/or drawbacks) of using remote sensing data with sub-meter resolution.

In the discussion all partners agreed that this procedure gives the maximum security of collecting good data and should be followed therefore. In between each step there should be some weeks in which possible problems can be solved.

It turned out that CCMAT could not participate at the first test measurements due to financial problems. Their participation at later measurements was left open.

On 03/09/2002 DLR installed the RMK and Daedalus sensors into the Zeppelin airship on the ground. Power and data connections were tested and the installation was inspected for flight security.

On 17/09/2002 a test field was prepared at the airfield Memmingerberg/Germany. A plastic tarp with a pattern of black and white bars of different sizes was laid out and several different

AP-mines were placed at the grass surface near the runway. The tarp is used for an analysis of the spatial resolution of the Daedalus sensor, the mines are used for information about the detectability of sub-pixel sized objects in a homogeneous area. The spatial resolution of the Daedalus sensor from 100m altitude is about 30cm, AP mines are in the range of 5-10cm. In the afternoon, the sensors were installed in the Zeppelin airship and the functions were tested.

On 18/09/2002 the flight test took place. RMK and Daedalus data of a stripe along the runway was collected, the tarp and the mines are within this stripe. GPS measurements of several points on the ground were carried out to get fixed points for a data correction without using flight attitude data. Several passes along the runway were flown in two different altitudes: 100m and 300m above ground. The data from 300m above ground can be compared easily with the data of the measurement campaign in Croatia of August 2001. The data from 100m above ground can show the increased spatial resolution. Additionally, this data shows the necessity of a very good correction of the flight attitude. The motion compensation was done with the available navigation and flight attitude data from the Zeppelin navigation instruments. The compensated Daedalus data stripes have still errors of several meters which can be seen at the undulations of the (in reality straight) runway. The cockpit data has a high time resolution but the measured values, especially the position is very coarse. The data is created for aeronautical purposes where its precision is sufficient. For data compression, all information which is unnecessary for navigation is being deleted. As an example the indication of the north coordinates are truncated to an accuracy of 0,006 degrees (approximately 670m). For motion compensation of the Daedalus data this accuracy is not high enough, an extra position and flight attitude data recording system has to be used.

Since it has become clear that it is necessary to use a differential GPS and inertial navigation system for the correction of the data, a second test measurement campaign having this equipment (IGI-system) on board had to be carried out.

Further information about the first Zeppelin test measurement campaign can be obtained at D1.3 "Report on Zeppelin Measurement campaigns".

4.2 Second Test Measurement Campaign on the Zeppelin Platform on 26/02/2003

From the first test measurements in September 2002 it was found that the available position and flight attitude cockpit data of the Zeppelin-NT is not precise enough for a data motion compensation of good quality. Therefore a second measurement campaign was carried out where the position and flight attitude data was recorded with the needed accuracy additionally to the remote sensing data.

DLR owns a differential GPS and inertial navigation system (IGI-system) which should have been installed together with the Daedalus sensor and the RMK camera on board of the Zeppelin-NT at a second Zeppelin test flight in December 2002. Unfortunately, the IGI-system broke down in November and had to be repaired at the manufactory. Therefore the second test flight had to be moved and was carried out on 26 February 2003. The weather situation was very stable without clouds and with only few wind. The accomplishment of two tests in very different weather situations (turbulent weather in September due to thermals, settled weather in February) allows us to analyse the behaviour of the Zeppelin-NT as a possible sensor platform in different weather situations.

The measurement campaign in Croatia which was planned for spring had to be cancelled by Zeppelin due to high transfer costs. The transfer would need approximately 25 flight hours, leaving only 7 flight hours left for data collection.

The behaviour of the Zeppelin-NT therefore was tested completely in Germany, the Zeppelin feasibility study was prepared with that information. The flight campaign in Croatia would allow to have optical data of known areas with a three times better resolution than from the flight campaign of August 2001. It would be a strong gain for SMART to analyse such data, and to compare the results of the developed tools for Zeppelin data and for the data of the measurement campaign in August 2001 but all requirements of the SMART contract can also be fulfilled without the Zeppelin measurement campaign in Croatia.

Further information about the Zeppelin test measurement campaign can be obtained at D1.3 "Report on Zeppelin Measurement Campaigns".

4.3   Zeppelin Feasibility Study

The data collected during the two Zeppelin measurement campaigns has been analysed with respect to the usability of the Zeppelin-NT airship as sensor platform for remote sensing applications in very low altitudes, e.g. for level-1 surveys in demining.

Information about the Zeppelin-NT airship (technical data, load, range and endurance, requirements for landing, take-off and mooring) was collected. The possibilities and restrictions for the installation of equipment are presented in the feasibility study. The sensors used during the Zeppelin measurement campaigns (Daedalus multispectral scanner and RMK metric camera, IGI CCNS differential GPS and inertial motion unit) are described, the collected data are presented and analysed. Daedalus data of the Friedrichshafen test area has been geocoded and mosaicked, the mosaic has been analysed with respect to the displacement of objects at the borders of two data stripes. The influence of the different parameters which are of importance for the Daedalus data quality has been calculated and compared with the collected flight attitude data. Recommendations are given for future Zeppelin-NT measurement campaigns to assure that a good data quality can be obtained.

pass	real altitude (GND, [m])	max. height deviat. [m]	ground speed [m/s]	max. over-speed [m/s]	yaw angle range [°]	max. roll angle deviat. [°]	max. pitch angle deviat. [°]	max. yaw rate [°/s]	max. roll rate [°/s]	max. pitch rate [°/s]
1	265 - 319	35	17.6 - 19.3	1.3	13	5.5	6.5	1.7	3.8	1.9
2	271 - 309	29	17.4 - 19.4	1.4	12	3.5	13.0	1.7	3.2	1.9
3	284 - 313	16	17.5 - 19.2	1.2	6	4.0	5.0	1.4	3.0	1.6
5	83 - 98	17	8.0 - 20.5	2.5	250	10.0	11.0	5.8	3.2	1.8
6	107 - 116	16	17.1 - 17.9	-	14	9.5	4.5	2.5	4.8	1.5
7	97 - 113	13	15.0 - 20.5	2.5	13	8.0	6.0	1.8	4.3	2.0
8	94 - 111	11	17.2 - 19.2	1.2	6	10	5	1.3	3.9	2.0

Table 7: Flight attitude data overview of the Zeppelin-NT during the measurements on 18/09/2002. Green colour shows parameter values which are well inside the needed ranges, yellow colour indicates values which still can be used and in red the parameter values are coloured which lie outside the specified borders.

pass	altitude (GND, [m])	max. height deviat. [m]	ground speed [m/s]	max. over-speed [m/s]	yaw angle range [°]	max. roll angle deviat. [°]	max. pitch angle deviat. [°]	max. yaw rate [°/s]	max. roll rate [°/s]	max. pitch rate [°/s]
3	95 - 110	10	21.2 - 24.9	0.9	29	9.5	4.0	3.8	3.5	0.8
4	103 - 121	21	22.1 - 26.1	2.1	15	12.0	2.5	4.6	4.8	0.7
5	95.2 - 96.7	4.8	24.5 - 25.8	1.8	7	5.0	1.5	1.1	2.3	0.6
6	100 - 121	21	23.4 - 26.0	2.0	11	7.5	5.0	2.2	2.6	0.5
7	95 - 112	12	22.2 - 25.0	1.0	10	2.5	6.0	1.2	0.9	1.0
8	98 - 137	37	21.9 - 26.7	2.7	6	4.0	8.5	0.9	2.5	1.0
9	89 - 118	18	20.6 - 26.5	2.5	15	12.0	5.0	4.5	4.5	0.9

Table 8: Flight attitude data overview of the Zeppelin-NT during the measurements on 26/02/2003. Green colour shows parameter values which are well inside the needed ranges, yellow colour indicates values which still can be used and in red the parameter values are coloured which lie outside the specified borders.

4.3.1 Conclusions and Recommendations

The Zeppelin-NT airship was tested for measurements with the Daedalus multispectral scanner and the RMK metric camera in two measurement campaigns at different weather situations. Three main conclusions can be drawn:

- **The Zeppelin-NT airship can be used as a sensor platform for remote sensing.**

  The Zeppelin-NT airship provides enough space for the sensors, the equipment, and the operators. The doors are large enough to allow an easy loading and unloading of bulky equipment. The airship is able to carry considerably more weight as was necessary for the test measurements. The needed electrical power for the equipment can be provided by the airships power system. If more than one sensor is used at the measurement campaign, a second opening in the gondola floor should be created.

  The flight character of the Zeppelin-NT allows its use as a sensor platform for both tested sensors. The stability of the platform depends directly on the weather conditions. In stronger wind conditions it is not very stable but the flight attitude variations have maximum values which can be compensated. Large amplitudes of high frequency pitch rates which are sometimes a problem when using an airplane as sensor platform have not been found during the Zeppelin-NT measurements. The critical parameter was the large variation in altitude at most of the flight passes. It is very probable that the size of the

altitude variations can be reduced if the pilots have several flight hours of experience with the special requirements of a data collection flight and if the weather is calm. An automatic height control system could help to minimise the height variations.

- **It is possible to use the Zeppelin-NT airship for airborne scanner measurements in low altitudes at low speed. The spatial resolution of the data can be increased considerably compared to an aircraft as sensor platform.**

  The needed flight time to cover an area increases strongly at low altitudes due to two reasons: The speed has to be reduced to avoid gaps in the scanner data and the stripe width of the scanner data is smaller. The data size increases quadratic with the resolution and since more details are visible, the homogeneity of areas is reduced. This leads to more effort in the data processing and data analysis. Therefore an analysis should be made previous to a measurement campaign to find out which spatial resolution of the data is necessary. If data of sufficient resolution can be acquired using an aircraft as sensor platform it is very probable that because of the reduced flight time the measurement campaign becomes less expensive than using the Zeppelin-NT airship. If the data need to have a higher resolution than can be provided using an aircraft, then using the Zeppelin-NT as sensor platform is a good choice which allows to collect the needed data.

- **The mapping of a predefined area is possible.**

  With a dGPS based flight guidance system and an experienced pilot it is possible to record scanner data along parallel flight tracks and merge the data stripes into a mosaicked data set. Due to the large possible roll angles of the Zeppelin-NT airship a large overlap in between two data stripes has to be planned which leads to an increased number of data stripes. For a good geocoding quality of data with sub-meter resolution great efforts are necessary to measure the position and flight attitude of the sensor platform.

If a future measurement campaign is planned, the following recommendations should be considered:

- A stabilised platform should be used which can compensate roll and pitch motions up to 5°. If larger motions occur, the stabilised platform reduces the motion angles by its maximum correction angles.

- For the best possible absolute position accuracy in real-time, an Omnistar receiver including an extra antenna on top of the hull should be installed. Omnistar allows real-time dGPS measurements with an accuracy of 1-3m.

- For the best possible absolute position accuracy in postprocessing a differential GPS system should be used with a L1/L2-band antenna on top of the airships hull and a geodetic base station on the ground at or near to the measurement area. Only with L1/L2-band differential GPS an accuracy of kinematic position measurements in the range of decimetres can be achieved in postprocessing.

- The GPS base station should be used to measure the coordinates of ground control points for a calculation of the boresight misalignment angles of the multispectral scanner.

- The flight tracks should be planned with some hundred meters reserve in front of the measurement area to allow the pilots to bring the airship exactly to the correct flight track and airspeed.

The Zeppelin feasibility study has been produced by DLR and Zeppelin Luftschifftechnik. Further information can be obtained at D1.6 "Report on Zeppelin Feasibility Study".

5 Tool Development

5.1 Detection of Defence Positions in the Pristeg Area

Defence positions are small shelters of few square meters size, either dug into the ground or protected by a piling of stones. Since the ground in the Pristeg test area is very rocky, it is hard to dig into it and defence positions are mostly build on the surface and therefore more easy to detect than in data of the other test areas where the fertile soil can easily be excavated. Fig.10 shows a georeferenced RMK aerial view with two defence positions of approx. 3m x 3m size. Geocoded E-SAR L-band data of the same area are shown in fig.11. A road is visible as a dark line, a trench as a bright line and the defence positions are bright parts along the trench. The trench has no vertical walls but slopes, therefore the incoming radar energy is scattered back partly from single bounce, partly from double bounce reflections. Since the trench is running nearly parallel to the flight direction, much more of the energy is scattered back from the trench than from the horizontal ground giving a bright appearance in the image.

The northern defence position in fig.10 and fig.11 has only very low walls while the southern one has no walls at all but seems to have only a natural slope covered with wood towards the front line. Both places are only slightly larger than the resolution of E-SAR L-band data, so only few pixels carry information about them. Since they are not real buildings but appear more like disturbed ground and their backscatter properties are orientation dependent, it is hard to find common properties in the SAR data except that they are connected with a trench for secure access. Bulges along a trench can be used as indicators for defence positions, but no unique characteristic could be found to be used for an algorithm that extracts defence positions.
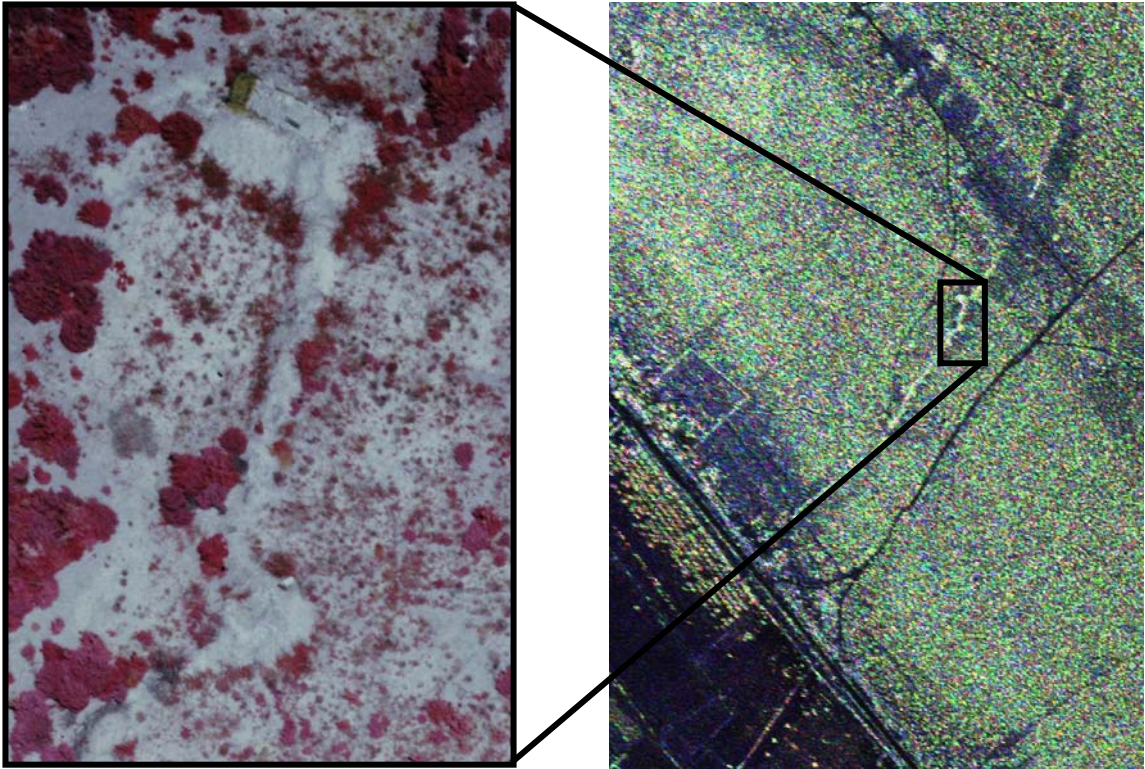
Fig.10: Subset of the geocoded RMK aerial view no.457 showing defence positions along a trench north of Pristeg.

Fig.11: Geocoded E-SAR L-band SLC data in Pauli decomposition. Flight direction was approximately from upper right to lower left corner.
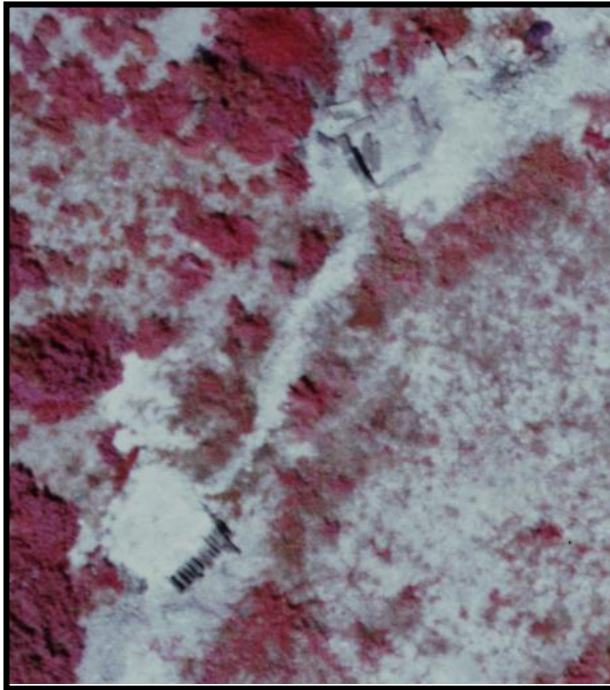
Fig.12: Subset of the geocoded RMK aerial view no.457 showing defence positions along a trench north of Pristeg.

Fig.13: Geocoded E-SAR L-band SLC data in Pauli decomposition. Flight direction was approximately from upper right to lower left corner.
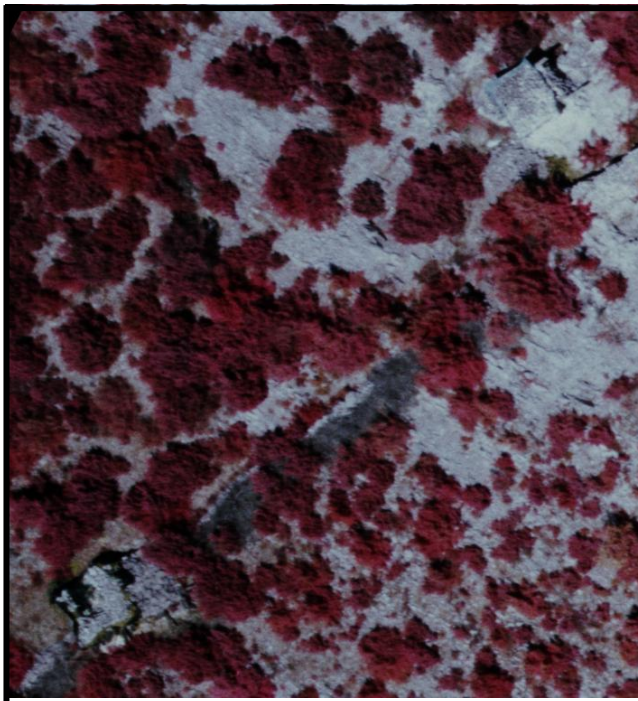
Fig.14: Subset of the geocoded RMK aerial view no.457 showing defence positions along a trench north of Pristeg.

Fig.15: Geocoded E-SAR L-band SLC data in Pauli decomposition. Flight direction was as in fig.13.
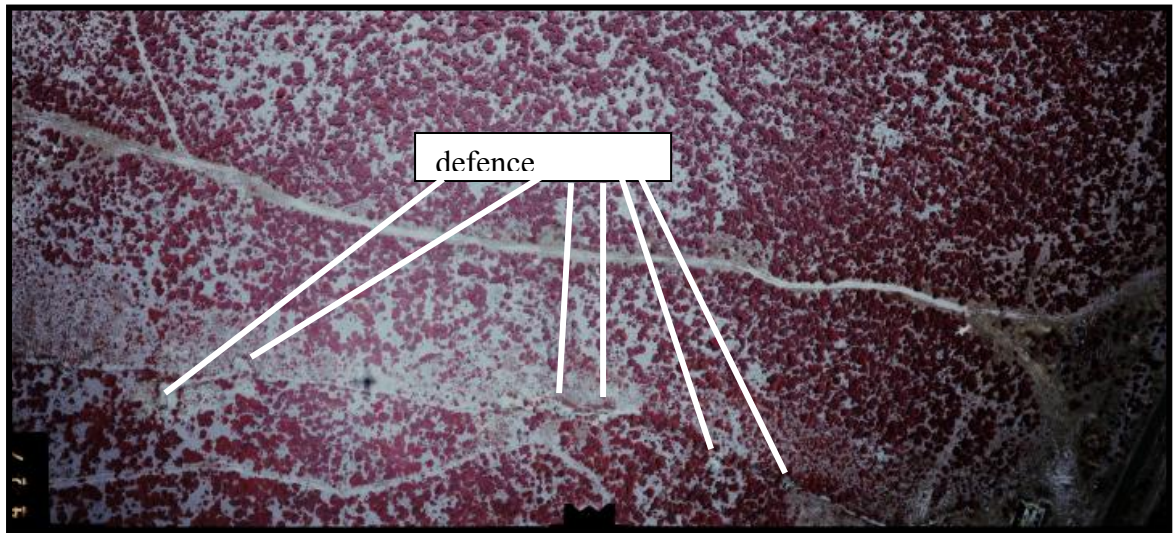
Fig.16: Part of the RMK aerial view no.457 (not geocoded) with the defence positions shown in fig.10-15 along a trench.
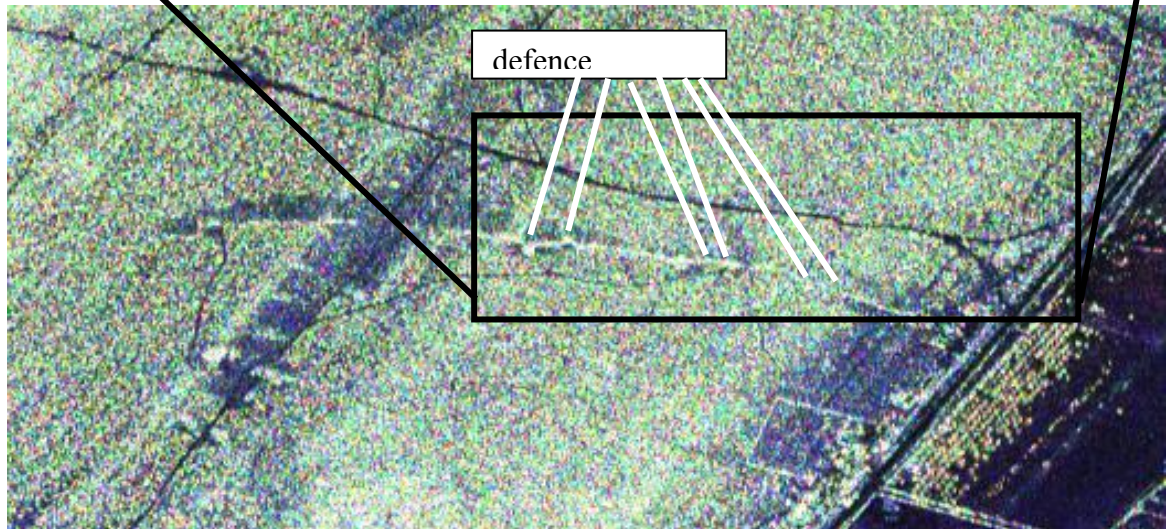
Fig.17: Slant range E-SAR L-band SLC data in Pauli decomposition (not geocoded) with the defence positions shown in fig.10-15 along a trench. The flight track was beneath the image, flight direction was from left to right.

5.2   Search for Known Mines in RMK Data

CROMAC distributed GPS coordinates of mines which were found during the demining in the Pristeg test area to the partners. The demining took place after the data collection has been ended, so the airborne data shows the ground undisturbed by demining. One scanned RMK aerial view, which covers most of the demined area was geocoded, and at the given mine positions the geocoded image was inspected for any visible evidence for the presence of a mine. Since the ground in the Pristeg region is very rocky, most of the mines are laid on the ground and should be detectable in high resolution airborne photography if they are not covered by vegetation. The vegetation consists mostly of bushes which cover about 50% of

the earths surface. Although many of the given coordinates are of uncovered places, no anomaly or direct indicator for mines could be found. This can have different reasons:

- Since no information was given from the deminers which mines were laid on the surface and which were buried, it is possible that all mines were either buried or covered by bushes so they can not be detected by airborne photography.

- The given GPS coordinates were probably collected by a handheld GPS and not by a much more accurate geodetic GPS. With a handheld GPS, the horizontal accuracy is in the range of several meters, depending on the duration of the measurement, the satellite constellation, and the covering of the signal by objects, while with a geodetic GPS a horizontal accuracy of several centimetres can be achieved. A mine position which is wrong by several meters can make the identification impossible.

- The geocoding of the RMK image was done by using the available DEM which is not very precise. For this reason an offset of some meters from the true coordinates is possible.
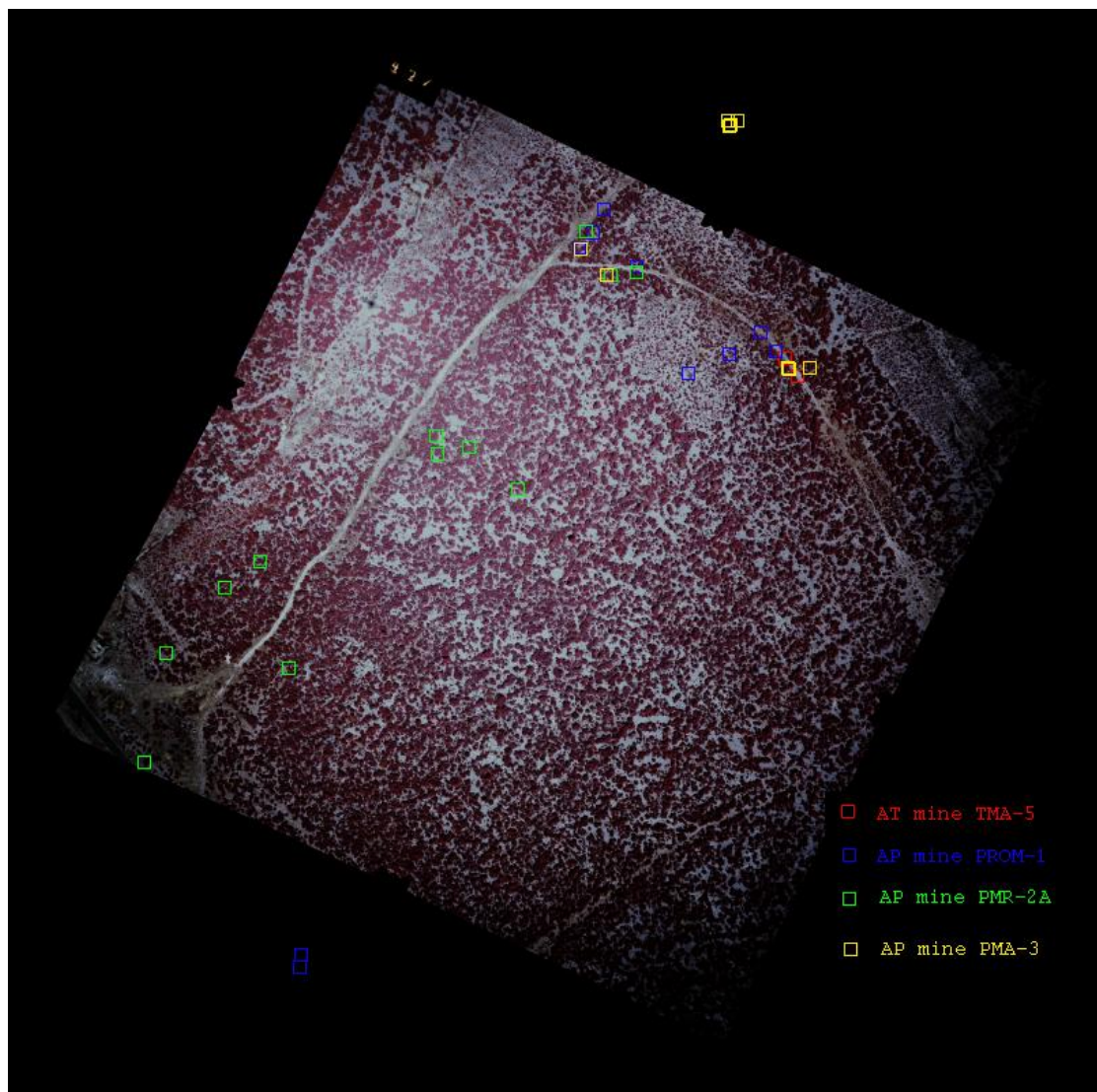
Fig 18: Geocoded RMK aerial view with mine positions

5.3 Geocoding and Mosaicking of Daedalus Data

Aerial survey with a multispectral scanner requires the generation of image mosaics, which are usually composed of several image strips. The quality of the produced mosaic depends mainly on the radiometric and geometric characteristics of individual image strips after the correction.

Especially airborne data obtained from sensors having a wide field of view (e.g. up to 90 degrees) exhibit substantial viewing angle dependence of radiances across the image swath width due to illumination, atmospheric conditions, and BRDF of different objects. Usually these radiometric corrections are derived by physical modeling (OLBERT 1998, RICHTER et al. 2002), which requires in-situ field and atmospheric measurements during the acquisition of the image data. Since in many cases such measurements are not performed simultaneously during aircraft overflight, empirical methods are necessary to achieve radiometrically homogeneous image data. Under the assumption of a stable and homogeneous atmosphere (justified for airborne data) the main radiometric distortions across an image strip are resulting from the variation of the sensor viewing angle (STAENZ et al. 1986, KENNEDY et al. 1997). To perform relative normalization of these radiometric distortions within the image strip an image-based empirical radiometric correction method EMRACO (PALUBINSKAS et al. 2002, PALUBINSKAS et al 2003) is used.

After the radiometric normalization the individual strips are ortho-rectified using a direct georeferencing software RECTIFY (MÜLLER et al. 2002), which takes into account the following parameters: the exterior (measured by an IGI AEROcontrol CCNS IIb) and interior orientation of the imaging system, the topography of the earth surface, the boresight misalignment angles between navigation sensor and camera system and the mapping coordinate reference system. One of the advantages of this approach in comparison with the conventional geometric transformation methods is that no ground control points are required.

Even if the individual image strips are radiometrically normalized, the seam line can be visible between the strips in the produced mosaic due to the change of the intensity and direction of solar illumination during the acquisition of adjacent image strips. Conventional mosaicking methods try to remove the between-strip radiometric variations by adjusting the mean, standard deviation values or histograms of the overlapping region. The seam line is drawn manually or goes through the tie points (e.g. found by using matching algorithm) (AFEK & BRAND 1998) in the overlapping region. Here another radiometric correction method RADMOS is used, which is based on the unsupervised clustering in the overlapping region of the image strips. The mosaicking of two image strips is performed along the seam line, which is drawn along the boundaries of clusters. Thus a seamless mosaic can be created.

Each of these three steps of the mosaicking procedure are presented below in more detail followed by the application to the airborne scanner data of this project.

From general considerations of radiation transfer from the ground target to the sensor (under some assumptions) the empirical image-based radiometric correction method EMRACO (PALUBINSKAS et al. 2002, PALUBINSKAS et al 2003) is used, which corrects the radiances of pixels at the sensor for sensor viewing angle effects and indirectly for BRDF effects of the surfaces. The radiance at any viewing angle (off-nadir) is normalized to the radiance at the selected reference angle, usually in nadir direction. In order to implement such type of

correction the objects (or classes or surface types) to be extracted from the image data are needed.

It can be assumed, that in some region of an image, around the reference angle (nadir), the pixel values are not or minimally distorted. This assumption is valid for nadir-looking sensors.

This selected region of the image (usually symmetric on both sides of nadir) is used to initialize the whole procedure, which consists of several steps. First, the initial region of an image is clustered by an extended k-means algorithm, which defines automatically the number of clusters (classes) depending on the complexity of an image (PALUBINSKAS 1999). Then for each cluster an average intensity profile along the scan direction is calculated. These profiles (initially defined in a central part of an image line) are extrapolated to the whole swath width of an image by a polynomial approximation. Finally, applying a linear regression method over all clusters to the radiation transfer equation results in a radiometric correction function for each sensor viewing angle with which the pixel intensity across the scan line can be relatively adjusted to the pixel intensity of the reference viewing direction. The procedure is iterative, that is the correction is first performed for a narrow central part of an image. Then the procedure is initialized with this corrected image region and repeated until the whole image swath width is corrected. This object-based correction method allows a relative correction of the local radiometric distortions.

The line scanner imagery are geometrically distorted with respect to a mapping frame. The upcoming high precision direct georeferencing systems consisting of a combined GPS/IMU and one or more imaging sensors can be used for orthoimage production provided a digital elevation model (DEM) is available in the case of single imagery. The utilization of direct measurements of the image exterior orientation parameters by a GPS/IMU system for image rectification is called Direct Geo-referencing and allows a fast automatic ortho-rectification of the remotely sensed data. The basic concept of direct georeferencing, addressed by various
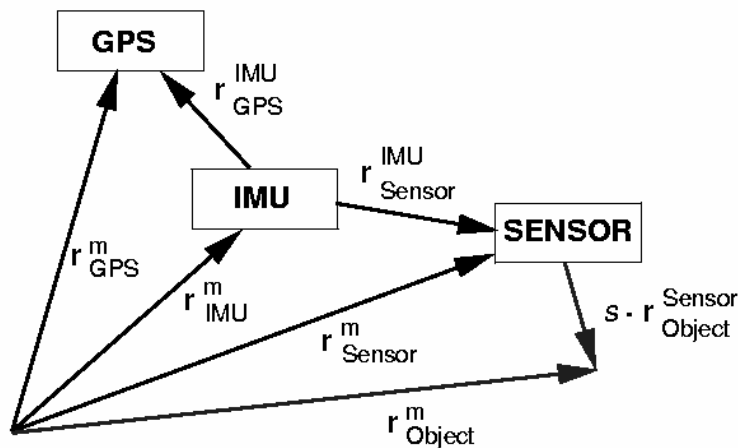
Fig 19: Concept of direct georeferencing.

authors in the last years (BÄUMKER & HEIMES 2001, CRAMER & STALLMANN 2001, ELLUM & EL-SHEIMY 2002, GRIMM 2001, JAKOBSEN & WEGMANN 2001, MOSTAFA 2001, MÜLLER et al. 1999, MÜLLER et al. 2002) is illustrated in Fig. 19.

The collinearity concept is the basis for all direct georeferencing formulas, where the coordinates of an object point r_{Object}^{Sensor} measured in the imaging sensors coordinate frame are related to the coordinates r_{Object}^{m} in the mapping coordinate frame

$$r_{Object}^{m} = r_{Sensor}^{m} + s \cdot R_{IMU}^{m} R_{Sensor}^{IMU} \cdot r_{Object}^{Sensor} ,$$

with the actual position of the projection center of the sensor

$$r_{Sensor}^{m} = r_{GPS}^{m} - R_{IMU}^{m} \cdot r_{GPS}^{IMU} + R_{IMU}^{m} \cdot r_{Sensor}^{IMU} .$$

The lower indices of the vectors r indicate the position of the points, whereas the upper indices denote the coordinate frame in which the vector is measured. The notation of the indices of the rotation matrices R indicates the transformation direction where the lower index represents the source system and the upper index the destination system.

In a first step of the orthoimage production the six parameters of the exterior orientation (position and attitude data normally corrected by the lever arm calibration values) are synchronized with each image line. As input for the orthoimage processor serves the exterior orientation for each scan line, the model of the sensor (whiskbroom or pushbroom system) in combination with the calibrated interior orientation and a digital elevation model (DEM). Applying the rigorous collinearity equation the intersection point of each sensor look direction with the DEM is iteratively calculated. The resulting irregular grid is filled with bilinear interpolated pixel values. The orthoimage processor RECTIFY (MÜLLER et al. 2002) supports a multitude of map projections (including local topocentric or ECEF coordinate systems) and geodetic datum transformations as well as ellipsoid to geoid transformations.

To remove the radiometric variations between image strips the radiometric correction method RADMOS is used, which is based on the information contained in the overlapping region of the images. First, the overlapping region is clustered by an extended k-means clustering algorithm, which automatically detects the different clusters (surface classes) in the region (PALUBINSKAS 1999). Then, the means of the clusters, calculated for each image strip separately, are used in the linear regression to derive the linear dependence between the radiances in the two image strips. This linear transformation is used for the radiometric normalization of image strips before the mosaicking. Finally, the mosaicking of two image strips is performed along the seam line, which is drawn along the boundaries of clusters, found after the unsupervised clustering in the overlapping region of the two image strips. The whole mosaicking procedure is fully automatic and does not require any manual user interaction.

As an example of the results in the SMART project, figure 20 shows a part of a mosaicked image of 5 Daedalus strips, where all the above mentioned procedures have been used. It shows that a really homogenous image ortho map can be created and used for further processing like classification or texture derivation (see chapter 5.12)

Fig 20: Geocoded and mosaicked Daedalus image (Glinska Poljana), no geometric or radiometric step values can be seen.

K. Staenz, P. Meyer, K.I. Itten, D.G. Goodenough, and P.M. Teillet, "Viewing angle corrections of airborne multispectral scanner data acquired over forested surfaces", Proceesings of IGARSS'86 Symposium. ESA, Noordwijk, The Netherlands, vol. 1, pp. 671-676, 1986.

R.E. Kennedy, W.B. Cohen, and G. Takao, "Empirical methods to compensate for a view-angle-dependent brightness gradient in AVIRIS imagery", Remote Sensing of Environment, vol. 62, pp. 277-291, 1997.

G. Palubinskas, R. Müller, and P. Reinartz, "Radiometric normalization of optical remote sensing imagery", Proceedings of IGARSS'03 Symposium, Toulouse, France, 2003.
G. Palubinskas, "An unsupervised clustering method by entropy minimization", In Maximum Entropy and Bayesian Methods, W. von der Linden, V. Dose, R. Fischer and R. Preuss, Eds., Dordrecht: Kluwer Academic, 1999, pp. 327-334.

Bäumker, M., Heimes, F.J., New Calibration and Computing Method for Direct Georeferencing of Image and Scanner Data Using the Position and Angular Data of an Hybrid Inertial Navigation System, *OEEPE Workshop, Integrated Sensor Orientation*, Hannover 2001

Cramer, M., Stallmann, D., On the use of GPS/inertial exterior orientation parameters in airborne photogrammetry, *OEEPE Workshop, Integrated Sensor Orientation*, Hannover 2001

Ellum, C.M., N.El.Sheimy, Land Based Mobile Mapping System, *Photogrammetric Engineering & Remote Sensing*, Jan. 2002, pp. 13-17

Grimm, A., Results of the integrated CCNS AEROcontrol System, *OEEPE Workshop, Integrated Sensor Orientation*, Hannover 2001

Jacobsen, K., Wegmann, H., Dependicies and Problems of Direct Sensor Orientation, *OEEPE Workshop, Integrated Sensor Orientation*, Hannover 2001

Mohamed Mostafa, Direct Georeferencing Column: An Introduction, *Photogrammetric Engineering & Remote Sensing*, Oct.2001, pp. 1105-1109

Müller, Ru., Lehner, M., Reinartz, P., Schroeder; M., Procedures for geometric rectification of airborne scanner data, *Proceedings of Workshop on In-orbit characterization of optical image systems*, Bordeaux Nov. 1999, 9 pages

Rupert Müller, M. Lehner, Rainer Müller, P. Reinartz, M. Schroeder, and B. Vollmer, "A program for direct georeferencing of airborne and spaceborne line scanner images", Proceedings of ISPRS Commission I Mid-Term Symposium, ISPRS, Denver, 2002.

5.4 Geocoding of E-SAR Processing Results in Slant Range Geometry

For polarimetric and interferometric SAR data analysis only SLC data can be used which is in slant range geometry and not geocoded. Since SLC data consists of amplitude and phase (complex data), a resampling of the data to geocoded geometry will change the phase values and so the polarimetric and interferometric information will be changed too. Therefore this step should be avoided. Instead, a resampling of the results of polarimetric and interferometric analysis should be done, when no further processing is necessary any more. This makes it possible to fuse polarimetric and interferometric information with information from other sources like maps, GIS data, or geocoded E-SAR and Daedalus data. An algorithm to geocode polarimetric and interferometric analysis results has been developed, all polarimetric and interferometric processing results can be made available now as geocoded data.

In fig.21a-22b colour composites of slant range and geocoded interferometric coherence data in L- and P-band of the Pristeg test area are displayed as examples. The red channels show the coherence between the horizontal polarisations (hh) of the interferometric pair of E-SAR data, in the green channels the crosspolar (hv and vh) coherence can be seen, and the blue channels show the coherence between the vertical (vv) polarisations of the interferometric pair. The range of coherence data is in between 0 and 1, 1 meaning a perfect stability of the scatterer in between the two data recording passes of the aircraft, and 0 meaning no relation of the backscattered signals of the two passes. Areas that show colours have a polarisation dependence of the coherence. The purple regions for example show agricultural fields of bare

soil or covered with only a thin layer of vegetation. Since there is not much volume scattering of the vegetation cover, only a low crosspolar signal (hv- and vh-channel) is scattered back, while the hh- and vv-channel have a much stronger signal due to surface scattering on the ground. Due to the low backscattered crosspolar signal, the signal-to-noise level is low in these areas for hv and vh and therefore the scatterers appear unstable by the influence of noise. The coherence is high in the copolar channels (hh and vv), resulting in bright red and blue colours, while the green colour is dark, showing a low crosspolar coherence. The resulting colour in the composite is purple. Interferometric coherence data and results of polarimetric processing of the E-SAR L- and P-band SLC data is available in geocoded form for all test areas. The geocoding algorithm has been implemented into the other programs where the geocoding of SLC data processing results is necessary.
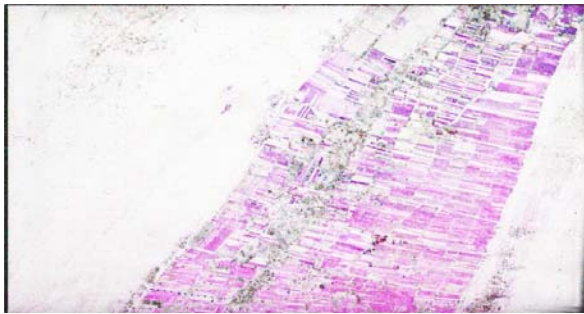
Fig.21a: Slant range colour composite of L-band repeat pass interferometric coherence E-SAR data of the Pristeg test area.

Red: hh-hh-coherence, green: hv-hv-coherence, blue: vv-vv-coherence
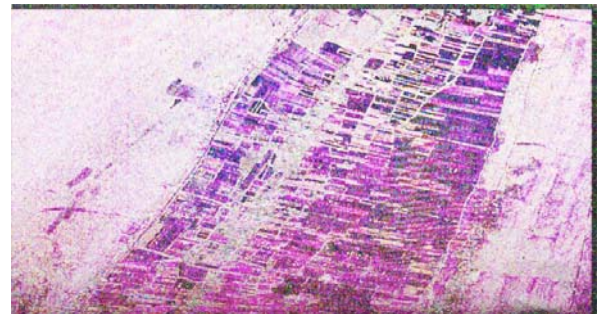
Fig.21b: Slant range colour composite of P-band repeat pass interferometric coherence E-SAR data of the Pristeg test area.

Red: hh-hh-coherence, green: hv-hv-coherence, blue: vv-vv-coherence
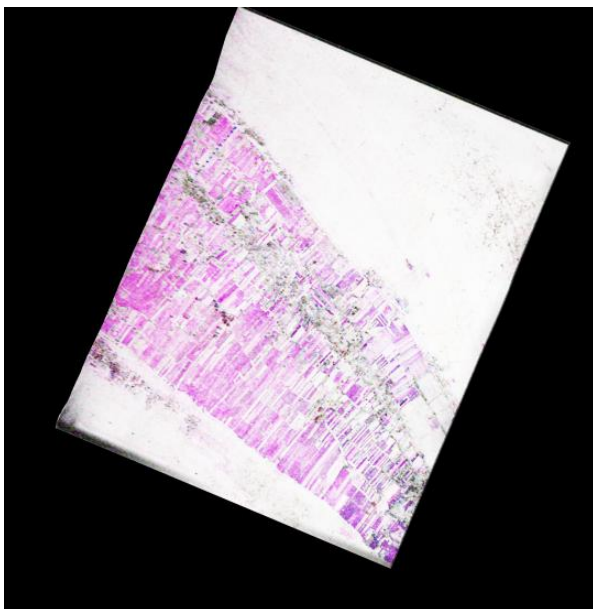
Fig.22a: Geocoded colour composite of L-band repeat pass interferometric coherence E-SAR data of the Pristeg test area.

Red: hh-hh-coherence, green: hv-hv-coherence, blue: vv-vv-coherence
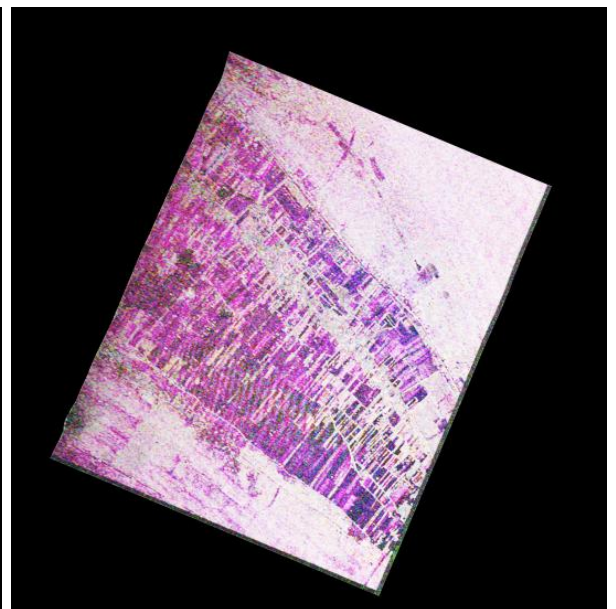
Fig.22b: Geocoded colour composite of P-band repeat pass interferometric coherence E-SAR data of the Pristeg test area.

Red: hh-hh-coherence, green: hv-hv-coherence, blue: vv-vv-coherence

5.5   E-SAR Data and Results in Daedalus Format

For a fused analysis of Daedalus and E-SAR data it is necessary that the information can be identified as coming from the same position. To assure not to mix information of different areas and to ease the working with the different data it is best to have the data available with the same geometry, format and pixel size.

The Daedalus data and the E-SAR amplitude data have been provided as geocoded data. The Daedalus data are delivered as 8-bit 12-channel data sets with the channels interleaved by line (BIL), while the geocoded E-SAR data are provided as 10 separate single-channel 16-bit data sets (1 X-band, 1 C-band, 4 L-band, 4 P-band). The geocoded E-SAR and Daedalus data both have a pixel size of 1m but do not cover exactly the same area.

Polarimetric and interferometric information is contained in fully polarimetric (all polarisations) and interferometric (interferometrically processed data of two passes) SLC data sets. The SLC data is in 64-bit complex float format with each polarisation saved in a separate file. The data is delivered in slant range geometry which has a non-linear spatial transformation connection to the geocoded data geometry. Therefore polarimetric and interferometric processing results have to be geocoded before they can be used together with Daedalus data.

For data fusion E-SAR data (X-, L-, P-band amplitudes, L-, P-band polarimetric and interferometric processing results) should be available in the same format as the Daedalus data. All the polarimetric and interferometric data processing can be done with the original slant range SLC E-SAR data, only the processing results are geocoded which minimises the introduction of resampling errors. Since the results are geocoded and byte-scaled, the data size is reduced significantly from 32-bit float data to 8-bit.

Altogether 23 channels of information have been provided in Daedalus format. Since the original Daedalus data set contains 12 channels, it was decided to distribute the 23 channels to two data sets of 12 channels each, leaving one channel empty.

The following data is saved in Daedalus format:

Data set 1:

channel 1: Geocoded X-band vv-polarisation amplitude data, byte-scaled

channel 2: Geocoded L-band hh-polarisation amplitude data, byte-scaled

channel 3: Geocoded L-band xx-polarisation amplitude data, byte-scaled. The xx-polarised (crosspolarised) channel was created by adding the complex values of the hv- and vh-polarised channels: xx = hv/2 + vh/2

channel 4: Geocoded L-band vv-polarisation amplitude data, byte-scaled

channel 5: Geocoded P-band hh-polarisation amplitude data, byte-scaled

channel 6: Geocoded P-band xx-polarisation amplitude data, byte-scaled

channel 7: Geocoded P-band vv-polarisation amplitude data, byte-scaled

channel 8: L-band polarimetric processing result: Square root of the first eigenvalue λ_1 (square root to reduce the strong contrasts), conversion from slant range to geocoded geometry, byte-scaled. The square root of λ_1 can be interpreted as the backscatter amplitude of the most important scattering mechanism.

channel 9: P-band polarimetric processing result: Square root of the first eigenvalue λ_1, conversion from slant range to geocoded geometry, byte scaled.

channel 10: L-band interferometric processing result: Coherency between two repeat pass data sets, conversion from slant range to geocoded geometry, byte scaled.

channel 11: P-band interferometric processing result: Coherency between two repeat pass data sets, conversion from slant range to geocoded geometry, byte scaled.

channel 12: empty

Data set 2:

channel 1: L-band polarimetric processing result: Entropy H, conversion from slant range to geocoded geometry, byte scaled.

channel 2: L-band polarimetric processing result: α-angle, conversion from slant range to geocoded geometry, byte scaled.

channel 3: L-band polarimetric processing result: H*A [Entropy times Anisotropy], conversion from slant range to geocoded geometry, byte scaled. H*A is large for areas with two scattering mechanisms of similar size($\lambda_1 \approx \lambda_2, \lambda_3 \approx 0$).

channel 4: L-band polarimetric processing result: H*(1-A), conversion from slant range to geocoded geometry, byte scaled. H*(1-A) is large for areas with no dominant scattering mechanism ($\lambda_1 \approx \lambda_2 \approx \lambda_3$).

channel 5: L-band polarimetric processing result: (1-H)*A, conversion from slant range to geocoded geometry, byte scaled. (1-H)*A is large for areas with two scattering mechanisms but one of them dominating ($\lambda_1 >> \lambda_2, \lambda_3 \approx 0$).

channel 6: L-band polarimetric processing result: (1-H)*(1-A), conversion from slant range to geocoded geometry, byte scaled. (1-H)*(1-A) is large in areas with one single scattering mechanism ($\lambda_2 \approx \lambda_3 \approx 0$)

channel 7: P-band polarimetric processing result: Entropy H, conversion from slant range to geocoded geometry, byte scaled.

channel 8: P-band polarimetric processing result: α-angle, conversion from slant range to geocoded geometry, byte scaled.

channel 9: P-band polarimetric processing result: H*A, conversion from slant range to geocoded geometry, byte scaled.

channel 10: P-band polarimetric processing result: H*(1-A), conversion from slant range to geocoded geometry, byte scaled.

channel 11: P-band polarimetric processing result: (1-H)*A, conversion from slant range to geocoded geometry, byte scaled.

channel 12: P-band polarimetric processing result: (1-H)*(1-A), conversion from slant range to geocoded geometry, byte scaled.

X-band, geocoded, amplitude, vv-pol.

L-band, geocoded, amplitude, hh-pol.
L-band, geocoded, amplitude, hv-pol.
L-band, geocoded, amplitude, vh-pol.
L-band, geocoded, amplitude, vv-pol.

P-band, geocoded, amplitude, hh-pol.
P-band, geocoded, amplitude, hv-pol.
P-band, geocoded, amplitude, vh-pol.
P-band, geocoded, amplitude, vv-pol.

L-band, slant range, SLC, hh-pol.
L-band, slant range, SLC, hv-pol.
L-band, slant range, SLC, vh-pol.
L-band, slant range, SLC, vv-pol.

P-band, slant range, SLC, hh-pol.
P-band, slant range, SLC, hv-pol.
P-band, slant range, SLC, vh-pol.
P-band, slant range, SLC, vv-pol.

L-band, sr, SLC, hh-pol., interf. slave
P-band, sr, SLC, hh-pol., interf. slave

xx = hv/2 + vh/2

xx = hv/2 + vh/2

xx = hv/2 + vh/2

xx = hv/2 + vh/2

3-channel, polar. SLC-data (Lhh, Lxx, Lvv)

2-channel, interf. SLC-data (Lhh1, Lhh2)

3-channel, polar. SLC-data (Phh, Pxx, Pvv)

2-channel, interf. SLC-data (Phh1, Phh2)

Polarimetric proc.:
H/A/α-Decompos.
$\Rightarrow$ λ_1, H, α, HA, H(1-A), (1-H)A, (1-H)(1-A)

Interferometric proc.:
$\Rightarrow$ interferometric coherence γ

Slant range to geocoded geometry

Adaptation of the data window to the Daedalus data and conversion to byte format.

Data set 1 (12 channels, byte BIL format):

1: amp(Xvv), 2: amp(Lhh), 3: amp(Lxx),
4: amp(Lvv), 5: amp(Phh), 6: amp(Pxx),
7: amp(Pvv), 8: λ_1(L), 9: λ_1(P),
10: γ(Lhh1, Lhh2), 11: γ(Phh1, Phh2),

Data set 2 (12 channels, byte BIL format):

1: H(L), 2: α(L), 3: H(L)A(L),
4: H(L)(1-A(L)), 5: (1-H(L))A(L),
6: (1-H(L))(1-A(L)), 7: H(P), 8: α(P),
9: H(P)A(P), 10: H(P)(1-A(P)),

5.6   Power Line Pole Detector

Power lines are an important part of the infrastructure and therefore very often a target of mining activities. An automatic detection of power lines can be much more cost effective than the extraction by hand from old and not always accurate maps, especially when dealing with large areas.

Power line poles usually have a strong double bounce reflection (at the pole and the ground) in P-band, independent of the flight direction of the aircraft. They can be discriminated from tree trunks by the missing volume scattering of the tree crowns. An algorithm was developed which takes this into account. The signal of the wires of the power lines themselves was not used for the identification of the power lines because it is highly direction dependent. If the power line runs parallel to the flight direction, the wires are clearly visible in SAR data but in all other cases nearly no energy is backscattered to the sensor. Therefore only the power line poles are used for the detection.

Power line wires and poles are both too small to be identified by Daedalus data. Therefore, only SAR data is used in the algorithm. The implementation of polarimetric decomposition results like the entropy H might help to differentiate still better between trees and power line poles, but already now most of the poles can be detected and separated from trees.

After the detection of poles a Hough-transform was used by RMA to find aligned poles. These alignments can be identified with power lines.

The power pole detector consists of several different routines, developed by DLR and RMA. The detector was improved in a way that the routines work together without manual interaction. The coordinates of all resulting pixels which represent "power pole candidate pixels" are calculated and written into an ASCII-file which serves as input for RMAs algorithms. These routines read the ASCII-list, merge adjacent pixels to objects (power pole candidates) and run a Hough routine to find aligned objects.

Flow chart of the algorithm:

Read geocoded SAR data

↓

Scale values to byte values (0..255) to have the same range for all.

bytevalue = bytescale(min=0, max=2.5*mean(pixelvalues))

↓

Search for objects in pixel neighbourhood with high P-band double bounce and low L-band crosspol backscatter

P-band double bounce > 210 in 3x3 neighbourhood
L-band crosspol < 90 in 21x21 neighbourhood (no forests)
L-band crosspol < 170 in 5x5 neighbourhood (no single trees)
L-band crosspol ≠ 0 (no background)

↓

Delete very large and very small objects, and objects in forests and at forest borders

Delete large objects (> 80 pixels in 21x21 neighbourhood)
Delete remaining pixels in forests and at forest borders:
    Create Median1 of 9x9 neighb. in Lcross-and Pco-band
    Create Median2 for L-band pixels with values > Median1
    If Median2 > 160 then delete pixel (too much vegetation)
    Create Median2 for P-band pixels with values < Median1
    If Median2 > 70 then delete pixel (too much vegetation)
Delete small objects (< 10 pixels in 7x7 neighbourhood)

↓

Search aligned objects with Hough-transform

Algorithm by RMA

Fig.23: RGB composite of multifrequency geocoded E-SAR data of a part of the Glinska Poljana test area. Red: P-band, hh-polarisation, green: L-band crosspolar, blue: X-band, vv-polarisation. The crosspolar channel in L-band was used to get as much backscatter from the vegetation volume as possible, while a copolarised channel in P-band was used to have as much backscatter as possible from the double bounce reflection at the pole and the ground. Trees can be seen in the image as red spots from P-band double reflections of the trunk and the ground, surrounded by green parts (L-band) from the volume of tree crowns. Power line poles show no volume scattering and are visible therefore as pure red spots.
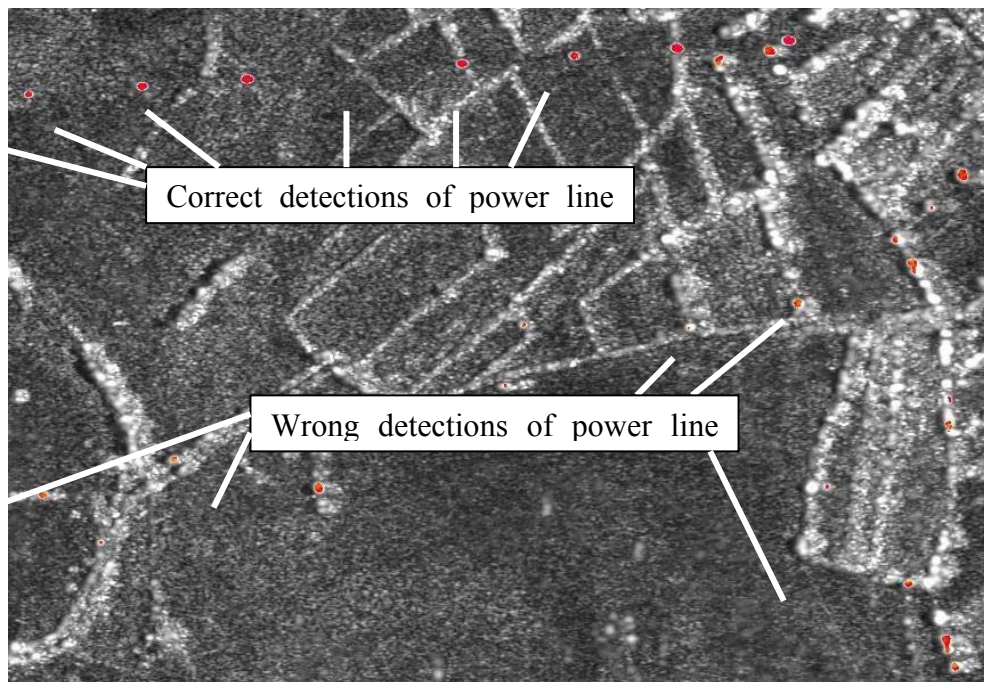
Fig.24: HSV (hue/saturation/value) colour composite. Hue and value come from the image in fig.23, the saturation channel is a mask created by the pole detection algorithm. Pixels where

poles were detected have full saturation. Pixels where no pole was detected are not saturated, only grey values are visible.
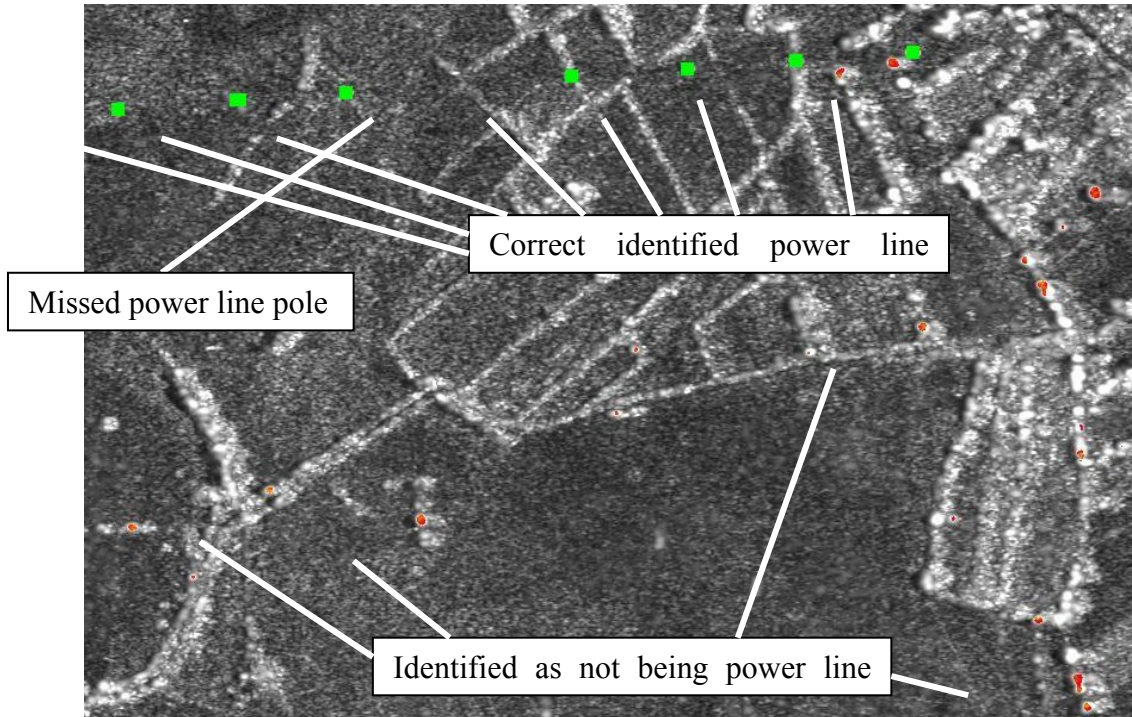
Fig.25: Result of the power line pole detection after Hough-transform (by RMA). Since power lines are build along a straight line, the Hough-transform searched for alignments of the detected poles. The results of the Hough-transform can be seen in green, the red detections are not aligned and do not belong to a power line.

5.7   Detection and Separation of Trees and Bushes/Hedges

From CROMAC we received the information that hedges which are often growing aside the agriculturally used fields, were often used as defensive lines. Soldiers were hiding behind the hedges. To defend themselves, mines were often placed some distance in front of the hedges. Therefore hedges are an indicator for mine suspected area and CROMAC is interested to get information about the distribution of hedges in the test area.

In multispectral data, hedges and trees appear very similar because only the uppermost parts of the plants which are in both cases leaves are visible. In SAR data the wavelength defines the penetration into the vegetation. While X-band SAR data (λ=3cm) is reflected mostly from the uppermost centimetres of the vegetation, L-band (λ=24cm) penetrates deeper into the vegetation structure and has a high reflectance from the volume part of the vegetation. If the wavelength is still longer (P-band, λ=67cm), the vegetation volume becomes nearly invisible for SAR and the double reflection at the ground and the trunk of trees plays an important role. Because of this behaviour trees are clearly visible in P-band because of their trunk while bushes/hedges do not reflect much energy in P-band. Therefore it is possible to separate trees and hedges using L- and P-band SAR data. The crosspolarised L-band data (Lxx) gives the maximum backscatter from the vegetation volume while copolarised P-band data (e.g. Phh) is sensible to double reflection on the horizontal ground and the vertical trunk.

For a better separation of both targets from other objects additional parameters are used: The SAR data Xvv and Pxx, the Daedalus channel 4 data, and the ratios Pxx/Xvv and Pxx/Phh.
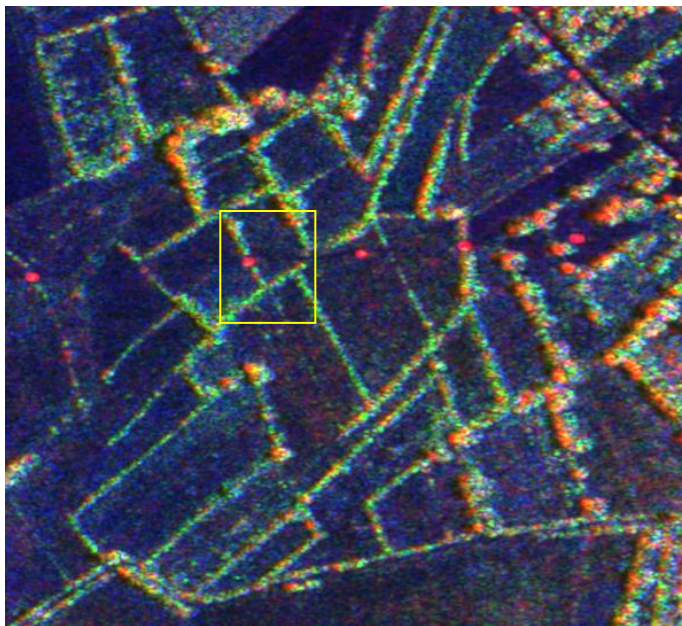
Fig 26: Colour composite of geocoded E-SAR amplitude data.
Red: P-band HH-polarised
Green: L-band XX-polarised
Blue: X-Band VV-polarised
Hedges have a high crosspolarised (XX) backscatter in L-band, trees additionally have a strong reflection in copolar (HH, VV) P-band.
$XX = (HV/2 + VH/2)$
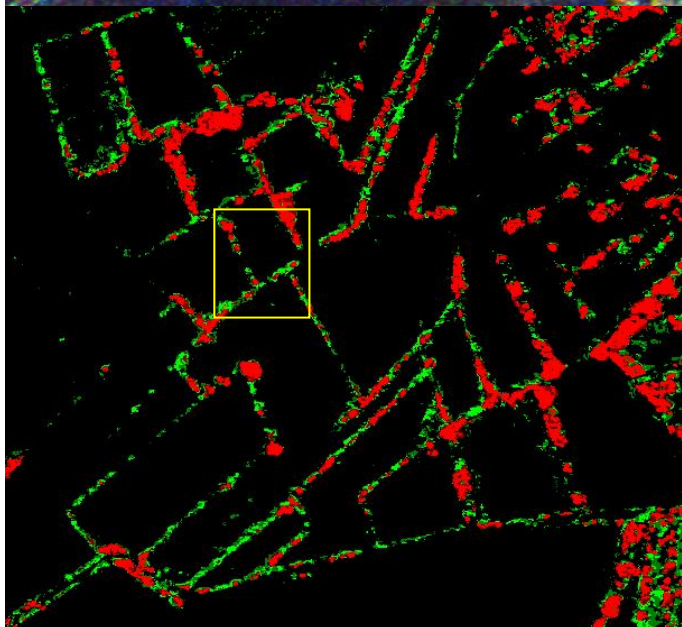
Fig 27: Colour composite of hedge and tree masks.
Objects which fulfil at least five of six criteria to be a tree are bright red, if they fulfil four criteria, they are dark red.
Objects which fulfil six of seven criteria to be a hedge and are no tree are printed in bright green. If they fulfil only five criteria, they are dark green.

Fig 28: Subset of RMK image #069 showing the area inside the yellow rectangle in fig 26 and 27.
Trees are mainly growing on the northern part of the area while in the southern part hedges, including young trees dominate.

Additionally to the separation of trees and hedges the algorithm detects and separates water areas, radar shadows and optical shadows.

The criteria for an area to be classified as water are:
- a very low backscatter in X- and L-band VV-polarised data (very smooth surface, specular reflection)
- a very low emission in the thermal IR channel 12 of Daedalus data (cold area)
- channel 04 (orange) of Daedalus data is neither very dark nor very bright
- more than 7 pixels in a 5 x 5 neighbourhood fulfil the above requirements (=> no single water pixels)
- if more than 15 pixels in a 5 x 5 neighbourhood are classified as water, the centre pixel is classified as water too.

To be classified as radar shadow, an area must:
- have a very low Xvv backscatter
- not be classified as water
- not be a hot road (no very bright areas in Daedalus thermal IR channel 12)
- contain more than 7 pixels in a 5 x 5 neighbourhood which fulfil the above requirements (=> no single radar shadow pixels)
- if more than 15 pixels in a 5 x 5 neighbourhood are classified as radar shadow, the centre pixel is classified as radar shadow too.

Pixels become members of the class "optical shadow" if:
- they are very dark in Daedalus channel 04 (orange) and 12 (thermal IR)
- they are not classified as water

- more than 7 pixels in a 5 x 5 neighbourhood fulfil the above requirements (=> no single optical shadow pixels)
- if more than 15 pixels in a 5 x 5 neighbourhood are classified as optical shadow, the centre pixel is classified as optical shadow too.

The classes "radar shadow" and "optical shadow" are not exclusive. An area can belong to both classes at the same time.

The algorithm usually uses fix boundary pixel values which have been chosen by experience. If the user wants to change these values, e.g. because in another region the situation is different, it is possible to chose others than the original values.

Fig.29: E-SAR data composite: Phh, Lxx, Xvv

Fig.30: Daed. data composite ch.12 (ThIR), 7 (NIR), 4 (R)

Fig.31: classes trees and hedges

Fig.32: Class water

Fig.33: Class radar shadow

Fig. 34: Class optical shadow
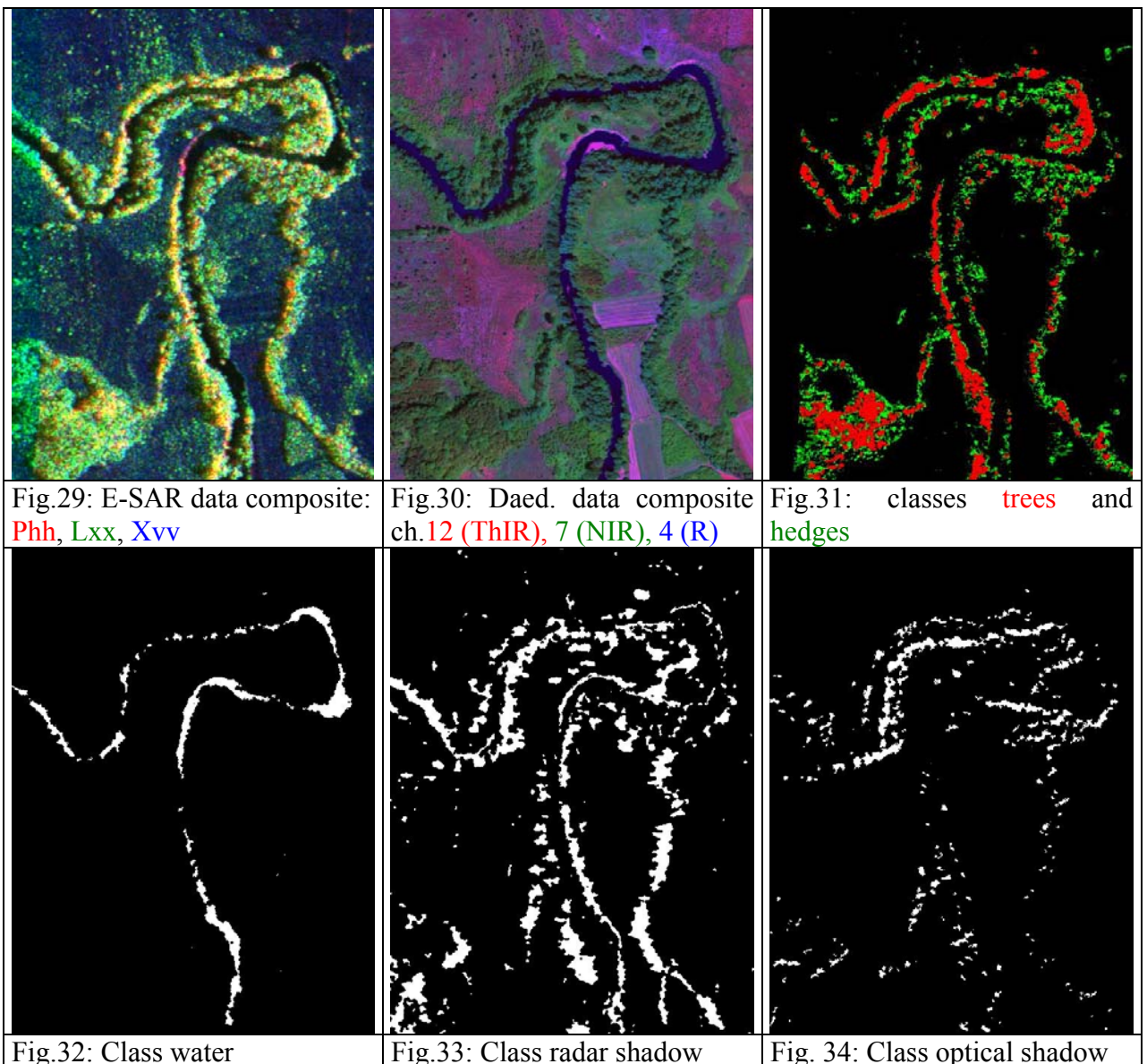
5.8 Interferometric Coherence Calculation

The basic algorithm which creates the interferometric phase and coherence from a pair of interferometric SLC data has been created already in 2002. The results in slant range geometry were geocoded and used as input to the algorithm which provides E-SAR data in Daedalus format. Now the interferometric processing algorithm has been updated for the implementation in the SMART environment. It uses as input two polarimetric SLC data sets in the format defined for SMART (3-channels: hh, xx=hv/2+vh/2, vv ; pixel interleaved complex data, little endian, separate ASCII header file).

The algorithms need as input the names of the two input files, the path to save the results and the path where it can find the geocoding matrices. This information is provided by an ASCII input text file which will be created directly by the SMART environment after reading the input from the user interface. The header files of all data sets are read and checked for consistency. Afterwards the program starts the processing of the interferometric phase and coherency in hhhh-, xxxx-, and vvvv-polarisations (hhhh means using the hh-polarisation of the master and of the slave data). The results are geocoded using the geocoding matrices. The slant range and geocoded data of phase and coherence are saved as data and as tif-images. For the resulting data separate ASCII headers containing important information are created automatically. Information about the different processing steps is saved to an output ASCII file.
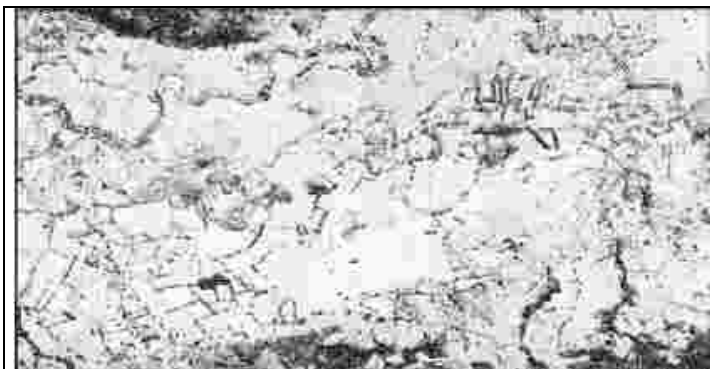
Fig. 35: Interferometric hhhh-coherence in slant range geometry (flight path below the image from left to right). White: coherence = 1, black: coherence = 0	Fig. 36: Geocoded interferometric hhhh-coherence

| Fig. 37: Geocoded interferometric hhhh-phase. Black: -π, white: π | Fig. 38: Geocoded colour composite of hhhh (red), xxxx (green), and vvvv (blue) interferometric phases | Fig. 39: Geocoded colour composite of hhhh (red), xxxx (green), and vvvv (blue) interferometric coherence |
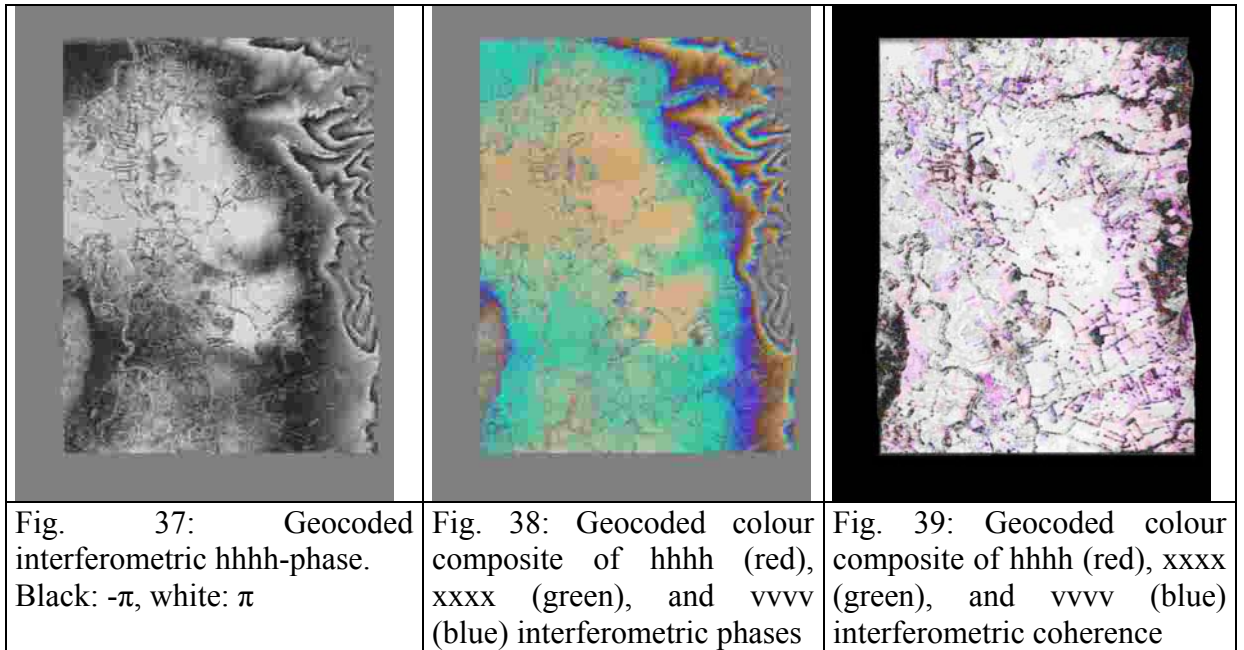
5.9 Eigenvalue Decomposition of Polarimetric SAR Data

The entropy/anisotropy/alpha decomposition method[1] was used to extract polarimetric information of SAR data. Polarimetric data of one data pixel can be decomposed into three independent scattering mechanisms because three independent observables are available. The three scattering mechanisms are described by the three eigenvalues and eigenvectors of the 3x3 coherency matrix, where the eigenvalues show the intensity and the eigenvectors the physical nature of the backscatter. In reality there might appear more than just three different scattering mechanisms. In this case, not all of them can be completely separated. The extracted scattering mechanisms will contain a mixture of the real ones but allow the maximum separability.

The entropy H reflects the dominance of one scattering mechanism over the others and therefore the degree of randomness. The extreme cases are H=0 if there is only one scattering mechanism, and H=1 if there are three extracted scattering mechanisms of the same strength. An example for the first case is a stable object with strong backscatter, e.g. a corner reflector (three reflections) or a wall (two reflections: ground and wall). Nearly all of the backscattered energy of the resolution cell will show this backscatter behaviour. It will dominate over all other scattering mechanisms like e.g. the surface backscatter from the surrounding ground. Such objects will have a very low entropy. A high entropy can be observed e.g. in forests, when due to the multiple reflections in the crown the polarisation of the backscatter gets more and more unrelated to the polarisation of the incoming wave. On smooth surfaces like roads, where most of the energy is scattered away from the sensor and noise begins to play an important role, the low measured backscatter shows a random polarimetric behaviour. In both cases, all extracted scattering mechanisms will be of similar strength, and the entropy will be high.

---

[1] S.Cloude and E.Pottier, An Entropy Based Classification Scheme for Land Applications of Polarimetric SAR, IEEE Transactions on Geoscience and Remote Sensing, Vol.35, No.1, January 1997

The anisotropy A is the normalised difference between two smaller eigenvalues. Together with the entropy, this parameter gives an overview over the importance of the different scattering mechanisms. If A is low, the second largest eigenvalue λ_2 and small eigenvalue λ_3 are of similar strength, either because there is only one important scattering mechanism (low entropy, $\lambda_1 >> \lambda_2, \lambda_3$) or because all three are of similar importance (high entropy, $\lambda_1 \approx \lambda_2 \approx \lambda_3$). If A is high ($\lambda_2 >> \lambda_3$, maximum: A=1), then there exist two important scattering mechanisms, the third one is negligible. Since A is created by the difference of the two scattering mechanisms with the lower backscatter, noise can become strong enough to disturb the information content for low anisotropies. Most structures of the amplitude image of SAR data are not visible any more in an anisotropy image because λ_1 , which contains the information of the most important scattering mechanism is not used in the calculation of the anisotropy. On the other hand, structures may appear that were invisible in other sets of data. The anisotropy should never been used without using the entropy too.

The α-angle is a measure for the scattering mechanism itself and can have values between 0° and 90°. α=0° means that there exists only an odd number of scatterings (single bounce scattering from the ground, or triple bounce scattering, e.g. from a corner reflector or from corners at houses). An increase of the α-angle is a sign for a change of the scattering properties to dipole scattering (α=45°) and finally to an even number of scatterings (double bounce, α=90°).

The information content of the results of a H/A/α decomposition is very different from regular intensity data of SAR or optical sensors. It needs more interpretation than intensity data but on the other hand contains very useful information, which is independent of the intensities. Such independent information can help in separating classes which appear very similar in optical and SAR amplitude data.

Flow chart of the algorithm:

```
┌─────────────────────────────────────┐
│ Read Polarimetric slant range SLC   │
│ data (4 complex numbers per pixel:   │
│ hh, hv, vv, vh )                     │
└─────────────────────────────────────┘
                 │
                 ▼
┌─────────────────────────────────────┐
│ Create Pauli target vector $\vec{k}_p$ │
└─────────────────────────────────────┘
                 │
                 ▼
┌─────────────────────────────────────┐
│ Create expectation value for         │
│ coherence matrix [T] by windowing    │
│ (9 complex numbers per pixel)        │
└─────────────────────────────────────┘
                 │
                 ▼
┌─────────────────────────────────────┐
│ Calculate real eigenvalues           │
│ ($\lambda_1$, $\lambda_2$, $\lambda_3$) and │
│ complex eigenvectors                 │
│ ($\hat{e}_1, \hat{e}_2, \hat{e}_3$) of the │
│ coherence matrix [T]                 │
└─────────────────────────────────────┘
                 │
                 ▼
┌─────────────────────────────────────┐
│ Create derived parameters:           │
│ Probability P (ancillary parameter)  │
│ Entropy H                            │
│ Anisotropy A                         │
│ α-angle                              │
└─────────────────────────────────────┘
                 │
                 ▼
┌─────────────────────────────────────┐
│ Geocode the derived parameters       │
└─────────────────────────────────────┘
                 │
                 ▼
┌─────────────────────────────────────┐
│ Save parameters as data and          │
│ tif-images                           │
└─────────────────────────────────────┘
```

$$\vec{k}_p = \frac{1}{\sqrt{2}} \begin{pmatrix} hh + vv \\ hh - vv \\ hv + vh \end{pmatrix}$$

$$\langle [T] \rangle = \langle \vec{k}_p \cdot \vec{k}_p^* \rangle$$

$$\langle [T] \rangle = \sum_{j=1}^{3} \lambda_j \hat{e}_j \cdot \hat{e}_j^*$$

$$\hat{e}_j = e^{i\phi_j} \begin{pmatrix} \cos\alpha_j \\ \sin\alpha_j \cos\beta_j e^{i\delta_j} \\ \sin\alpha_j \sin\beta_j e^{i\gamma_j} \end{pmatrix}$$

$$P_j = \frac{\lambda_j}{\sum_{k=1}^{3} \lambda_k}$$

$$H = \sum_{k=1}^{3} -P_j \log_3 P_j$$

$$\alpha = \sum_{k=1}^{3} P_j \alpha_j$$

$$A = \frac{\lambda_2 - \lambda_3}{\lambda_2 + \lambda_3}$$
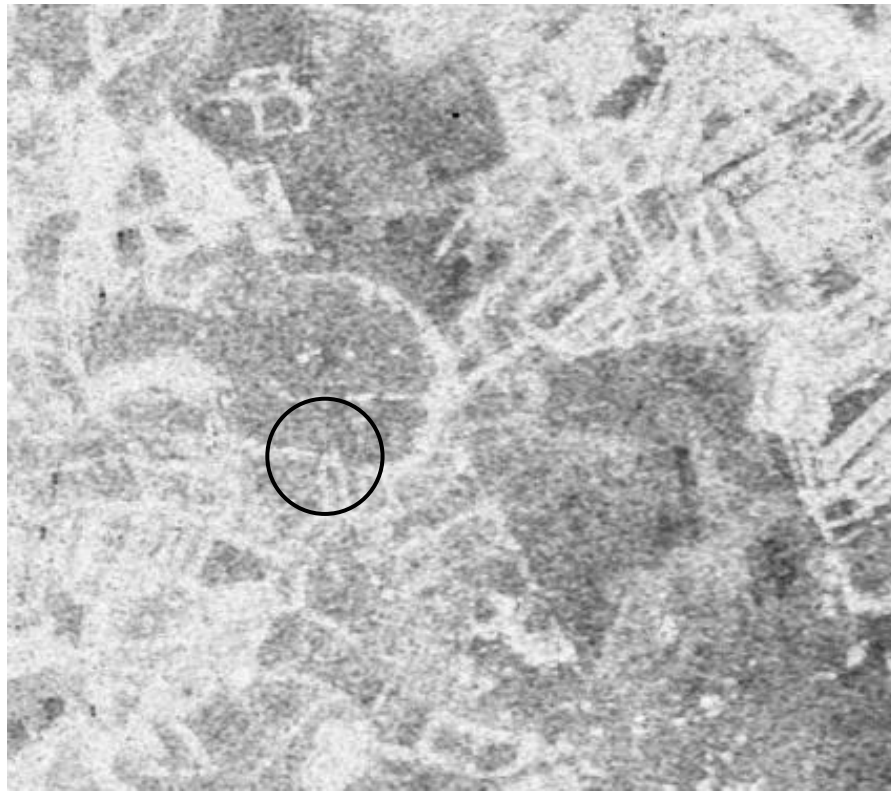
Fig.40: Entropy H of a part of the Glinska Poljana test area. Dark areas have a low entropy (one dominant scattering mechanism), bright areas a high entropy (several scattering mechanisms of similar strength). Fences inside the area marked by the circle show a similar entropy like the surrounding unused fields and are therefore not visible in the entropy image.
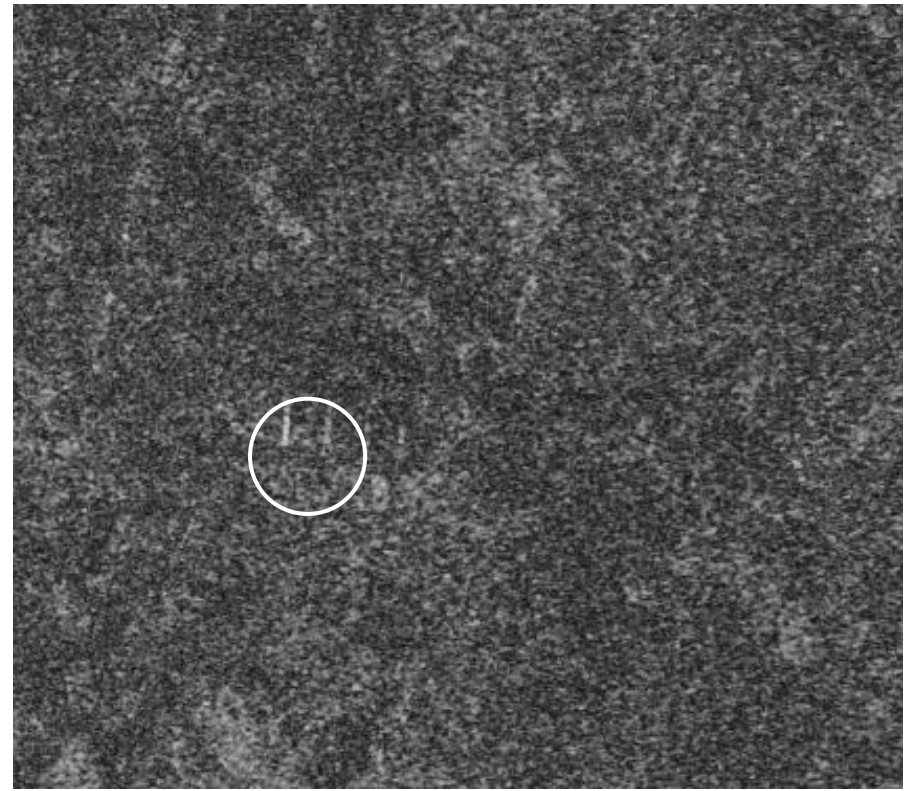
Fig.41: Anisotropy A of a part of the Glinska Poljana test area. Dark areas have a low anisotropy (2nd and 3rd eigenvalues are of similar strength), bright areas a high anisotropy (2nd eigenvalue is much stronger than 3rd). At the fences two dominating scattering mechanisms exist ($\lambda_1, \lambda_2 >> \lambda_3$), single bounce reflections from the horizontal fencing, and double bounce from fence and ground. At the unused fields, surface scattering is dominating above two different kinds of volume scattering with similar strength ($\lambda_1 > \lambda_2 \approx \lambda_3$).
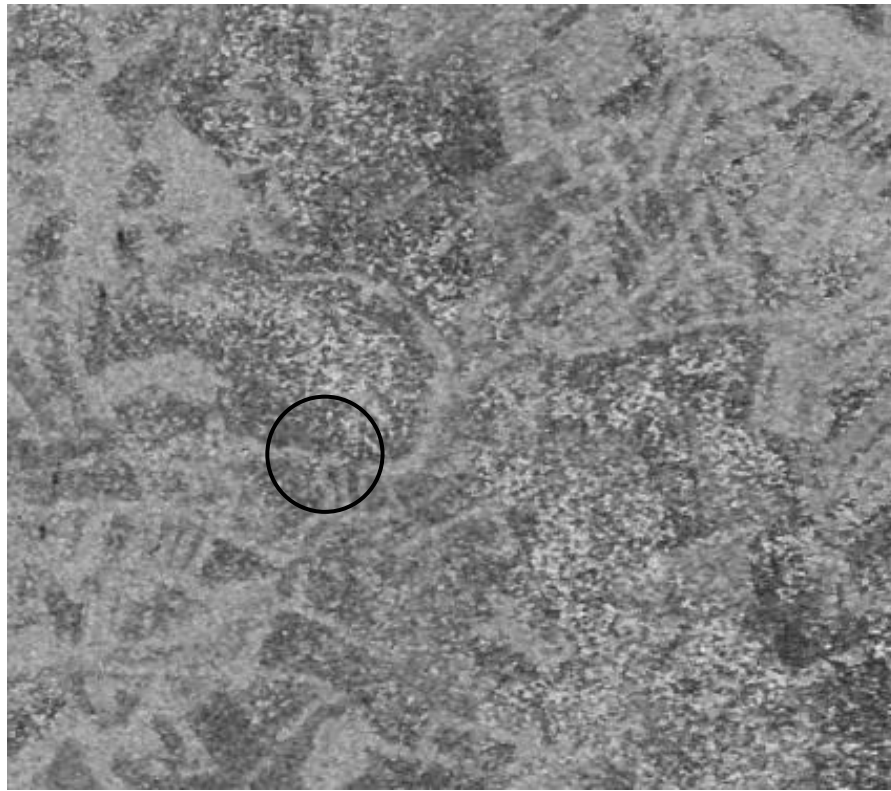
Fig.42: α-angle of a part of the Glinska Poljana test area. Dark areas have a small α (surface scattering), bright areas a large α (dihedral scattering). The vegetation in mine suspected areas appears very inhomogeneous with very dark parts (surface scattering) and very bright parts (double bounce at oriented stalks and the ground). This is no noise effect, bare agricultural fields appear homogeneous.
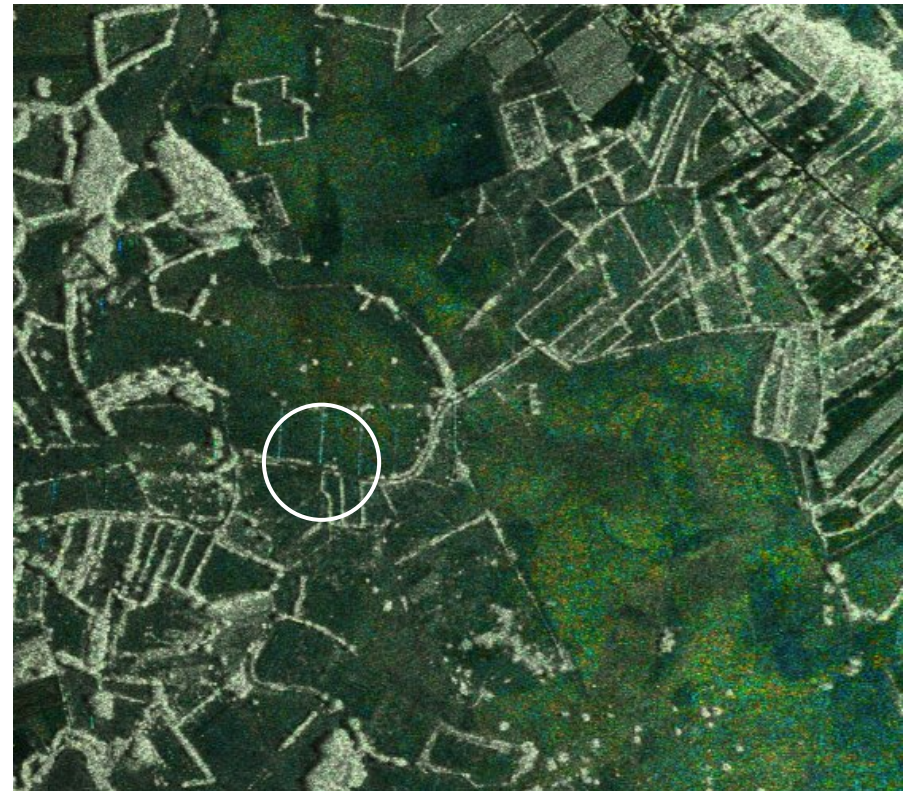
Fig.43: HSV (hue/saturation/value) colour composite of the α-angle, the inverse entropy 1-H, and the backscatter amplitudes. The hue reflects the kind of scattering, the saturation is defined by the entropy H and the image intensity by the overall backscatter amplitudes. The more dominating a scattering mechanism is, the more colour is visible. If there is no dominating type of scattering, only grey values are visible.

5.10 Unsupervised Classification of Polarimetric E-SAR Data Based on H and α

An algorithm for an unsupervised classification of polarimetric SAR data was developed, based on the eigenvector decomposition. The entropy H, the α-angle, the first two Eigenvalues λ_1 and λ_2 and the interferometric coherency are as parameters for the classification. They carry independent information from polarimetry, interferometry and backscatter strength.

Flow of the algorithm:

Read geocoded classification parameters: (H, α, γ, $\lambda1$, $\lambda2$,Eigenvalues)

$\downarrow$

Assign pixels to eight different classes depending on their position in the H-α-plane.

$\downarrow$

Compare pixels near the borders of classes with their neighbourhood and reallocate them.

$\downarrow$

Geocode the classification result.

$\downarrow$

Save the classification result as byte-data and tif-image.
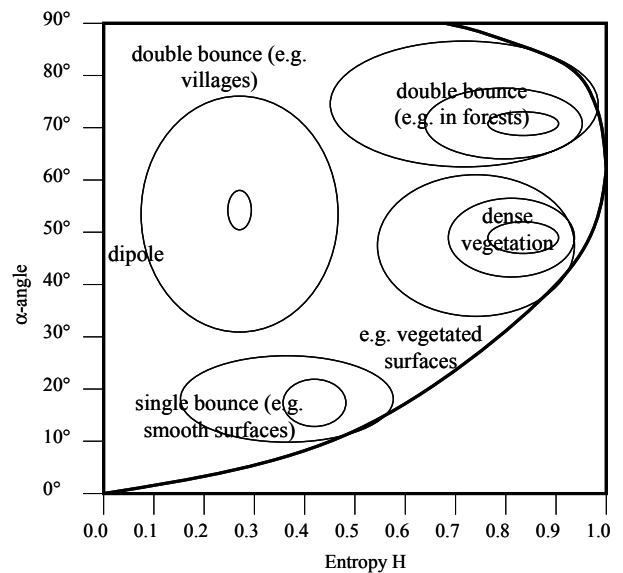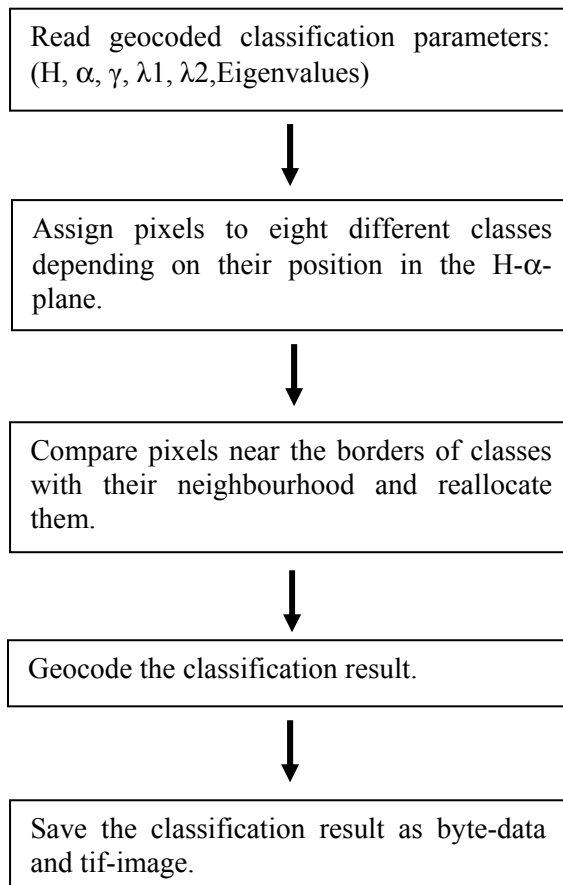
Fig. 44: H-α-diagram. Possible values are on the left side of the black curve. As an example, several classes are marked in the diagram showing imaginary areas of high pixel density in the parameter space.
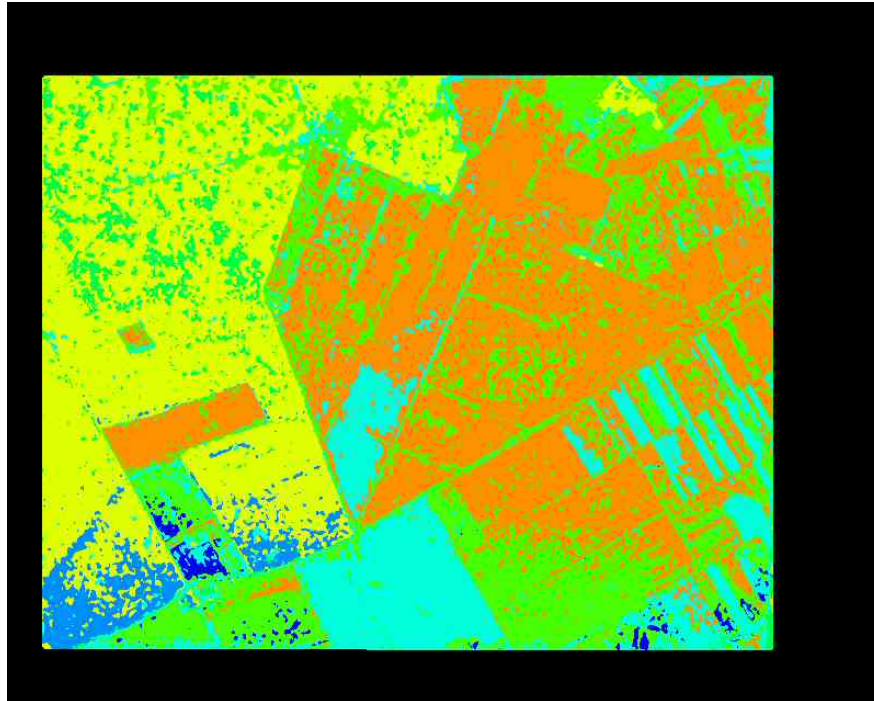
Fig.45: Unsupervised classification results of the four parameters H, α, λ₁, γ.
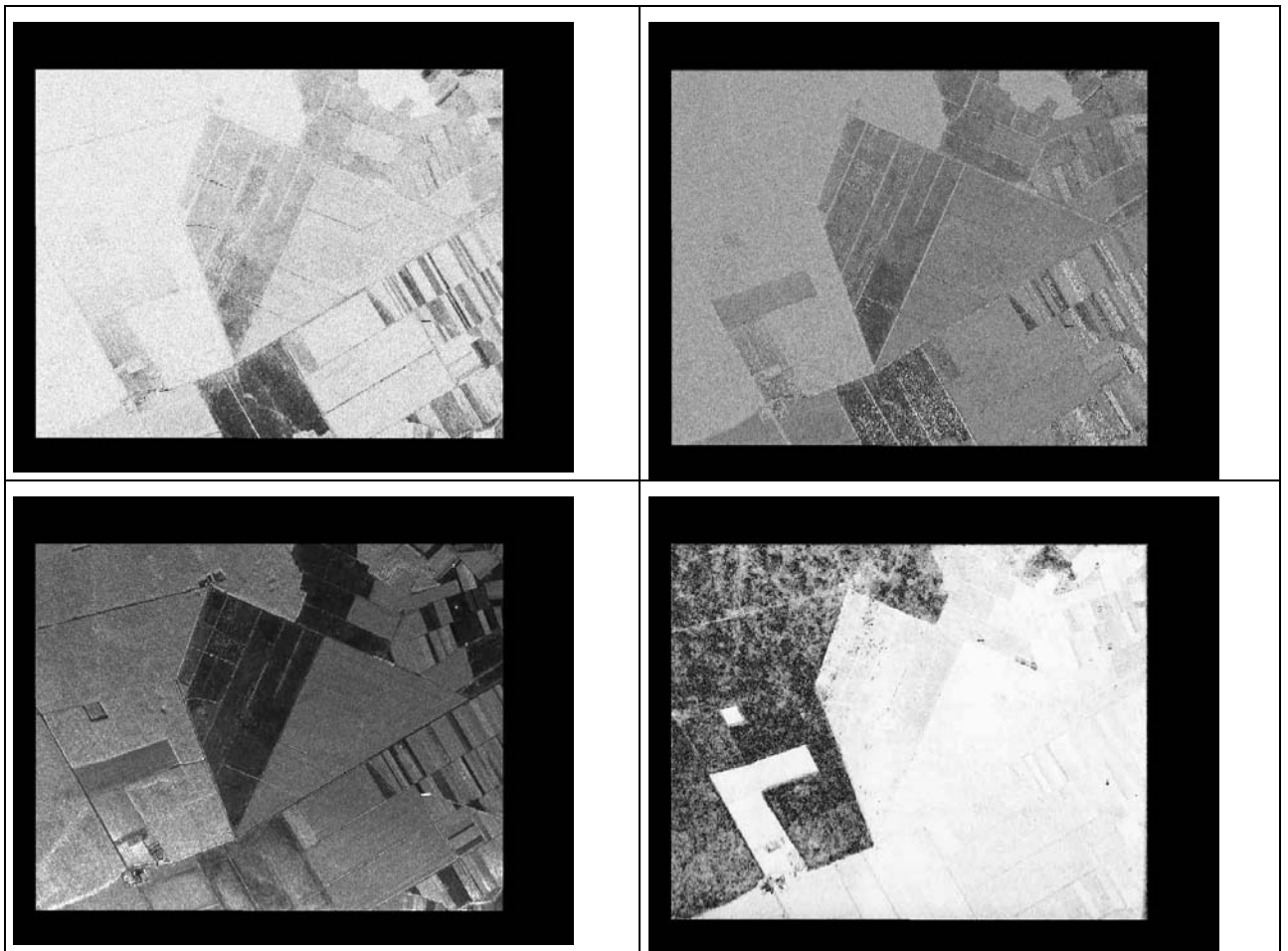
Fig.46: Input parameters for the classification: Entropy H, α-angle, Eigenvalue λ₁, coherecny γ.

Due to the speckle of SAR data, the different classes show a very large variance in the parameter values. This leads to overlapping classes which can not be separated any more completely. Therefore speckle filtered input data should be used or if they are not available, a median filtering of the input data should be done. The input data then show a much smoother appearance of homogeneous areas but on the other hand, small scatterers in the median filtered data may disappear.

The new classification algorithm reads the input data and runs a median filter with a window size set by the user (if 0 then no median filtering). The parameters are grouped into a number of partitions each. A four dimensional data set is created, containing the number of pixels inside a four-dimensional box of the length of one partition. The classification starts with the box containing the most pixels and creates the first class. The next densely populated box is chosen and a neighbourhood of 3x3x3x3 boxes is checked for already classified boxes. If there is already a box belonging to a certain class, this class grows and the centre box gets the same class (as long as the maximum number of pixels per class is not reached). If no box in the neighbourhood is already classified, a new class is created. After all boxes are classified, the number of pixels in one class is checked. Classes with less than 0,01% of all pixels are joined and form a class containing the "unusual" pixels. Mask data and images of the separate classes are produced and saved. For interpretation purposes two HSV images (Hue Saturation Value) are produced. The Saturation is always full, the Hue shows the different classes as different colours. For the Value two different choices are taken: Using the image amplitudes as Value creates an image which can easily be interpreted while setting the Value to the maximum highlights the distribution of the different classes.

The classification is run for two different parameter choices:
1.) Entropy H, alpha angle, Eigenvalue lambda1, Coherence
2.) Entropy H, Eigenvalue lambda2, Eigenvalue lambda1, Coherence

The number of partitions for the classification parameters is crucial: Three partitions allow a fast coarse classification, more than six partitions will lead to very time consuming calculations. The needed time for the calculations is approximately proportional to partitions^4.

The maximum fraction of pixels in one class is the normalised value of the number of pixels which are allowed in one class. It can be between 0 (no pixels in a class allowed -> makes no sense) and 1 (all pixels in one class allowed -> makes not much sense either)

Since it is an unsupervised classificator, it may happen that one "real" class is spread into two or more classes during the classification. These classes can be combined in a supervised way manually by the user afterwards.

5.11 Information Mining

5.11.1 Introduction

The detection of mined fields, compared with other scene classification tasks, has very high complexity. The difficulties are in the heterogeneous nature of the observed scene, thus requiring both sensor, optical and radar, and information fusion. The sensor fusion aims at the

observation of physical and geometrical scene characteristics, trying to capture complementarities. The information fusion has as its goals first a fission of the observed signals in a quasi-complete set of primitive attributes, and their aggregation (fusion) such to be able to detect all, or at least, all possible, scene structures. The fission is based on utilisation of a library of models for the data, capturing the main attributes: radiometric or polarimetric, structural and multiscale.

The large number of models, and the huge dimensionality of the feature space, mainly for hyperspectral data, makes the selection of the appropriated data sets difficult. The task can be solved by the utilization of the categories of information communicable to users in other domains as mitigation (de-mining) and military (mining) domain knowledge. The idea is to detect areas suspected to contain mined fields by the interrelations among objects and structures defined by the experts.

In figure 47 the different concepts and objects depending on the domain knowledge ontology is shown.
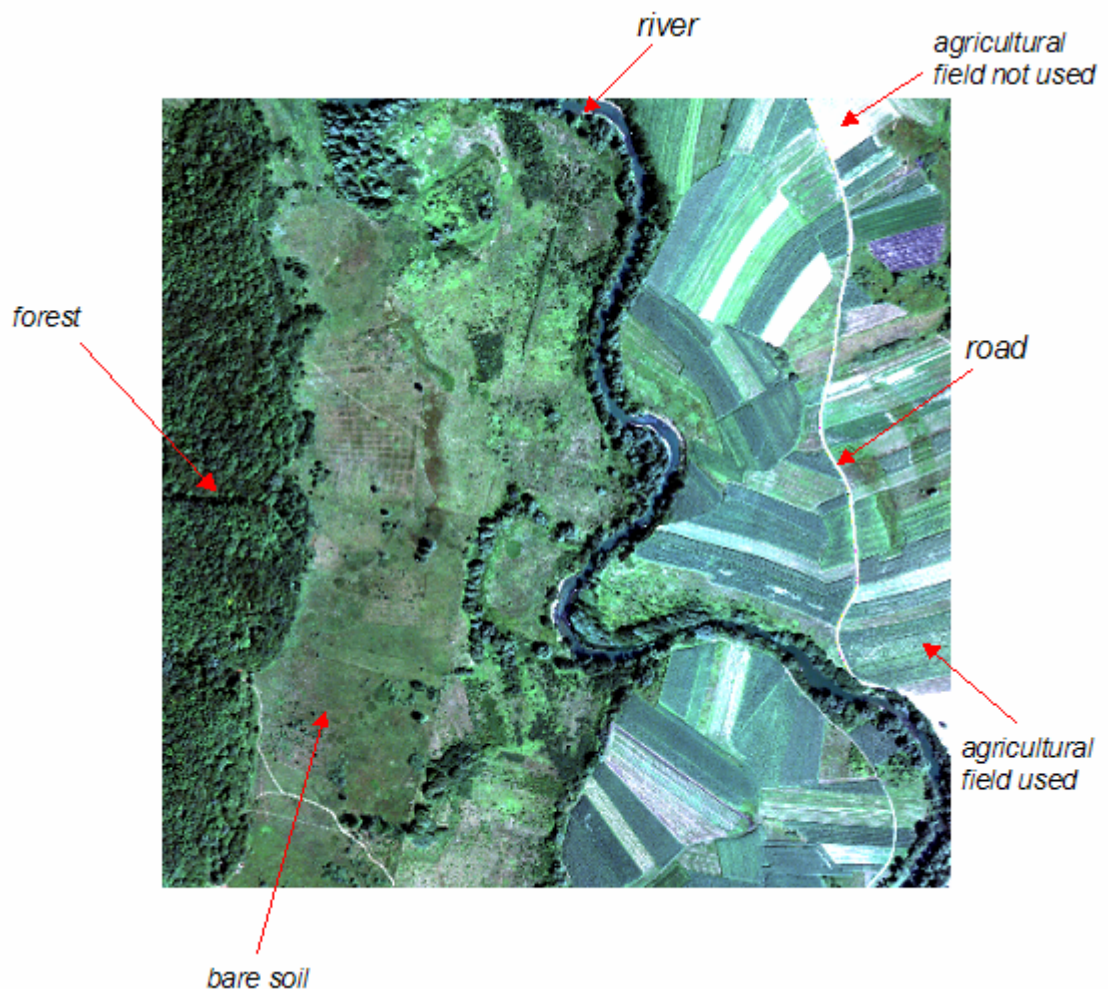
Figure 47: Daedalus data at the flight campaign in Glinska Poljana showing the mitigation domain knowledge.

The article is organized in four sections. Firstly, the aim of the project, the complementarity of the task and importance and the ensor and data used is described.

The next section presents the Knowledge-driven Information Mining System (KIM). The knowledge consists in the ensemble of existing information, know causalities and other type of associations between information and concepts. In the system, the user-defined semantic image content interpretation is linked with Bayesian networks to the completely unsupervised models. The meaning of image objects or structures is obtained by an interactive learning process fusing the relevant information extracted from the sensor image data set. A right combination of models and a good interaction by the user with the system goes to a clear detection of the targets.

Next some case studies of the system and their evaluation will be described and finally, the conclusions will be enumerated.

5.11.2 Remote sensing images analysis for mined fields detection

5.11.2.1 Goal: detection of mined fields

The goal of the project is the detection of mined fields by fusion of sensor information. Images can not only contain the quantitative and objective information obtained by unsupervised algorithms, but also subjective based on knowledge. By getting categories of knowledge defined by the experts, the user would find some classification of forest, agricultural fields, river, etc and thus, the detection of mined fields would be reduced to the exclusion of this classes over the scene.

Knowledge-driven Information Mining system (KIM) is built in order to formalize the knowledge acquisition and the knowledge driven interpretation. It provides solutions how to access to large image data sets through information mining, and content based image retrieval.

The creation of the archive catalogues or scene understanding paradigms are based on the primitive feature extraction. It must be considered as relevant external knowledge coming from expert users in order to identify and classify the mined fields.

5.11.2.2 The Sensors and Data

The first activity carried in the project has been the data collection, planning and performing flies over several suspected areas.

For each test area data were collected in X-, C-, L-, and P-band. X- and C-band were recorded in vv-polarisation (vertical received, vertical transmitted), L- and P-band were both recorded several times from slightly different tracks. The baselines which are available are 13m and 20m for L-band, 40m and 60m for P-band. All data are of good quality. In the data of X-, C-, and L-band, no visible interferences can be found, the data quality is high. In P-band there are sometimes visible interferences, but the overall quality of it is also good. Due to the experimental status of P-band an absolute calibration of the P-band data is not yet possible.

The Daedalus optical scanner data was taken from very low altitude (330m) to get a high spatial resolution. Data was collected in twelve spectral channels, ranging from visible blue to thermal infrared in good quality. Therefore several stripes of data were collected in each area and mosaicked to one geocoded image afterwards. The processing chain for Daedalus data processing consists of:

- system corrections: correction for interrupted scanlines and correction of perspective dependent sensor sensitivity.
- radiometric processing: calibration of the raw data and radiometric normalisation.
- geometric processing: preparation of aircraft position and flight attitude, geocoding of the image stripes and mosaicking the stripes into one image.

Each Daedalus channel is able to receive electromagnetic waves in a part of the whole spectrum. Since the sensitivity is not equal for all wavelengths inside this window, this is an important fact to know. In figure 48 is shown the wavelength of each band.

Channel Number	Wavelength
1	0.420 – 0.450
2	0.450 – 0.520
3	0.520 – 0.600
4	0.605 – 0.625
5	0.630 – 0.690
6	0.695 – 0.750
7	0.760 – 0.900
8	0.910 – 1.050
9	1.550 – 1.750
10	2.080 – 2.350
11	8.500 – 13.000

Figure 48: Spectral channels of ATM}

Figures 49 and 50 show a test area E-SAR data and Daedalus data, respectively.

Figure 49: Site suspected to contain mined areas at the flight campaign in Glinska Poljana. SAR L band polarimetric image.
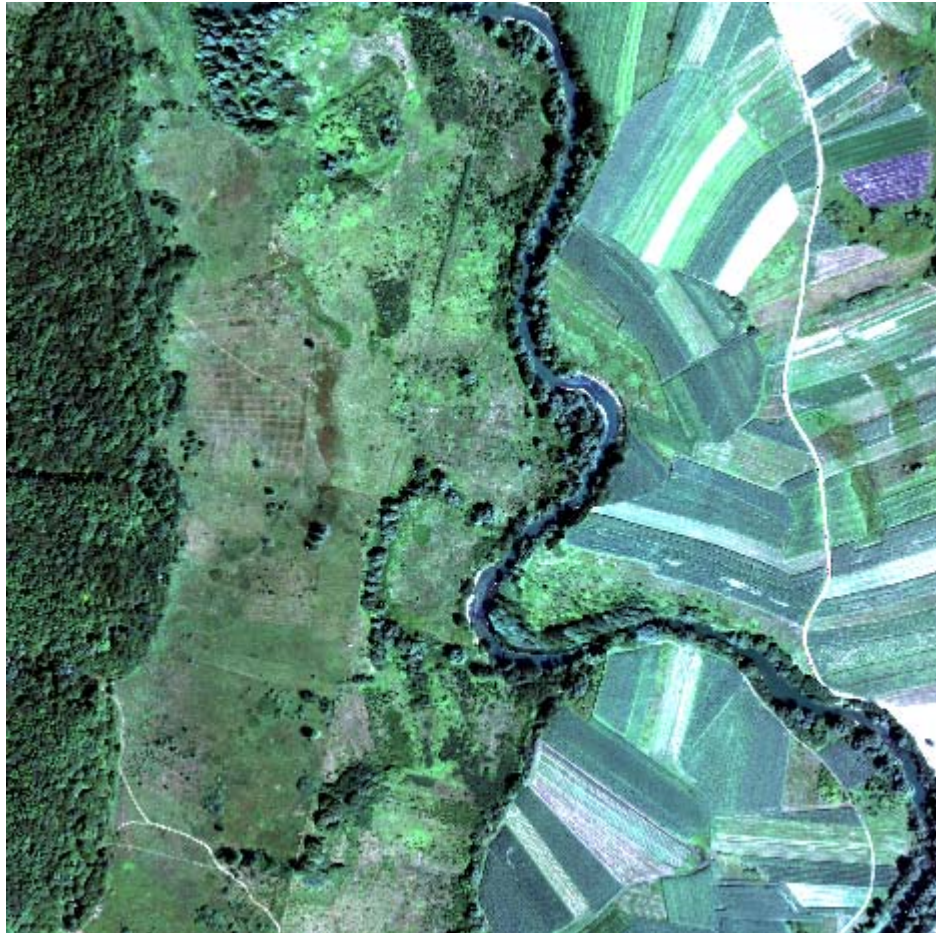
Figure 50: Daedalus data at the flight campaign in Glinska Poljana.

5.11.2.3 Data complementarity

The data comes from different sensors, optical and radar. The optical sensor provides twelve channels containing information about the scene geometry, like shape, shadows, textures, color or temperature.

On the other side, the radar sensor gives several polarisations, and, in this case, scattering information about the physical quantities, like gas concentrations, humidity, and speed of the wind is obtained.

The sensor fusion aims at the observation of physical and geometrical scene characteristics, trying to capture complementaries. Therefore, using both SAR and multispectral scanner data increases considerably the ability to separate different kinds of objects.

5.11.2.4 Knowledge based understanding

The enormous volumes of acquired data from the sensor and the need of retrieving information from them guides us to the creation of automated tools, which could explore and

explain the contents of large amount of complexity images. This environment should let the user formulate information retrieval without knowing the exact representation of the signal. The user could interpret the image using his background knowledge and by relating concepts with the image.

To perform the system stochastic models, artificial intelligence and formal and semantic representation of images should be applied.

5.11.2.5   Definition of relevant targets

Once the need of a knowledge based system is demonstrated, the next step is to define the information that must be found. The project focuses its attention in the following topics.

1. Mined Areas: Millions of mines are infesting over seventy countries on all continents. They have enormous and long-term extremely negative effects on a country and the goal is to detect them using airborne images to reduce the suspected mined areas.

2. Landing fields: In this case it is about searching for areas where would be possible to land with a small airplane from the collection of optical images. The system needs the help of the user in order to give the description of the area: flat, smooth, solid and large.

3. Dynamics of inhabited areas: For the study of the dynamics of inhabited areas, the knowledge of build-up areas must be present. Through an interactive learning the system will be able to place the populated areas.

5.11.2.6   Use of domain ontology for understanding

The large number of models, and the huge dimensionality of the feature space, mainly for hyperspectral data, makes the selection, by classical methods, of the appropriated data sets difficult. Images contain quantitative and objective information, but the new technology requires a different attitude of the user of remote sensing data for searching or interpreting the image content. The user understands the image information as semantic concepts in a certain context depending on its background. Thus, the image interpretation needs to be adapted to the user domain. The task can be solved by utilisation of the categories of information stored in the information mining system (the horizontal ontology). The expert user - sensor domain - gets help to collect the information under generic categories, at semantic level, thus communicable to users in other domains.

The research is based on the ontology of the sensor data and signal classes. In this assumption the domain knowledge can be structured as [1]:

Mitigation domain knowledge: de-mining

The expert in the de-mining action is using a special set of objects, structures and interrelations among them, to express a degree of believe in the fact that a field is mined or

not. The key step is the identification of the domain knowledge ontology. In this case the following concepts or classes are relevant:

- forest
- agriculture fields used
- agriculture fields not used
- bare soil

Military domain knowledge: mining

To increase the degree of goodness of classification of mined fields, mining domain knowledge should be used. The user will look for the following objects:

- road
- access to narrow river site
- bridge
- power line

5.11.3 Knowledge driven automated interpretation

In general, by image we understand picture thus relating it to the (human) visual perception and understanding. A picture is characterized by its primitive features such as colour, texture, and shape at different scales. However, images can not only contain this quantitative and objective information, but also subjective based on knowledge. The knowledge consists in the ensemble of existing information, know causalities and other type of associations between information and concepts.

Knowledge-driven Information Mining System (KIM) [2][3][4][5] is built in order to formalize the knowledge acquisition and the knowledge driven interpretation. The *KIM* concept and system provide solutions how to access to large image data sets through information mining, and content based image retrieval. In the system, the user-defined semantic image content interpretation is linked with Bayesian networks to a completely unsupervised content-index. Based on this stochastic link, the user can query the archive for relevant images and obtains a probabilistic classification of the entire image archive as an intuitive information representation.

5.11.3.1 The KIM System architecture

The Knowledge-based Information Mining system is implemented in two levels: acquisition, preprocessing and archiving of the data and interactive learning by the user. The former and off-line level the features are extracted from the original image for different scales. The next step is to cluster the image parameters and finally a signal content index is created using the cluster and image description and the type of stochastic model assumed.

In the interactive learning level the user is able to generate a supervised classification taking into account the clusters, scales and model types. The user can also summarize its acquired knowledge defining a label and retrieve from the archive images with the same content.

In figure 51 an scheme of the Kim architecture is displayed.
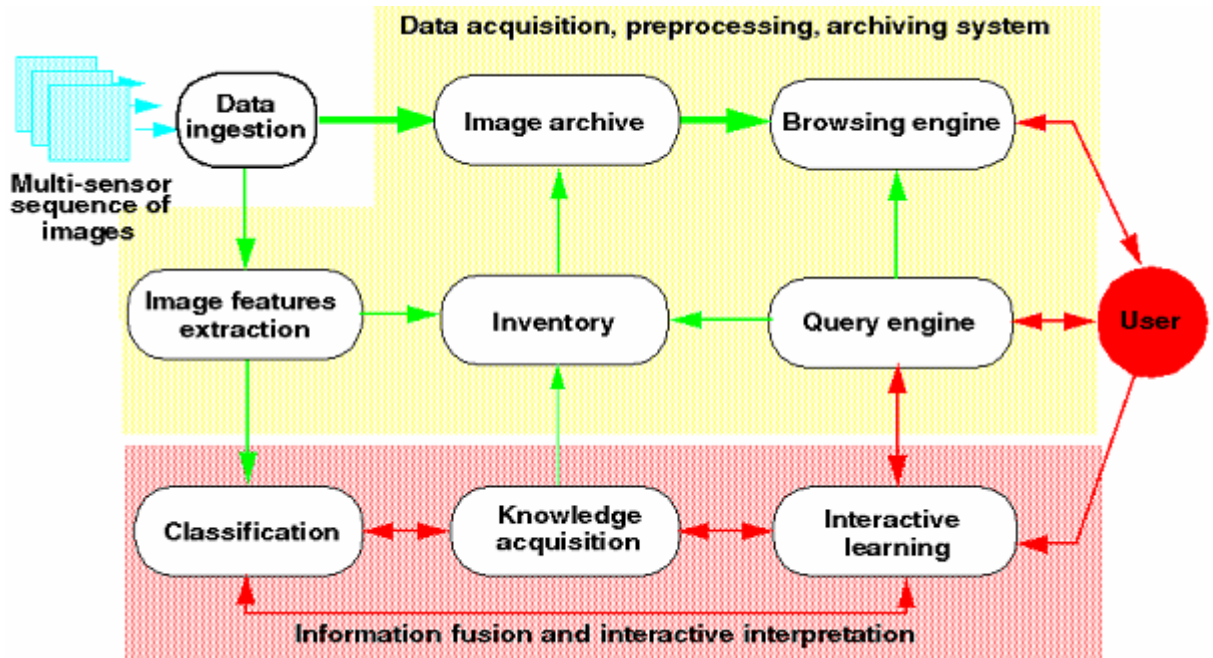
Figure 51: The system consists of two main modules: 1) the first, data driven, is responsible for data acquisition, and preprocessing for feature extraction, 2) the second, user driven, solves the information fusion and interactive interpretation operations and it supports knowledge based functions.

The hierarchy of information representation of the KIM System (see fig. 52) can be summarized in the following way:

data - features - metafeatures - cluster (class) models -semantics
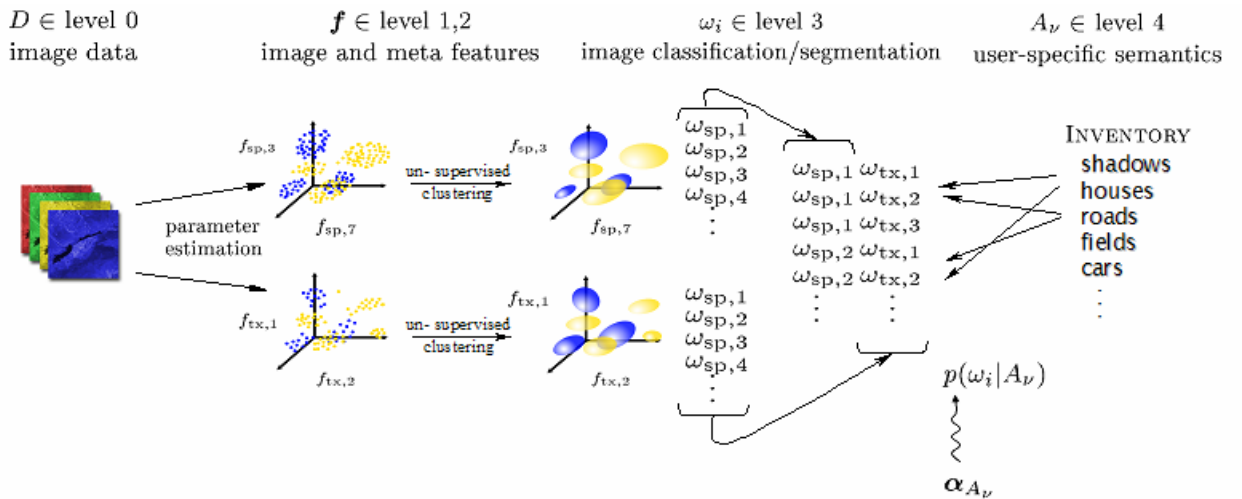
Figure 52: Representation of the KIM System

The concept of information representation is based on a 5 level Bayesian learning model:

- *Level 0*: Representation of the image data D. In our research it consists on optical hyperspectral data formed with 12 bands.
- *Level 1*: Primitive image features θ extracted from image data D (level 0) through application of stochastic models (*sp*, *tx*).
- *Level 2*: Meta-features extracted from image data D (level 0) using different signal models (*sp*, *tx*), i.e. the type of model used for the extraction of the primitive features, and the scale at which the analysis was done.
- *Level 3*: Completely unsupervised clustering of the pre-extracted image parameters θ, we obtain a vocabulary of signal classes ω_i that describe characteristic groups of points separately for each model (*sp*, *tx*). For each image, this results in as many classification maps as models are used, and they are stored in a relational database system. The used classification algorithm is called *k-means*.
- *Level 4*: User-specific interests, that is, semantic cover-type labels A, are linked to combinations of these vocabularies ω_i by probabilities $p(\omega_i \mid A_i)$ (Bayesian networks).

Levels 1 to 3 are obtained in a completely unsupervised and application-free way during data ingestion in the system. The information at level 4 can be interactively defined by users with a learning paradigm that links (objective) signal classes and user (subjective) labels A.

5.11.3.2   KIM primitives

The image information processing, archiving and retrieval needs an advanced communication technology.

The kernel of the system is a database that contains information about the images, stochastic models, sensors used, features extracted, quicklooks of the images, classification maps, defined labels and users.

The system architecture is based on a client-server structure and is designed to support web-based remote access which enables the communication. Thus, the offline tasks are curried out on the server and the interactive learning mainly on the client.

5.11.3.3   Bayesian Fusion and Classification

The information fusion aims a fission of the signals in primitive features and their aggregation to be able to detect all possible scene structures.

The different extracted features are combined for a later classification of objects or concepts. The clustering is applied for each feature space apart for all images in an archive, thus is simultaneously a data reduction and generalization by similarity over the image space. The different clusters will be included in a database catalogue.

At the semantic level the meaning of image objects or structures is obtained by an interactive learning process fusing the relevant information extracted from one sensor image data set or multisensor data and information.

5.11.3.4   Web KIM Application

In figure 53, the interface of Kim System is shown.
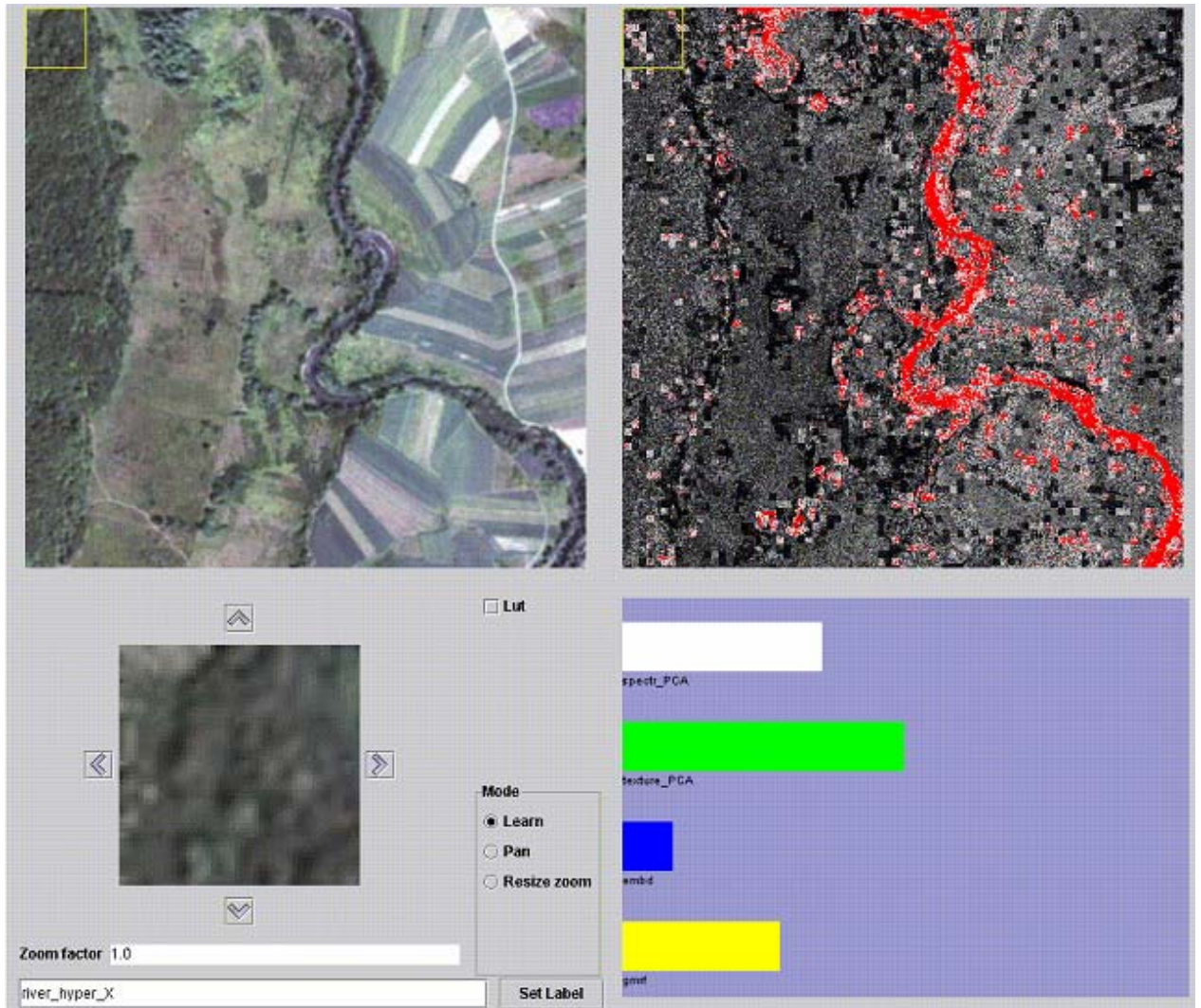
Figure 53: Kim System

On the left part of the application you can visualize the image that you have selected, in this case it is a subset of the *smart* data. On the left bottom part, appears a zoomed part of the original picture. On the right part, we visualize a map which contains the combination of the classfiles obtained in the clustering phase of the kim chain for the selected models. In red appears the positive examples and in grey dark the negative ones. It is clearly separated the target and false alarms from the rest of objects. At the bottom, there are four bars, each one corresponds to one selected model and show how the system is learning, the longer one, the more the system learns with that model.

Sensor data and features selection

In sections 5.11.4.1 and 5.11.4.2 the extracted radar and optical features will be presented. The user must select two or four features among principal component analysis of high resolution hyperspectral images, principal component analysis of the texture parameters, polarimetric L Band SAR images and polarimetric X Band SAR images.

Knowledge representation

Ones the user has trained the system for finding the targets, a label can be defined. A label is the acquired knowledge which will be included in a database catalogue. This knowledge can be used by the user in later iterations to improve the results.

Operation protocol

The actions performed by the user on the system are stored in the database. This actions can be "choose a model", "select an image", "give a positive or negative example on an image", "load the applet", "zoom an image", "search images from the catalogue", etc.

5.11.4 Case study

Once the Kim System has been presented and the objective is defined the case study raises. Different features, both optical and radar, will be extracted for the generation of risk map expected to contain mined fields. Finally, the combination of features will be evaluated.

5.11.4.1 Feature extraction for radar data

In this section, the second step of the KIM chain is focused: *feature extraction*. In this phase, different unsupervised techniques are applied: SAR despeckled images, SAR image textures at resolutions 2 meters and 4 meters, SAR polarimetric signatures. The generic features that have been extracted are:

- L-Band:
    - HH (scale 1, 2)
    - VV (scale 1, 2)
    - HV (scale 1, 2)
    - VH (scale 1, 2)
    - Alpha angle
    - Anisotropy A
    - Entropy H
- P-Band:
    - Alpha angle
    - Anisotropy A
    - Entropy H
- X-Band:
    - VV (scale 1, 2)

5.11.4.2 Feature extraction for optical data

In section 5.11.4.1 the features for radar data are listed. In parallel, optical features as hyperspectral signatures, texture parameters (channel 8) at different resolutions or principal component analysis are extracted. In the following these methods are briefly presented.

Texture Parameters

This section pretends to explain how to extract information from the observed data as contextual spatial features for false alarms rejection. To extract structural information from remote sensing images, stochastic models are applied, for instance, the *Gibbs-Markov Random Field (GMRF)*. This algorithm assumes that the statistics of the grey level of the pixels belonging to a neighborhood with a restricted dimension.

From the estimated parameters, it is derived several features to describe the image content: the norm of the estimated parameters $\left|\hat{\theta}\right|$ as the strength of the texture, the estimate of the variance $\hat{\sigma}_M^2$, the evidence of the model M and the local mean, e.g. the twelve spectral channels in the visible spectrum of sensor result in a twelve-dimensional vector $\theta = \theta_1, \theta_1, ..., \theta_{12}$.

Spectral Signatures

To describe the image content by using the spectral properties, directly assign the individual spectral channels to elements of the vector ξ, e.g. the twelve spectral channels in the visible spectrum of the sensor result in a twelve-dimensional vector $\xi = \xi_1, \xi_1, ..., \xi_{12}$.

Principal Component Analysis

Principal Components Analysis technique produces uncorrelated output bands, segregates noise components, and reduces the dimensionality of data sets. Because multispectral data bands are often highly correlated, the Principal Component (PC) Transformation is used to produce uncorrelated output bands. This is done by finding a new set of orthogonal axes that have their origin at the data mean and that are rotated so the data variance is maximized. PC bands are linear combinations of the original spectral bands and are uncorrelated. The first PC band contains the largest percentage of data variance and the second PC band contains the second largest data variance. The third one appears noisy because it contains very little variance, much of which is due to noise in the original spectral data. Principal Component bands produce more contrast composite images than spectral composite images because the data is uncorrelated.

5.11.4.3   Generation of risk maps

The different models ingested in the system that can be selected for the interactive learning are: *SAR embd, L band hh (scale 1, scale 2), SAR embd L band vv (scale 1, scale 2), SAR embd L band hv (scale 1, scale 2), SAR embd L band vh (scale 1, scale 2), SAR embd X band vv (scale 1), SAR gmrf L band hh (scale 1, scale 2), SAR gmrf L band vv (scale 1, scale 2), SAR gmrf L band hv (scale 1, scale 2), SAR gmrf L band vh (scale 1, scale 2), SAR gmrf X band vv (scale 1), spectral signature L band alpha, spectral signature, L band anisotropy, spectral signature L band entropy, spectral signature P band alpha, spectral signature P band anisotropy, spectral signature P band entropy, principal component analysis of the spectral*

signature, principal component analysis of the texture parameter from optical data, texture parameter from daedalus sensor (scale 0, scale1, scale 2)

The following images presents a selection of examples extracted from an interactive session aiming at detection of forest (figs. 54 and 55), agriculture fields used (figs. 56 and 57), agriculture fields not used (figs. 58 and 59), bare soil (figs. 60 and 61), road (figs. 62 and 63) or river (figs. 64 and 65).
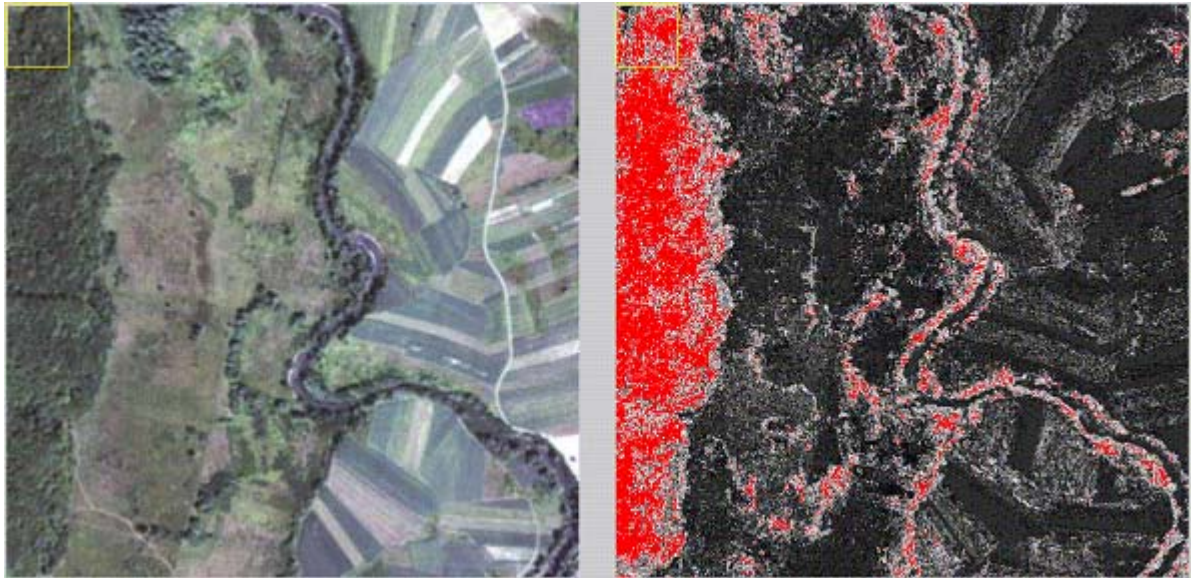
Figure 54: Site suspected to contain forest. Combination of models used in the interactive learning *PCA of hyperspectral images, PCA of texture parameters, SAR L Band polarimetric image*
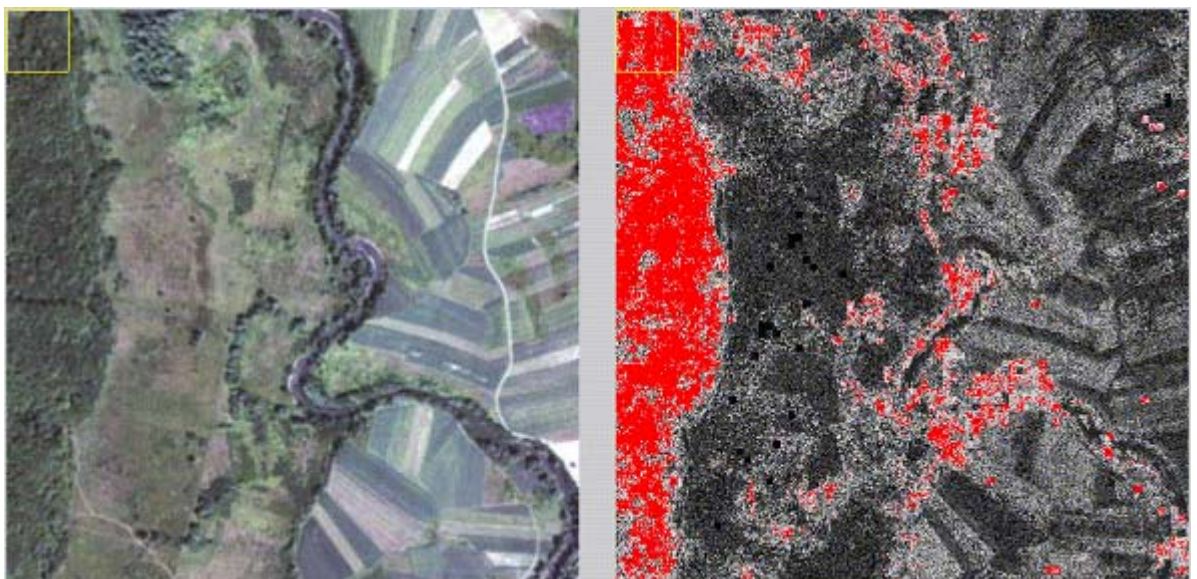
Figure 55: Site suspected to contain forest. Combination of models used in the interactive learning *PCA of hyperspectral images, PCA of texture parameters, SAR X Band polarimetric image*
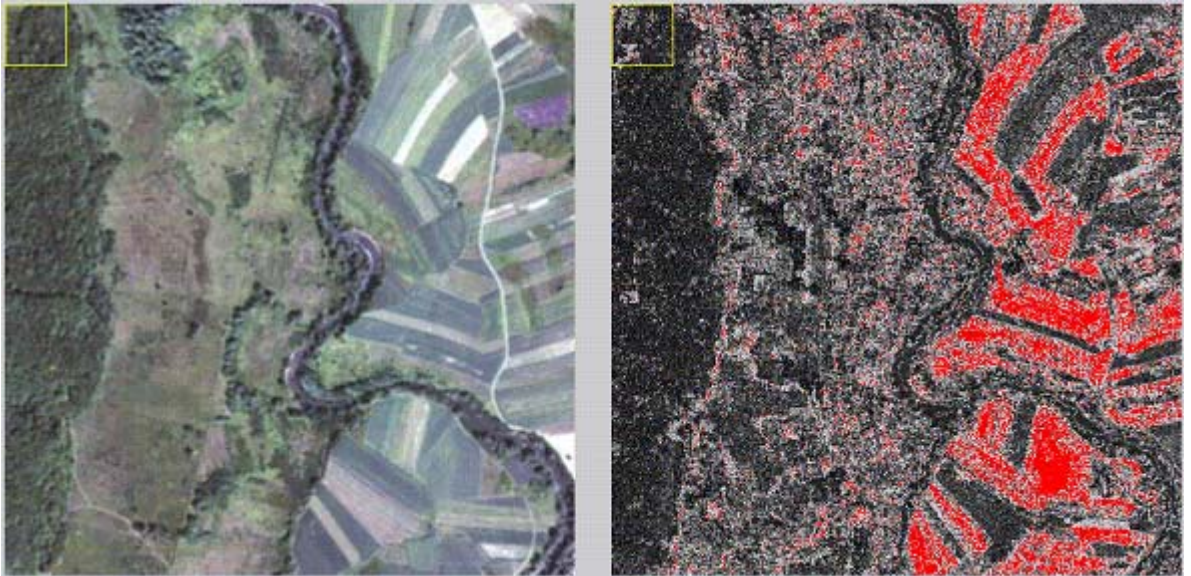
Figure 56: Site suspected to contain agriculture fields used. Combination of models used in the interactive learning *PCA of hyperspectral images, PCA of texture parameters, SAR L Band polarimetric image*
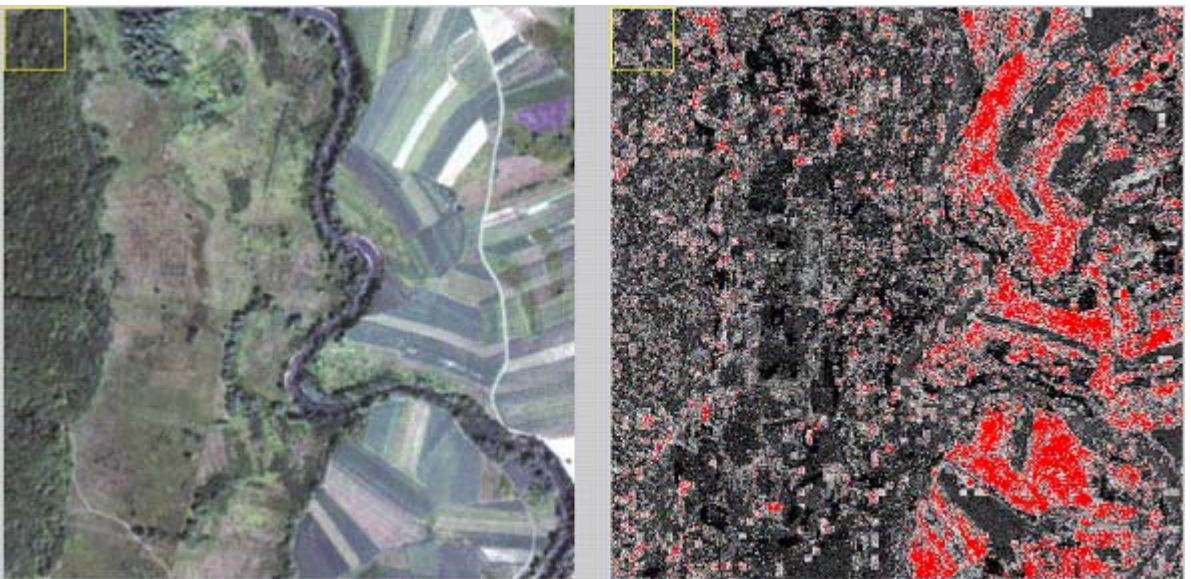
Figure 57: Site suspected to contain agriculture fields used. Combination of models used in the interactive learning *PCA of hyperspectral images, PCA of texture parameters, SAR X Band polarimetric image*
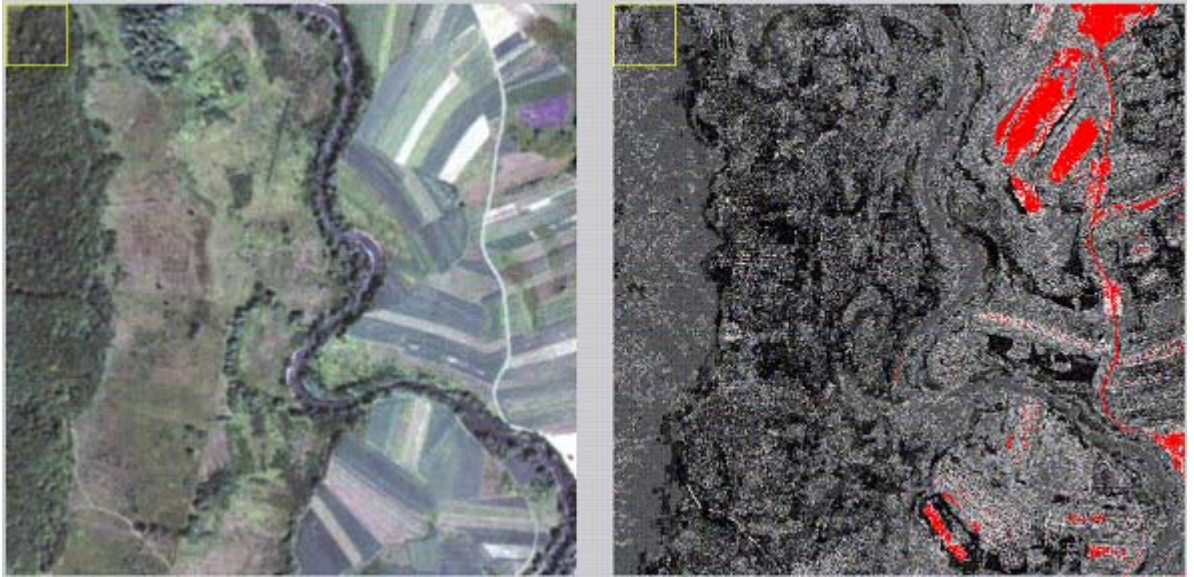
Figure 58: Site suspected to contain agriculture fields not used. Combination of models used in the interactive learning *PCA of hyperspectral images, PCA of texture parameters, SAR L Band polarimetric image*
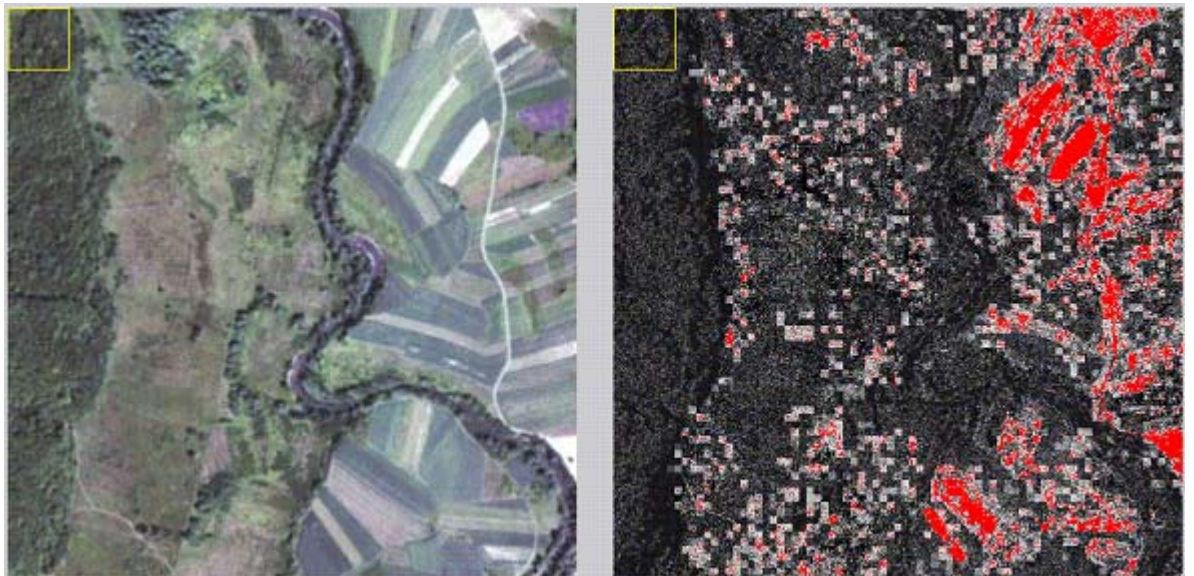
Figure 59: Site suspected to contain agriculture fields not used. Combination of models used in the interactive learning *PCA of hyperspectral images, PCA of texture parameters, SAR X Band polarimetric image*
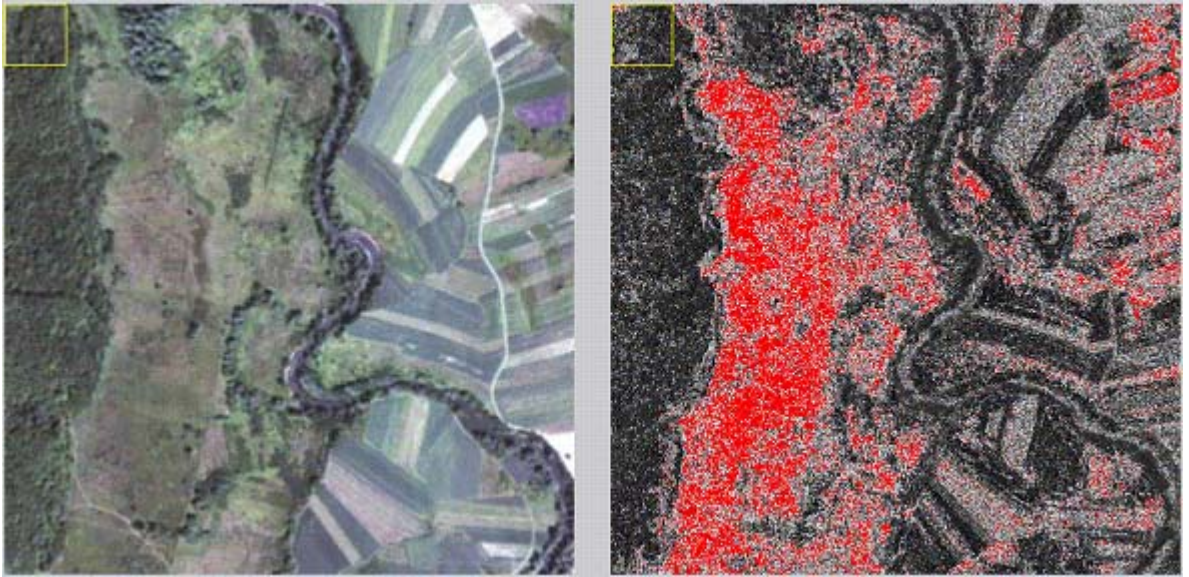
Figure 60: Site suspected to contain bare soil. Combination of models used in the interactive learning *PCA of hyperspectral images, PCA of texture parameters, SAR L Band polarimetric image*
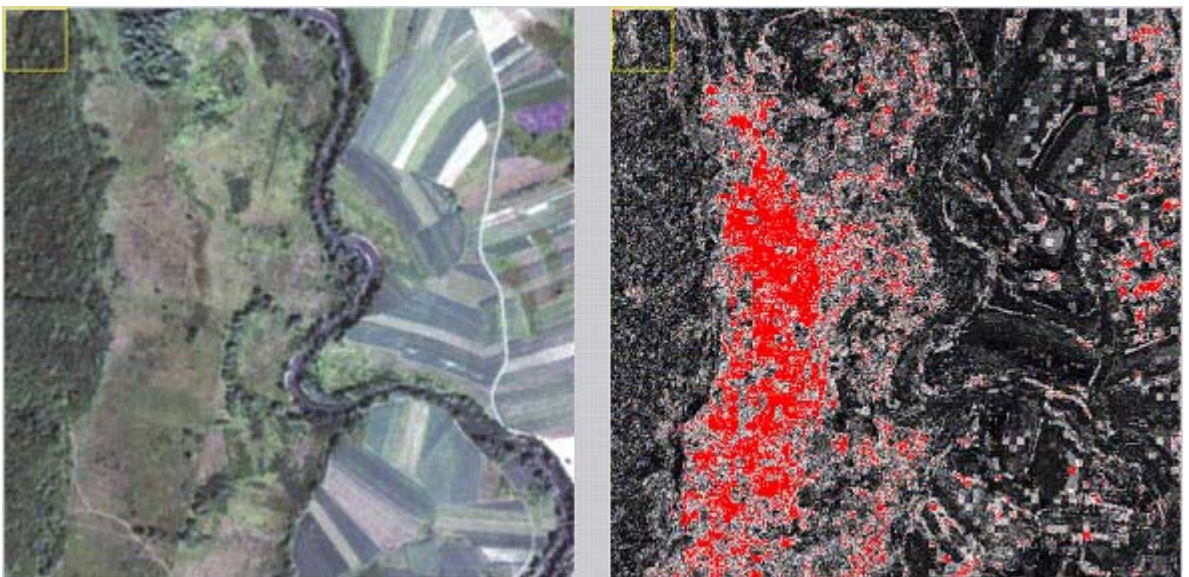
Figure 61: Site suspected to contain bare soil. Combination of models used in the interactive learning *PCA of hyperspectral images, PCA of texture parameters, SAR X Band polarimetric image*
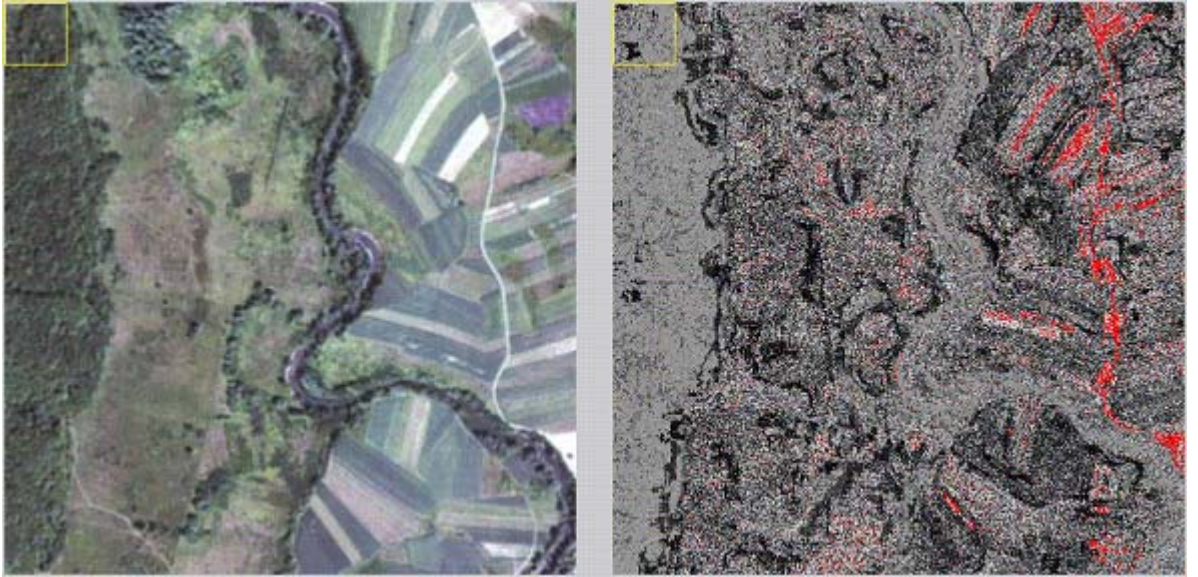
Figure 62: Site suspected to contain roads. Combination of models used in the interactive learning *PCA of hyperspectral images, PCA of texture parameters, SAR L Band polarimetric image*
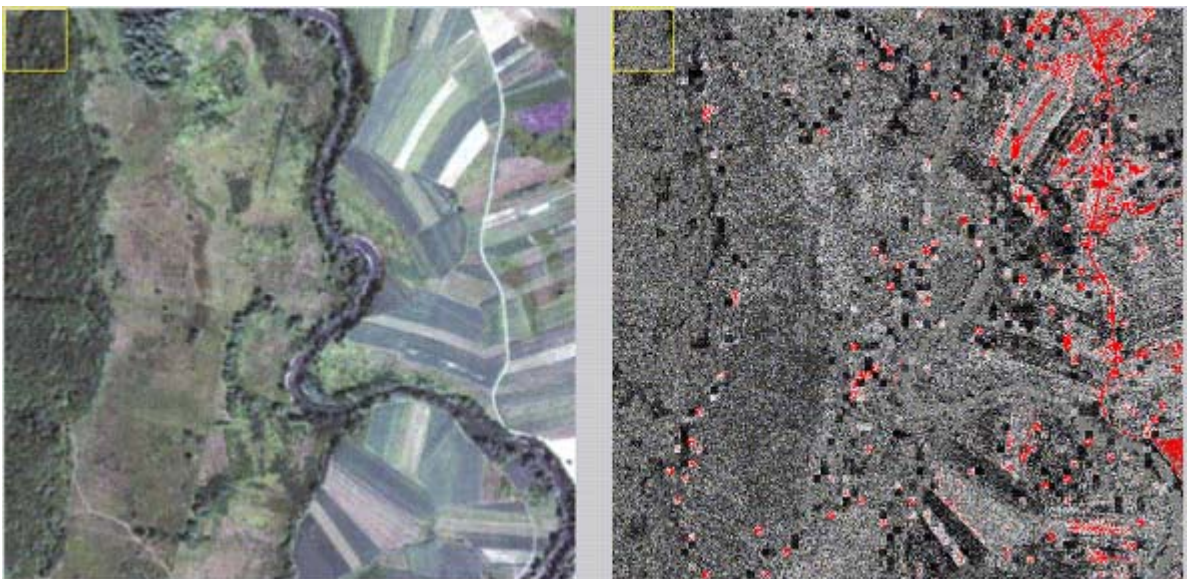
Figure 63: Site suspected to contain roads. Combination of models used in the interactive learning *PCA of hyperspectral images, PCA of texture parameters, SAR X Band polarimetric image*
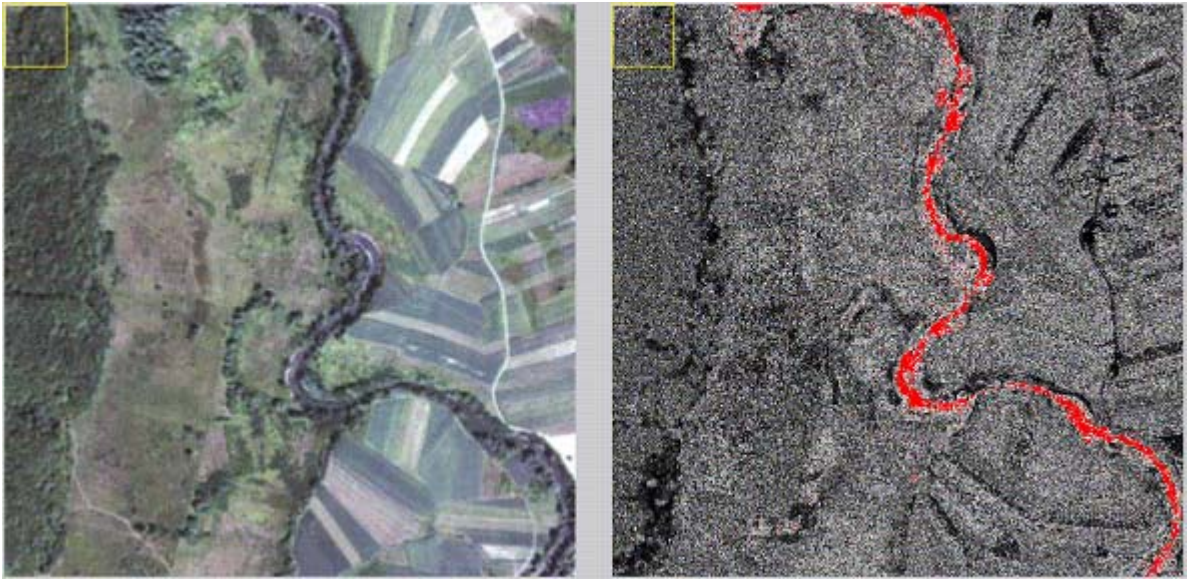
Figure 64: Site suspected to contain rivers. Combination of models used in the interactive learning *PCA of hyperspectral images, PCA of texture parameters, SAR L Band polarimetric image*
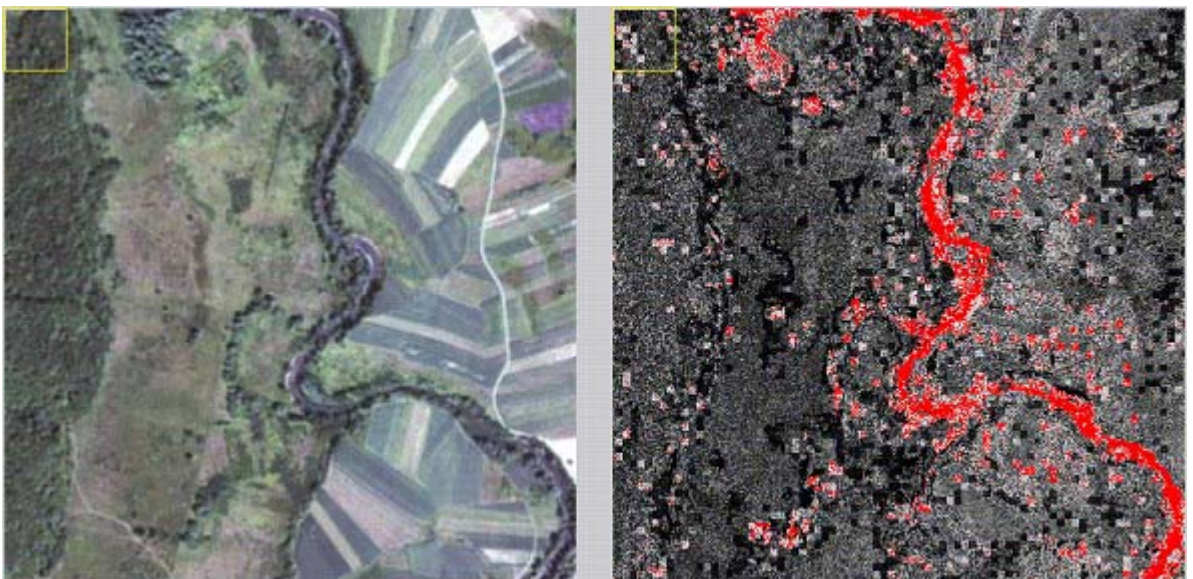
Figure 65: Site suspected to contain rivers. Combination of models used in the interactive learning *PCA of hyperspectral images, PCA of texture parameters, SAR X Band polarimetric image*

5.11.4.4 Quantitative analysis

In order to evaluate the results for combining different features in the system two experiments have been carried out.

First evaluation

A quantitative mechanism in order to get the good of the system detecting mining fields is needed. Firstly a mask of target must be created to compare with the results of the learning. The mask consists of a layer which pixels values are between 0 and 6, each of them corresponding to a class (forest, agriculture fields used, agriculture fields not used, bare soil) or to an object (river, road). In figure 66, you can observe the created target mask.
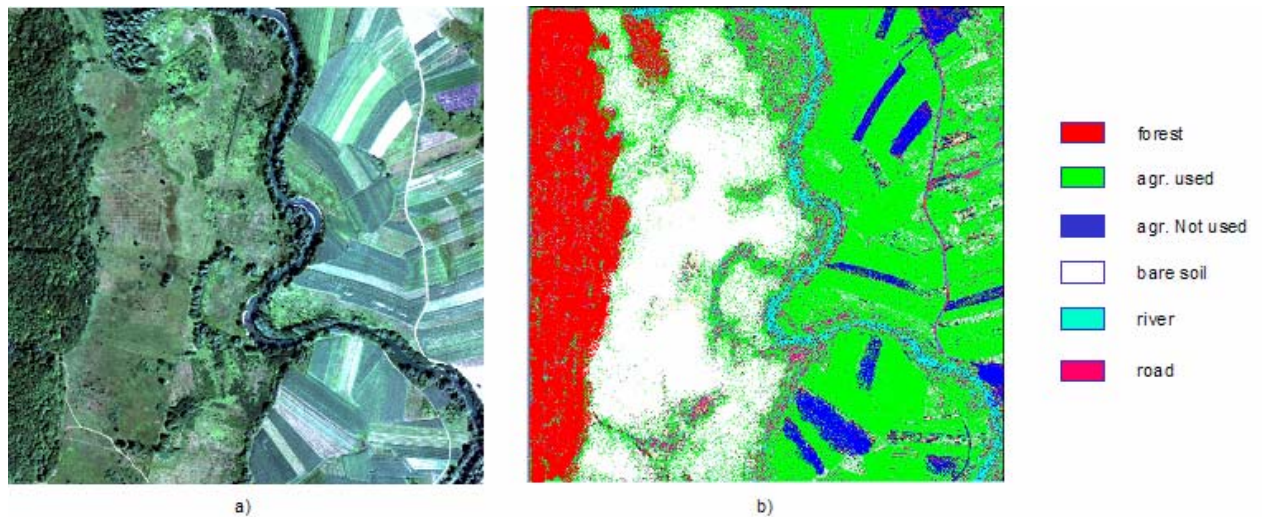
Figure 66: a) Daedalus data site of Glinska Poljana, b) mask used for the evaluation.

In order to evaluate the methods after the interactive learning, we need to extract the information contained in the classification map. To do it, some labels are defined and analyzed. This analysis consists of comparing the learning results with the mask and quantifying the percentage of the detected area corresponding to each class or object. Those areas which are classified as targets and do not correspond to any class or object will be treated as false alarm. On the Daedalus data site of Glinska Poljana shown in figure 66, 12% of the image corresponds to forest, 67% to agriculture fields used, 3% to agriculture fields not used, 11% to bare soil terrain, 0,98% to the road and 4% to the river. The rest of the image that does not correspond to any of this classes or objects is not classified.

For the evaluation several experiments have been carried out (see fig. 67). In the first one, only spectral features have been chosen and for the other two also texture and polarimetric features have been selected. Two percentages will be found per combination of models and class or object. The first number corresponds to the detected percentage of the class or object and the second one to the detected false alarms. For instance, looking at the column of forest and choosing hyperspectral as models, it is concluded that after the learning process 90% of the forest is detected and 23% comes as false alarms.

After the evaluation process, several conclusions are extracted.

- Using only hyperspectral features, the detection of the objects is very high, meanwhile it is not so good to detect the classes.
- Using not only hyperspectral features, but also polarimetric ones the detection of classes (agricultural fields used and not use and bare soil) increase. On the other side, the

detection of specific objects, as road or river is not as good as using only hyperspectral models.

- The principal component analysis (PCA) of texture contributes important information, specially detecting classes.
- Comparing X- with L-Band, the former is better to detect objects but in order to detect classes L-Band looks much better.

	Models	Classes (targets – false alarms)				Objects (targets – false alarms)	
		Forest	Agriculture fields used	Agriculture fields not used	Bare soil	Road	River
	Total cover area on the image	12%	67%	3%	11%	0,98%	4%
2 Models	Hyperspectral	90%-23%	44%-17%	39%-28%	73%-36%	0%-21%	86%-16%
4 Models	Hyperspectral (PCA) Texture (PCA) X-Band (embd) X-Band (gmrf)	85%-67%	54%-33%	46%-66%	80%-61%	0%-19%	53%-32%
	Hyperspectral (PCA) Texture (PCA) L-Band (embd – vh) L-Band (embd – vv)	50%-67%	84%-44%	39%-48%	86%-55%	0%31%	53%-38%

Figure 67: Percentages of detected classes/objects and false alarms after the interactive learning selecting different combination of models in each iteration.

Second evaluation

A second test is done, but in this case in order to discriminate the vegetation in E-SAR images. Figure 68 shows the results of several experiments selecting in each case a different combination of features.

test	band/polar	models	Probability of Detection	Probability of False Alarms	conclusion: synergy between two bands
1	L-band	model 1 : qmrf L-band HH	correct : principal vegetative cover extracted	confusion in zones of manufacture - correct in the vegetative areas	
	L-band	model 2 : qmrf L-band HH	problem in isolated bushes	confusion in isolated bushes	
2	L-band	model 1 : qmrf L-band HH	correct : principal vegetative cover extracted	confusion in zones of manufacture - correct in the vegetative areas	same proportion
	L-band	model 2 : qmrf L-band HV	problem in isolated bushes	if negative example in zones of manufacture degradation	
3	L-band	model 2 : qmrf L-band HH	correct : principal vegetative cover extracted	confusion in zones of manufacture - correct in the vegetative areas	same proportion
	L-band	model 2 : qmrf L-band VV	problem in isolated bushes	confusion in isolated bushes	
	L-band	model 2 : qmrf L-band HV	correct : principal vegetative cover extracted	confusion in zones of manufacture - correct in the vegetative areas	
	L-band	model 2 : qmrf L-band vH	problem in isolated bushes	confusion in isolated bushes	
4	L-band	model 1 : qmrf L-band HH scale 1	correct, small improvement in relation to 1	less false alarms than in 1, 2, 3	same proportion
	L-band	model 2 : qmrf L-band HH scale 2	the isolated trees are better detected		
5	X-band	model 1 : qmrf X-band HH scale 1		prob. of false alarms bigger that in test 1	same proportion
	X-band	model 2 : qmrf X-band HH scale 1			
6	X-band	model 1 : qmrf X-band HH scale 1		prob. of false alarms bigger than in test 1	same proportion
	X-band	model 2 : qmrf X-band HH scale 2			
7	L-Band	model 1 : embd X-band HH scale 1		big prob. of false alarms	
	L-Band	model 2 : embd X-band HH scale 1			
8	L (band polar)	model1: alpha	good	prob. of false alarms mediocre	
		model1: alpha			
9	L band	entropy		mediocre	
10	L band	anisotropy		mediocre	
	L band	anisotropy			
11	L band	spectr ampl	good: the most vegetative cover is detected:	false alarms on the fields	spectr ampl> spectr anisotr
12	L band	spectr anistropy	small bushes and hedges	but the prob. of false alarms in zones of manufacture is smaller than in 1, 2, 3, …	
	P band	spectr ampl	problem with isolated trees	prob. of false alarms bigger than in L-band: prob. of false alarms on the fields	
	P band	spectr ampl			
13	P band	despeckled, hor-vert-cross polar - intensity	very good detection also in small bushes	prob. of false alarms suitable	
	P band	despeckled, mean of co and cross - intensity			
14	X band	despeckled, ert-vert-co polar - intensity	results not good: the whole image is detected	results not good	
		despeckled, ert-vert-co polar - intensity			

Figure 68: Discrimination of vegetation in E-SAR images.

Looking at the evaluation results, several conclusions are deduced:

- L-Band gets better results than X- and P-band (X-band produced a diffusion on the surface).
- Better results can be obtained giving polarimetric filters.

- Texture gmrf contributes important information, there are some confusion problems over zones of manufacture in some images. The polar band gives almost no information for these texture parameters.
- The parameters anisotropy, entropy, and alpha angle do not contribute to get a good classification. Giving only three clicks, the whole image is detected.
- The color of the test´s number means how good the results are. From better results to worse the classification is: red, blue, green and black.

5.11.5 **Conclusions**

The new developed concept for image information mining helps the understanding and exploration of large volumes of data. It opens a huge potential to extract essential information from remote sensing images.

In order to express a degree of believe that a field is mined or not, the expert in the de-mining action is using the concepts of forest, bare soil, agriculture fields used and not used. On the other hand, the expert in the military domain knowledge (mining) is focusing on objects as road, river or bridge. Considering this, the classification of a mined field is reduced to the exclusion of forest, bare soil, river, road, agricultural fields used and not used and bridge. This knowledge is stored in a database.

The user has a content-based retrieval information possibility and can interactively evaluate the sensors and access to the information of the images stored in the knowledge-based database.

The extracted knowledge from the system is used to evaluate the sensors in detection of mined fields. The following conclusions can be extracted:

- In order to detect objects, using hyperspectral features better results are obtained.
- In order to detect classes, giving polarimetric filters help clearly.
- Texture parameters and the principal component analysis (PCA) of them contribute important information.
- In terms of polarimetric features, L-Bands gets better results than X-Band.

References

[1] Mihai Datcu and Klaus Seidel, "Human Centered Concepts for Exploration and Understanding of Satellite Images", Proc. of the IEEE Workshop on Advances inTechniques for Analysis of Remotely Sensed Data, CD-ROM, 8 pag. 2003.

[2] M. Datcu, H. Daschiel, et al., "Information mining in Remote Sensing Image Archives: System Description", IEEE Trans. on Geoscience and Remote Sensing, ISSN 01 96 2892, Vol. 41, No. 12, pag. 2923-2936, 2003.

[3] KIM Project (ESA, DLR, ETH Zurich, ACS Rome),
"http://earth.esa.int/rtd/Projects/#_CompletedProjects"

[4] M.Schröder, H. Rehrauer, K. Seidel, M. Datcu, "Interactive Learning and Probabilistic Retrieval in Remote Sensing Image Archives", IEEE Transactions on Geoscience and Remote Sensing, Vol. 38, pp. 2288-2298, 2000.

[5] M. Datcu, K. Seidel, S. D´Elia, P. G. Marchetti, "Knowledge-driven Information-Mining in Remote Sensing Image Archives", ESA Bulletin 110, pp. 26-35, 2002.

[6] Lorenzo Bruzzone, and Diego Fernandez Prieto, "Unsupervised Retraining of a Maximum Likelihood Classifier for the Analysis of Multitemporal Remote Sensing Images", IEEE Transactions on Geoscience and Remote Sensing, Vol. 39, No. 2, pp. 456-460, February 2001.

6   Integration of Tools into SMART environment

6.1   Data Header Modifications

At the beginning all SMART data at DLR was using a header in form of 10 long integer and 10 float numbers containing information about important image parameters (dimensions in x and y, pixel size, number of channels, ...). In autumn 2003 a decision about the image format was taken in the SMART project to use a separate ASCII header file instead of saving header information in the same file as the data. Therefore the data sets had to be modified to fulfil the SMART requirements. All data headers had to be removed, separate ASCII header files had to be prepared. Now the developed tools had to be modified too, they were provided to the partners step by step for testing.

6.2   Integration of Algorithms

For the implementation of the developed algorithms into the SMART environment it is necessary that the algorithms have a defined form. Since different programming languages are used by the partners in SMART and the rewriting of the algorithms in C/C++ would have been very time consuming, it has been agreed by TRASYS and DLR that TRASYS purchases an IDL runtime license and DLR provides the algorithms in IDL. For input and output operations it was defined to use a special ASCII text file format. The algorithms were updated to fulfil these criteria and sent to TRASYS for testing and integration.

6.3   Input / Output ASCII Files

The SMART environment contains a runtime version of IDL 6.0 which allows it to run executables of routines written in IDL 6.0 or prior versions. The user interface is created by TRASYS so that the user of the SMART environment is not confronted with different versions of input and output windows. The end-user does not notice that different programs work together in the SMART environment.

All input and output of the IDL routines is passed by ASCII-files named xxx_input.txt and xxx_output.txt with xxx the name of the routine.

Example of an input file (calc_insar_smart_ input.txt):

```
Infile1      e:\mkeller\daten\glinska\esar\0108_t11_Lmaster_12\0108_t11_slc_sr_pol.dat
Infile2      e:\mkeller\daten\glinska\esar\0110_t03_Lslave_13\0110_t03_slc_sr_coreg_pol.dat
Savepath     e:\mkeller\daten\glinska\esar\0108_t11_Lmaster_12\if\
Sr2geopath e:\mkeller\daten\glinska\esar\0108_t11_Lmaster_12\orig\geo\data\
```

The first column shows the parameter names and must not be changed. The second column contains the needed information about the input data and can modified, e.g. when the data is moved to another place on the hard disk.

Example of an output file (calc_insar_smart_output.txt):

CALC_INSAR_SMART: Calculations of the interferometric coherence and
the interferometric phase from an IF data set.

Input files:

  SAR SLC 3-channel polarimetric IF master data:
   e:\mkeller\daten\glinska\esar\0108_t11_Lmaster_12\0108_t11_slc_sr_pol.dat

  SAR SLC 3-channel polarimetric IF slave data:

e:\mkeller\daten\glinska\esar\0110_t03_Lslave_13\0110_t03_slc_sr_coreg_pol.dat

  Transformation matrix with geocoding information (azimuth positions)

e:\mkeller\daten\glinska\esar\0108_t11_Lmaster_12\orig\geo\data\0108_t11_positionsaz_slc_geo.dat

  Transformation matrix with geocoding information (range positions)

e:\mkeller\daten\glinska\esar\0108_t11_Lmaster_12\orig\geo\data\0108_t11_positionssr_slc_geo.dat

  Path to save the processing results
   e:\mkeller\daten\glinska\esar\0108_t11_Lmaster_12\if\

Output files:
  Data of the hhhh-, xxxx-, vvvv-polarised IF coherences
  Data of the hhhh-, xxxx-, vvvv-polarised IF phases
  Tif-images of all data sets
  Header files to all data sets

The input data mast be 3-channel complex little endian pixel
interleaved SLC data sets of the hh-, xx-, and vv-polarisations.
The dimensions must be: (3, pixels in range, pixels in azimuth)

Starting calculations at   Fri May 28 10:47:14 2004

Calculating flat earth phase...

Window size for IF coherence calculation:
    7 pixels in range direction
    24 pixels in azimuth direction

Starting calculations for hhhh-polarisation

Calculation of the hhhh IF coherence...
Slant range to geocoded conversion...
Saving coherence results in slant range format to
 0108_t11_0110_t03_coh_hhhh.dat
Saving coherence results in geocoded format to
 0108_t11_0110_t03_coh_hhhh_sr2geo.dat

Calculation of the hhhh IF phase...
Slant range to geocoded conversion...
Saving IF phase results in slant range format to
 0108_t11_0110_t03_ifphase_hhhh.dat

Saving IFphase results in geocoded format to
0108_t11_0110_t03_ifphase_hhhh_sr2geo.dat

Starting calculations for xxxx-polarisation

Calculation of the xxxx IF coherence...
Slant range to geocoded conversion...
Saving coherence results in slant range format to
0108_t11_0110_t03_coh_xxxx.dat
Saving coherence results in geocoded format to
0108_t11_0110_t03_coh_xxxx_sr2geo.dat

Calculation of the xxxx IF phase...
Slant range to geocoded conversion...
Saving IF phase results in slant range format to
0108_t11_0110_t03_ifphase_xxxx.dat
Saving IFphase results in geocoded format to
0108_t11_0110_t03_ifphase_xxxx_sr2geo.dat

Starting calculations for vvvv-polarisation

Calculation of the vvvv IF coherence...
Slant range to geocoded conversion...
Saving coherence results in slant range format to
0108_t11_0110_t03_coh_vvvv.dat
Saving coherence results in geocoded format to
0108_t11_0110_t03_coh_vvvv_sr2geo.dat

Calculation of the vvvv IF phase...
Slant range to geocoded conversion...
Saving IF phase results in slant range format to
0108_t11_0110_t03_ifphase_vvvv.dat
Saving IFphase results in geocoded format to
0108_t11_0110_t03_ifphase_vvvv_sr2geo.dat

Ending calculations at   Fri May 28 11:01:10 2004
Program CALC_INSAR_SMART finished!

6.4 ASCII Header Files

All spatial data (Daedalus, geocoded E-SAR data, SLC E-SAR data, DEMs, geocoding matrices,...) will get a header file called yyy.hdr if the data set is called yyy.dat . The header file is an ASCII-data set containing two columns (parameter name and value). Each line describes another parameter. At the beginning of the header file are the parameters needed for ArcGIS, followed by additional parameters describing the data set. Other parameters or remarks can be added at the end of the file. An example for an ASCII header file is:

```
NCOLS                3600
NROWS                4800
NBANDS               12
NBITS                8
NODATA               0
ULXMAP               588325.062500
ULYMAP               5031795.000000
XDIM                 1.0
YDIM                 1.0
OFFSETX              0
OFFSETY              0
SENSORTYPE           MULTISPECTRAL_SCANNER
SENSORNAME           DAEDALUS
CONTENT              DATA
GEOMETRY             GEOCODED
AREA                 GLINSKA_POLJANA
DATATYPE             BYTE
LEGENDFILE           NOT_APPLICABLE
SR2GEOFILE_AZ        NOT_APPLICABLE
SR2GEOFILE_SR        NOT_APPLICABLE
SARPOLARISATION      NOT_APPLICABLE
SARLOOKDIRECTION     NOT_APPLICABLE
SARBAND              NOT_APPLICABLE
DESCR_CH1            BLUE
DESCR_CH2            BLUEGREEN
...                  ...
DESCR_CH12           THERMAL_INFRARED
```

7 Dissemination / Exploitation Information

7.1 Conferences, Workshops...

Date	Type and title / scope	Number of persons + other information
01-05/04/2002	SPIE Aerosense conference	2 persons, talk in session OR41, Nr. 4742-98
14-16/01/2003	POLinSAR workshop, Frascati, Italy	1 person, SAR polarimetry and interferometry
27-28/10/2003	Title: Human Centered Concepts for Exploration and Understanding of Satellite Images	1 person , IEEE Workshop on Advances in Techniques for Analysis of Remotely Sensed Data, Goddard

Table 9: Conferences / workshops

7.2 Articles Published,...

Martin Keller (DLR), Nada Milisavljevic (RMA), Helmut Süß (DLR), Marc Acheroy (RMA): Reduction of Mine Suspected Areas by Multisensor Airborne Measurements - First Results, SPIE Aerosense conference 2002, Orlando, USA, Paper-Nr: 4742-98

M. Datcu, K. Seidel, 2003, Human centered concepts for exploration and understanding of satellite images, Proc. of the IEEE Workshop on Advances in Techniques for Analysis of remotely Sensed Data, NASA GSFC, MD, USA.

8 Main Results

- The Zeppelin-NT airship can be used for very high resolution measurements from low altitudes. It has stronger deviations in altitude and flight attitude than an aircraft but the resulting errors in the data can be removed. For high resolution data with a small pixel size a very high effort is necessary to reduce geocoding errors. While recording high resolution data, the area which can be recorded per hour drops considerably which leads to significantly higher costs for the measurement campaign.
- IDL algorithms can be run in the SMART system in a way the user doesn't notice that he uses different software packages.
- E-SAR data and important E-SAR processing results are available in the same format as the Daedalus data and can be used as additional channels for fused classification and analysis.
- Using both SAR and multispectral scanner data increases considerably the ability to separate different kinds of objects. For future projects maybe not all the SAR information can be collected and exploited which we have in SMART. In this case the priority rank is:

  1. Polarimetric geocoded and SLC L-band data
  2. Single geocoded channels in X- and P-band (multifrequency SAR data)
  3. Interferometric L-band data
  4. Polarimetric and/or interferometric SLC data and geocoded data in X- and P-band.

9 Appendix: Images of Collected E- SAR Data

DLR — HR E—SAR SYSTEM MOTION COMPENSATION PROCESSOR

GLINSKA Date: 07—AUG—2001 Time: 11:43:46 Coordinates: N 45°21'15" E 16°10'50"

Image Parameters > * Resolution: 4.0 m × 4.0 m (Range × Azimuth) * Pixel Size: 0.7 m × 0.7 m
* Image Size: 3396 m × 5734 m * Near Range: 3372 m * Altitude: 3055 m * Ground Speed: 88 m/s
* WCA: 2° * Processed Squint: 0° * Antenna Depression Angle: 35° * PRF: 500 Hz * V 3.0/IMU / GPS
* RF Center Frequency: 0.45 GHz * Polarisation HH * Number of Looks: 4 * ID: 01SMARTY0117X1_CH1

GROUND RANGE

FLIGHT DIRECTION → 0°